

Sustaining glacial-fed catchments with artificial ice reservoirs

Suryanarayanan Balasubramanian

August 29, 2022
Version: My First Draft



Sustaining glacial-fed catchments with artificial ice reservoirs

Suryanarayanan Balasubramanian

- 1. Reviewer* **Felix Keller**
ETH Zurich and Academia Engiadina
- 2. Reviewer* **Marcus Nüsser**
South Asia Institute
- 3. Reviewer* **Michael Lehning**
Swiss Federal Institute of Technology Lausanne and WSL
Institute for Snow and Avalanche Research
- 4. Reviewer* **Thomas Vikhamar Schuler**
University of Oslo
- Supervisor* Martin Hoelzle

August 29, 2022

Suryanarayanan Balasubramanian

Sustaining glacial-fed catchments with artificial ice reservoirs

Artificial Ice Reservoirs, August 29, 2022

Reviewers: Felix Keller, Marcus Nüsser, Michael Lehning and Thomas Vikhamar Schuler

Supervisor: Martin Hoelzle

English editors: Lou Del Bello and Ana Rodríguez Crespo

University Of Fribourg

Cryosphere Research Group

Department of Geosciences

Av. de l'Europe 20

CH-1700 and Fribourg

Preface

Please put your preface here.

Fribourg, August 29, 2022

Martin Hoelzle

Abstract

Irrigated agriculture is crucial for the livelihood security of mountain communities. Using meltwater from glaciers, snow and permafrost, mountain dwellers have developed sophisticated techniques to cope with recurrent water scarcity caused by glacial retreat, glacier thinning, and seasonal snow-cover dynamics. Artificial ice reservoirs (AIRs) are a key example of community based water management. Worldwide, farmers in 26 mountain villages build these ice structures. These seasonal ice reservoirs increase meltwater availability during the critical period of water scarcity in spring. To assess the role of AIRs within the water resource management of mountain villages under a changing climate, they need to be represented in integrated modelling frameworks. To achieve efficient water storage, their design needs to take into account the location's weather conditions and water availability throughout the year. This thesis aims to examine the volume evolution of AIRs within the framework of a mass and energy balance model, as well as developing construction strategies that can enhance their size and duration while increasing their water-use efficiency.

To start, we estimate the differing contribution of AIR surface processes built in Guttannen, Switzerland and Ladakh, India. These two locations exhibit different meteorological patterns due to their significant latitude, longitude and altitude differences. Using an AIR-specific mass and energy balance model which keeps into account meteorological factors, fountain discharge and ice volume changes, surface processes are quantified and compared across the two locations. The results reveal that higher sublimation process enhanced the Indian AIRs freezing rate, and poor fountain operation of both the AIRs resulted in wastage of four-fifth of the water supply provided. These results therefore highlight the relevance of colder, drier climates and fountain water supply management in optimizing AIR construction.

Then, we focus on the Swiss Alps to provide the first estimate of the water loss reduction achieved due to fountain scheduling strategies. Fountain scheduling was realized through a control valve that was automated with optimal discharge rates computed using real-time weather input and location metadata. Simulations converting unscheduled fountains to scheduled fountains showed a more than threefold improvement in the water use efficiency of several AIRs. Fountain operation using scheduling strategies produced similar ice volumes while consuming one-tenth

of the water compared to their unscheduled counterparts. Overall, these results show that automated fountain water supply management can both increase the water use efficiency of AIRs and reduce their maintenance needs without compromising on their meltwater production.

This thesis advances the current understanding on the volume evolution of AIRs under different climates. It provides tools to quantify the storage potential of these ice structures worldwide and practical strategies to improve their efficacy. This study provides the scientific evidence needed to upscale this indigenous water storage technology, thus challenging the preconception that local water management traditions are outdated and supporting the uptake of nature-based solutions for water security. Future work may build on this research by fully integrating climate change scenarios to investigate the potential hydrological contributions of ice harvesting technologies for water-stressed mountain catchments.

Contents

Preface	v
Abstract	vii
1 Ice Reservoirs	1
1.1 Introduction	1
1.2 Nomenclature and Classification	4
1.3 Objectives	5
1.4 Structure	5
2 Religion of ice reservoirs	7
2.1 An old history	7
2.2 The marriage of glaciers	8
2.3 From folklore to science	9
3 Science of ice reservoirs	11
3.1 Study sites and data	12
3.2 AIR Model	15
3.3 Model calibration, uncertainty and validation	27
3.4 Model limitations and suggestions for improvement	31
4 Technology of ice reservoirs	37
4.1 Types of ice reservoirs	37
4.2 The need for water supply management	42
5 Habitat of ice reservoirs	49
5.1 Observed ice volume variability	49
5.2 Metrics to judge site suitability	51
6 Heritage of ice reservoirs	55
6.1 Summary	55
6.2 Conclusions	56
6.3 Discussion	58

6.4 Future research direction	59
7 Peer-reviewed papers	61
7.1 Paper I	61
7.2 Paper II	79
7.3 Paper III	105
Bibliography	113
A Appendix	131
A.1 Drone surveys processing methodology	131
A.2 Sensitivity and uncertainty analysis	133
A.3 Model forcing based on water-use efficiency and maximum ice volume objectives	136
Acknowledgement	139
Declaration	145

Ice Reservoirs

“*Glaciers are the secret of life in these otherwise lifeless deserts. But now, they are melting away at an alarming rate.*

— Sonam Wangchuk

(Ramon Magsaysay awardee, Inventor of ice stupas)

1.1 Introduction

Irrigation networks in arid mountain regions are completely dependent on the timely availability of meltwater from glaciers, snow and permafrost (Immerzeel et al., 2020; Farhan et al., 2015; Tveiten, 2007). With the accelerated decline of glaciers due to climate change (Marcus Nüsser and Baghel, 2016), these regions are experiencing acute water scarcity (Norphel and Tashi, 2015; Mukhopadhyay and A. Khan, 2015). Further, the unreliability and the foreseen decrease of seasonal snow cover (Chevuturi et al., 2018) affects the cryosphere’s ability to store water, especially in spring.

For example, due to the short growing period, central Ladakh is a single-cropping area with barley and wheat as important staples, complemented by vegetables, pulses, and oil seeds (M. Nüsser et al., 2019). Depending on the altitude, irrigation with complete flooding of fields (approximately 2-5 cm water column) starts between March and April prior to the melting of high-altitude glaciers (Fig. 1.1). This results in increased demand during a period of reduced supply at the onset of the agricultural season (Fig. 1.1).

To cope with this recurrent water scarcity, villagers have developed two types of Artificial Ice Reservoirs (AIRs): ice stupas and ice terraces (Fig. 1.2). Both the ice reservoirs capture water in the autumn and winter, allowing it to freeze, and hold it until spring, when it melts and flows down to the fields (IPCC, 2019; Vince, 2009; Clouse et al., 2017; M. Nüsser et al., 2019). In this way, they retain a previously

unused portion of the annual flow and facilitate its use to supplement the decreased flow during the following spring (Fig. 1.1).

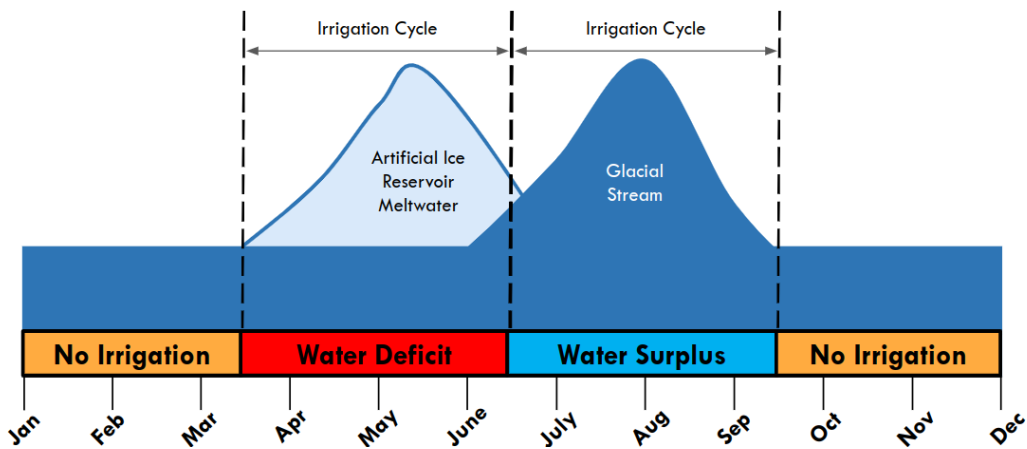


Fig. 1.1.: Seasonal variation in the availability of irrigation water. The graph highlights the crucial role of AIRs in bridging the gap in water availability. Adapted from Marcus Nüsser and Baghel, 2016

There is a long tradition of developing such ice harvesting structures in the upper Indus Basin, in both Ladakh, northern India (Labbal, 2000; Marcus Nüsser, S. Schmidt, et al., 2012) and various locations in northern Pakistan (Kreutzmann, 2011). According to oral history and Corona imagery from 1969, the first ice terraces are older than 50 years. Over the past decade, several ice stupas have been built to supplement the irrigation water supply of mountain villages in India (Sonam Wangchuk, 2020; Palmer, 2022; Aggarwal et al., 2021), Pakistan (Awaz Production, 2022), Kyrgyzstan (BBC News, 2020), Nepal, and Chile (Reuters, 2021).

Despite this widespread adoption, only a few publications examine the role of AIRs in the water resource management of these regions. Notably, none of these prior reports have investigated AIRs outside Ladakh. Moreover, the available estimates of water storage capacity of AIRs in Ladakh vary widely (Norphel and Tashi, 2015; Bagla, 1998).

Quantifying the water storage capacity of AIRs is not straightforward since the processes by which AIRs are formed are complex. These processes are controlled by local topography, meteorology and the construction strategies used. Modelling approaches to quantifying these processes exist on glacier surfaces but they are not readily applicable for AIRs due to their limited size, and comparatively more variable surface area. Therefore, conventional glacial modelling approaches need to be adapted in order to capture the spatio-temporal scale of AIR surface processes. Furthermore, these modelling approaches need to be validated and calibrated with comprehensive data from field measurements.

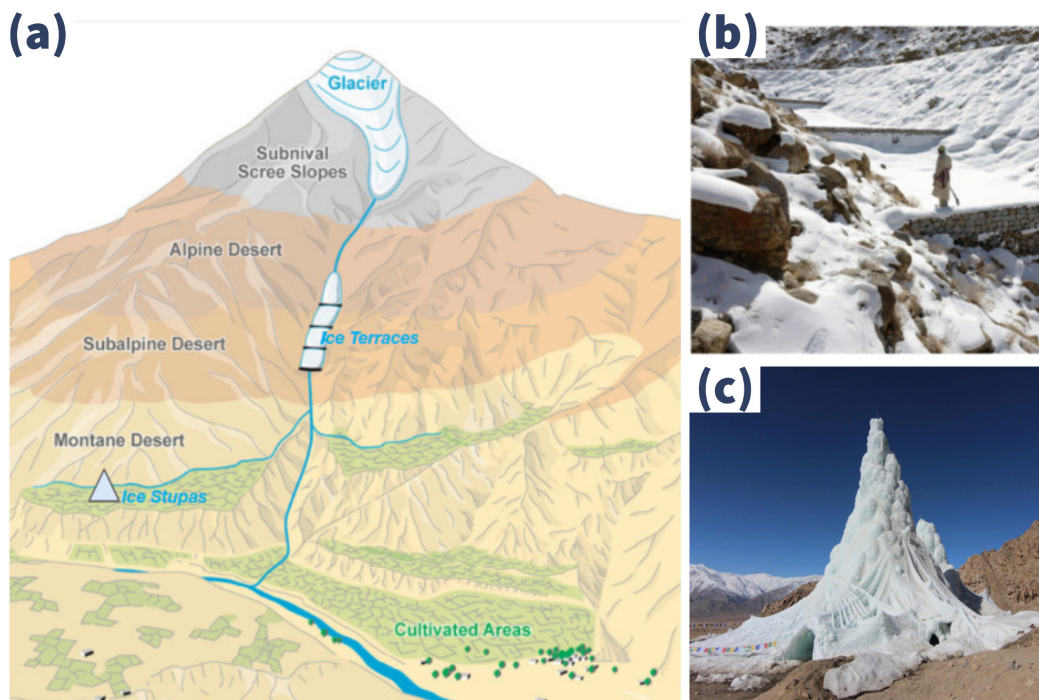


Fig. 1.2.: (a) Schematic overview of the position of artificial ice reservoirs. These constructions are located at altitudes between the glaciers and the irrigation networks in the cultivated areas. (b) Ice terraces at 3900 m, located above the village of Nang, Ladakh. The cascade is composed of a series of loose masonry walls ranging in height from 2 to 3 m, which help freeze water for storage. (c) Ice stupas at 3600 m, located above the village of Phyng, Ladakh. They are made using fountain systems. Adapted from Marcus Nüsser and Baghel, 2016

A spirit of improvisation guides the construction of AIRs (Clouse et al., 2017). Depending on the local topography and on how water is supplied, AIRs can form as flat sheets or vertical cones. This has resulted in ice reservoirs exhibiting significant volume variations despite experiencing similar meteorological conditions. For example, in Ladakh, India, ice terraces have attained volumes up to 30 times larger than ice stupas (M. Nüsser et al., 2019). However, the processes driving these differences can only be understood if the complete design methodology behind each construction is available.

This thesis aims to fulfill both these requirements by providing a new set of AIR-specific volume and area measurements via drone flights, along with meteorological data during the construction period. All these datasets were generated through construction strategies that used fountain systems. These systems are quantified via in-situ observations of the fountain characteristics and discharge rate measurements. First, this thesis formulates a one-dimensional AIR model in order to calibrate and validate it with the procured AIR datasets. Then it uses this model as a tool to

propose a construction strategy that can produce AIRs efficiently and effortlessly. It is important to note that while this thesis reviews published AIR research and presents a comprehensive quantitative study of their water storage potential, we acknowledge that the farming communities that have been building these structures since mid-1800s are the custodians of substantial additional knowledge.

1.2 Nomenclature and Classification

While the term "artificial glacier" is more commonly used, we deliberately use the term "ice reservoir" in this thesis. By definition, all glaciers, including the smallest ones, are bodies of sedimentary ice which were built by progressive snow compaction and firnification and flow downhill under the influence of gravity (Benn, Douglas I and Evans, David JA, 2014). Hence, because of their genesis and composition, AIRs differ from glaciers. Man-made ice structures typically have a lifetime in the order of months and a size million times smaller than typical glaciers. Therefore, any comparison between these ice structures can be misleading. Since glaciers are considered natural ice reservoirs, we use the terminology AIRs to distinguish the man-made ice structures described in this thesis from the natural ones.

However, when classified in terms of size and survival duration, AIRs exhibit similar characteristics to very small glaciers. The glossary of glacier mass balance and related terms by Cogley et al. (2010) defines very small glaciers or glacierets as follows:

A very small glacier, typically less than 0.25 km^2 in extent, with no marked flow pattern visible at the surface. To qualify as a glacieret, an ice body must persist for at least two consecutive years. Glacierets can be of any shape, and usually occupy sheltered parts of the landscape. Windborne snow and avalanches can be dominant contributors to the accumulation of glacierets.

This rather broad definition of glacierets or very small glaciers may be best suited to describe AIRs, since they have been measured with areas as high as 0.15 km^2 and observed to last beyond a year.

As noted above, AIRs's construction strategies are usually inspired by a spirit of improvisation which challenges their classification. However, it has been found that construction strategies that use fountain systems form conical AIRs, while those that don't form flat sheets of ice. Therefore, this thesis classifies all the AIRs produced based on whether or not they use fountain systems. AIRs using fountain systems

are called "ice stupas" and those without are called "ice terraces" as this terminology denotes the resulting shape of the respective AIRs appropriately.

1.3 Objectives

This study employs an integrated approach, which includes field measurements and modelling, to answer the following research questions:

1. What is the influence of construction location and fountain characteristics on ice stupa volume evolution?
2. How can ice stupa fountain systems be engineered to reduce their water losses and maintenance efforts?

An energy and mass balance model for AIRs was designed to answer the first research question (paper I and III). Since in-situ measurements were required to run this model, we executed a measurement campaign in Switzerland and India during the past 4 winters. These datasets provided the necessary input, calibration and validation data to model the evolution of AIRs and study their sensitivity to meteorological conditions and fountain characteristics.

We also developed new construction strategies to answer the second research question. These strategies employed fountains the discharge rate of which was regulated by an automation system that used the AIR model previously developed. Their advantages over traditional construction strategies are quantified in paper II.

1.4 Structure

Chapter 1 introduces the motivation of this work and provides a summary of the state of knowledge about AIRs prior to this thesis. Chapter 2 describes the origins of this technology as a religious practice. Chapter 3 gives an overview about the study sites and introduces the different field techniques applied. The engineering design of AIR technologies are showcased in Chapter 4 along with suggestions for their improvement. The observed spatio-temporal variations in AIR volume evolution are presented in Chapter 5 along with suggestions for choosing future construction locations. Chapter 6 concludes the thesis with a synthesis and the future scope of this work. Chapter 7 lays out the peer-reviewed work supporting the conclusions of this thesis.

Religion of ice reservoirs

“ We believe that glaciers are alive. That’s why a combination of female and male ice was necessary.

— Liaquat Ali Baltee
(Resident of Skardu)

For centuries, in the Himalayan mountain ranges, local cultures have believed that glaciers are alive. And what's more, that certain glaciers can have different genders. These local communities 'breed' new glaciers by grafting together—or marrying—fragments of ice from male and female glaciers, then covering them with charcoal, wheat husks, cloths, or willow branches so they can reproduce in privacy. These glacierets transform into fully active glaciers that grow year by year with additional snowfall, serving as lasting reserves of water that farmers can use to irrigate their crops. Over time, these practices have inspired other cultures, in which people are now creating their own AIRs and using them to solve urgent challenges around water supplies.

2.1 An old history

According to legend, when the people of Baltistan, in Pakistan, learnt of the Mongol army advancing towards them from the north in the early 13th century, they came up with an ingenious way to stop them. As the inhabited valleys were only accessible through narrow passes, they decided to block the entry way by building a glacier. This successfully prevented the Mongol invasion and, crucially, it also solved the locals' other big problem: water scarcity.

2.2 The marriage of glaciers

The people of Gilgit Baltistan believe that glaciers are living entities (Shabina Faraz, 2020; K. Khan, 2020). That's why a combination of female and male ice was absolutely necessary for them to multiply and grow. The male glacier – called ‘po gang’ locally – gives off little water and moves slowly, while a ‘female glacier’ – or ‘mo gang’ – is a growing glacier that gives off a lot of water.

The glaciers that people help grow are the fruit of the sacred union between a mother glacier and a father glacier. The ice formations get married and have offspring. For local communities, the selection of an appropriate site for this marriage is of utmost importance, and a suitable site must fulfil a list of conditions. It should be located at an altitude of at least 4000 or 5000 metres above sea level; it should be on a gentle slope, where it should have minimal exposure to sunlight, thus a north-facing mountain side is preferable. For most expert glacier grafters, the presence of permafrost or ice on the site is another key requirement.

Once a suitable spot is selected, the expedition can be planned. The bride and groom – the female and the male glacier, preferably from different villages – are chosen and the marriage can be organized. The glacier grafting usually takes place in November, when the local temperatures oscillate around zero. A 12-man party carries the pieces of female ice in woven baskets, another 12 men carry the male ice, the water drawn from the Indus river is carried traditionally in 12 gourd bottles, but sometimes clay pots or goatskins are also required, as well as charcoal and wheat husks or sawdust which act as insulators for the ice. The last ingredient is salt, which, according to some glacier grafters, helps protect the new glacier from impurities. The bride and groom party walk from different sites and meet at a certain point to climb together to their destination, where the new glacier will be created. No greetings are exchanged, as the people involved in the ceremony must remain silent until the ice is deposited in its new home. They walk continuously without any breaks, but if the distance is too much and rest is required, they do not put their loads on the ground: Instead, they hang the baskets on trees, or on walking sticks if nothing else is available. Each man has to carry around 15 to 25 kilograms of ice, walking in cold air, silently up the mountains, for a day or more. Once they reach the glacier growing site, they deposit their valuable loads. The ice lumps and water vessels are placed in between the boulders, or in a small cave, or sometimes in a pit dug specifically for this purpose, and are covered with layers of salt, charcoal and sawdust. The silence is finally broken as religious leaders recite verses of the Quran and pray for the success of the glacier marriage and for protection from the

djinns. Once the male and female glaciers are placed in their new home and covered, a man from the glacier grafters' party stands up and offers his life for the success of the process. His symbolic sacrifice is matched by the actual sacrifice of a goat – its meat is distributed to a charity, because prayers are more likely to be answered if accompanied by a charitable act. They will not visit the place for at least three years, so as not to disturb the glacier. It is said that a person who disturbs the glacier before its maturation will die. The celebrations continue in the village with traditional songs and prayers, alongside festive food and the joy of the accomplished mission.

2.3 From folklore to science

Myths, legends and superstitions are ways of codifying and disseminating knowledge. But in the face of a mounting climate crisis, they now need to be translated into the language of science. However, when it comes to glacier building expeditions, the evidence available is scant and anecdotal.

Classifying glaciers as male and female is, of course, a practice motivated by deep religious beliefs, but the method used to achieve this classification hints at an even deeper understanding of their temporal discharge patterns. In scientific terms, male glaciers are those who have achieved their peak water, likely leading to imminent water scarcity in their catchment. From this perspective, accelerated glacier shrinkage due to climate change is causing a gender imbalance. Such narratives are not designed to stand up to scientific scrutiny but rather to illustrate the state of the world in the most simple and effective way that can inspire societal change.

According to Tveiten (2007), the account of the glacier development process presented by a glacier grafter from Balghar, in the Baltistan region, bears a strong resemblance to the definition of the formation of rock glaciers as described in the conventional scientific literature:

“First the ice slips down into the rocks where it grows roots. Then it starts to break the rocks bringing them up. Then the glacier comes forward. This has happened where they did the glacier growing.”

Tveiten, who conducted field research in Baltistan, concludes that:

“glacier growing is typically performed [...] in a terrain that is conducive to the accumulation of snow by avalanching and snow slips. The presence of permafrost at these locations is likely to contribute to ice accumulating [...] Thus, glacier growing is conducted at locations which are already very prone to ice accumulation, and may explain why glacier growing is perceived to work.”

Here it is, traditional knowledge translated into the language of science.

Even the choice of the glacier grafting site suggests that the technique was developed as a result of the residents’ deep understanding of local environmental processes. The view of glaciers as animate entities implies that humans can influence their lives, just as glaciers can influence the lives of people.

Science of ice reservoirs

“ I could do with some scientific help from specialists. I am trying to collect data on how and where glaciers form best so that I can improve on them and people can use the technique elsewhere.

— Chewang Norphel
(Padmashree awardee, Inventor of ice terraces)

Prior AIR volume estimates differ widely from each other, are highly uncertain and restricted to the Ladakh region (M. Nüsser et al., 2019; Norphel and Tashi, 2015). Moreover, each structure is an accumulation of ice generated using specific weather conditions and differing construction strategies. This makes it challenging to extrapolate these findings across future winters or in new locations.

Modelling is a powerful tool that allows estimation of AIR volumes across space and time. However, in-situ measurements are required to tie these models to reality. The weather, water and volume measurements we carried out with an enormous input of manpower in the Indian Himalayas and the Swiss Alps provide a unique data basis for present and future AIR studies. The combination of measurements and modelling is key to understanding the influence of the construction strategy and location on AIRs.

In this chapter, we showcase the AIR datasets collected and develop a physically-based model that can estimate their volume evolution. Mass and energy balance equations were used to estimate the quantity of ice, meltwater, sublimation, and wastewater. Sensitivity and uncertainty analysis were performed to identify the most sensitive parameters and the variance they caused. For calibration, we chose two AIRs built across the winter of 2020/21 in India and Switzerland, and validated the model on a Swiss AIR built during 2019/20.

3.1 Study sites and data

We chose the Swiss Alps and the Indian Himalayan mountain regions to collect the required datasets described above. The study period starts when the fountain was first switched on (start date) and ends when the respective AIR either melted or broke into several ice blocks (expiry date). Each AIR dataset was abbreviated based on the construction strategy used, prefix of the country code and the suffix of the year of its expiry date. The construction strategies are distinguished based on whether they used fountain scheduling strategies to regulate water supply. Fountain scheduling was realized through a control valve that was automated with optimal discharge rates computed using real-time weather input and location metadata. Those that did were codenamed "automated" whereas the rest were codenamed "traditional". All except one construction campaign used traditional construction strategies. Therefore, traditional AIRs are referred to without explicitly specifying their construction strategy henceforth.

In total, 23 AIRs were studied in these two regions across four winters. However, only four AIRs located in Guttannen, Switzerland, and one in Gangles, India, had complete weather, water and volume measurements. Therefore, only these AIR datasets are used in the following analysis. The rest of the AIR datasets are described in the Appendix table A.1 and are used in later chapters to perform qualitative analysis.



Fig. 3.1.: The Swiss and Indian AIRs were 5 m and 13 m tall on January 9 and March 3, 2021 respectively. Picture credits: Daniel Bürki (left) and Thinles Norboo (right)

3.1.1 Swiss site

The Guttannen site (46.66°N , 8.29°E) is situated in the Berne region, Switzerland and has an altitude of 1047 m a.s.l. In the winter (Oct-Apr), mean daily minimum and maximum air temperatures vary between -13 and 15°C . Clear skies are rare, averaging around 7 days during winter. Daily winter precipitation can sometimes be as high as 100 mm . These values are based on 30 years of hourly historical weather data measurements (Meteoblue, 2021). Several AIRs were constructed by the Guttannen Bewegt Association, the University of Fribourg and the Lucerne University of Applied Sciences and Arts during the winters of 2020-22.

3.1.2 Indian site

The Gangles site (34.22°N , 77.61°E) is located around 20 km north of Leh city in the Ladakh region, lying at 4025 m a.s.l. . The mean annual temperature is 5.6°C , and the thermal range is characterized by high seasonal variation. During January, the coldest month, the mean temperature drops to -7.2°C . During August, the warmest month, the mean temperature rises to 17.5°C (Marcus Nüsser, S. Schmidt, et al., 2012). Because of the rain shadow effect of the Himalayan range, whereby a peak obstructs the path of the clouds, the mean annual precipitation in Leh totals less than 100 mm , and there is high interannual variability. While the average summer rainfall between July and September reaches 37.5 mm , the average winter precipitation between January and March amounts to 27.3 mm and falls almost entirely as snow.

3.1.3 Meteorological data

Air temperature, relative humidity, wind speed, pressure, longwave and global shortwave radiation are required as model input. The resulting dataset highlights the difference in meteorological influences driving ice volume evolution in the two study sites (Table 3.1).

3.1.4 Fountain observations

The fountain consists of a pipeline and a nozzle. The pipeline has three attributes, namely discharge rate (Q), height (h) and water temperature (T_F). "Discharge rate"

Tab. 3.1.: Summary of the weather observations for AIRs built during the respective study period. The weather measurements are shown using their mean (μ) and standard deviation (σ) during the study period as $\mu \pm \sigma$.

Name	Symbol	IN21	CH21	Units
Air temperature	T_a	0 ± 7	2 ± 6	°C
Relative humidity	RH	35 ± 20	79 ± 18	%
Wind speed	v_a	3 ± 1	2 ± 2	m/s
Direct Shortwave	SW_{direct}	246 ± 333	80 ± 156	$W m^{-2}$
Diffuse Shortwave	$SW_{diffuse}$	0 ± 0	58 ± 87	$W m^{-2}$
Hourly Precipitation	ppt	0 ± 0	139 ± 457	mm
Pressure	p_a	623 ± 3	794 ± 9	hPa

represents the discharge rate of the water in the fountain pipeline. "Height" denotes the height of the fountain pipeline installed. "Fountain water temperature" is the temperature of water droplets produced by the fountain.

The fountain nozzle has three characteristics, namely the aperture diameter (dia) and pressure loss (P_{nozzle}). "Pressure loss" denotes the loss of water head due to the fountain nozzle. Additionally, the observed ice radius formed from the fountain water droplets is denoted as spray radius (r_F) (Fig. 3.2).



Fig. 3.2.: Spray radius of the CH20 AIR

3.1.5 Drone flights

Several photogrammetric surveys were conducted for each of the AIRs. The details of these surveys and the methodology used to produce the corresponding outputs are explained in paper I. The Digital Elevation Maps (DEMs) generated from the obtained imagery were analysed to document the ice radius, the surface area and the volume of the ice structures. Ice radius measurements of drone flights which

Tab. 3.2.: List of all the studied AIRs. The study period starts when the fountain was first switched on (denoted as Start Date) and ends when the respective AIR either melted or broke into several ice blocks (denoted as Expiry Date).

Name	Start Date	Expiry Date	No. of flights	Spray radius
Traditional CH20	Jan 3 2020	Apr 6 2020	2	7.7 m
Traditional CH21	Nov 22 2020	May 10 2021	8	6.9 m
Traditional IN21	Jan 18 2021	June 20 2021	6	10.2 m
Traditional CH22	Dec 8 2021	April 12 2022	8	4.1 m
Automated CH22	Dec 8 2021	April 12 2022	6	4.8 m

observed either an increase in AIR circumference or volume were averaged to determine the fountain's spray radius. The number of drone surveys conducted for each of the AIRs and the corresponding spray radius observed is shown in Table 3.2.

3.2 AIR Model

A bulk energy and mass balance model is used to calculate the amounts of ice, meltwater, water vapour and wastewater of the AIR. In each hourly time step, the model uses the AIR surface area, energy balance and mass balance calculations to estimate its ice volume, surface temperature and wastewater as shown in Fig. 3.3.

3.2.1 Surface area calculation

The model assumes the AIR shape to be a cone and assigns the following shape attributes:

$$A_{cone}^i = \pi \cdot r_{cone}^i \cdot \sqrt{(r_{cone}^i)^2 + (h_{cone}^i)^2} \quad (3.1a)$$

$$V_{cone}^i = \pi/3 \cdot (r_{cone}^i)^2 \cdot h_{cone}^i \quad (3.1b)$$

$$j_{cone}^i = \frac{\Delta M_{ice}^i}{\rho_{water} * A_{cone}^i} \quad (3.1c)$$

where i denotes the model time step, r_{cone}^i is the radius; h_{cone}^i is the height; A_{cone}^i is the surface area; V_{cone}^i is the volume and j_{cone}^i is the AIR surface normal thickness change as shown in Fig. 3.4. M_{ice}^i is the mass of the AIR and $\Delta M_{ice}^i = M_{ice}^{i-1} - M_{ice}^{i-2}$.

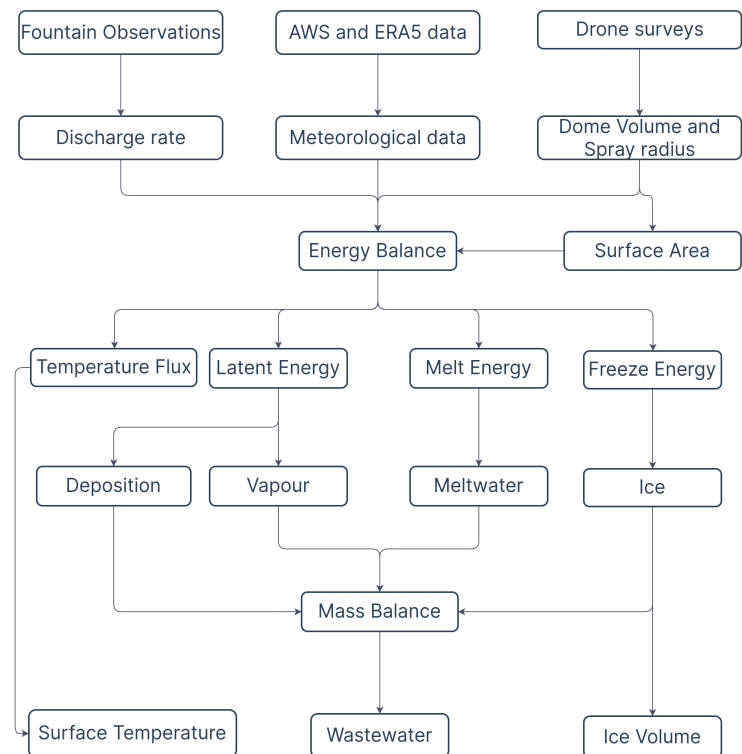


Fig. 3.3.: Model schematic showing the workflow used in the model at every time step.

Henceforth, the equations used display the model time step superscript i only if it is different from the current time step.

AIR density can be defined as:

$$\rho_{cone} = \frac{M_F + M_{dep} + M_{ppt}}{(M_F + M_{dep})/\rho_{ice} + M_{ppt}/\rho_{snow}} \quad (3.2)$$

where M_F is the cumulative mass of the fountain discharge; M_{ppt} is the cumulative precipitation; M_{dep} is the cumulative accumulation through water vapour deposition; ρ_{ice} is the ice density (917 kg m^{-3}) and ρ_{snow} is the density of wet snow (300 kg m^{-3}) taken from Cuffey and Paterson, 2010 .

AIR volume can also be expressed as:

$$V_{cone} = \frac{M_{ice}}{\rho_{cone}} \quad (3.3)$$

The initial radius of the AIR is assumed to be r_F . The initial height h_0 depends on the dome volume V_{dome} used to construct the AIR as follows:

$$h_0 = \Delta x + \frac{3 \cdot V_{dome}}{\pi \cdot (r_F)^2} \quad (3.4)$$

where Δx is the surface layer thickness (defined in Section 3.2.2)

During the subsequent time steps, the dimensions of the AIR evolve assuming a uniform thickness change (j_{cone}) across its surface area with an invariant slope $s_{cone} = \frac{h_{cone}}{r_{cone}}$. During these time steps, the volume is parameterised using Eqn. 3.1b as:

$$V_{cone} = \frac{\pi \cdot (r_{cone})^3 \cdot s_{cone}}{3} \quad (3.5)$$

We define the ice stupa boundary through its spray radius, i.e. we assume ice formation is negligible when $r_{cone} > r_F$. Combining Eqns. 3.1b, 3.3, 3.4 and 3.5, the geometric evolution of the Ice stupa at each time step i can be determined by considering the following rules:

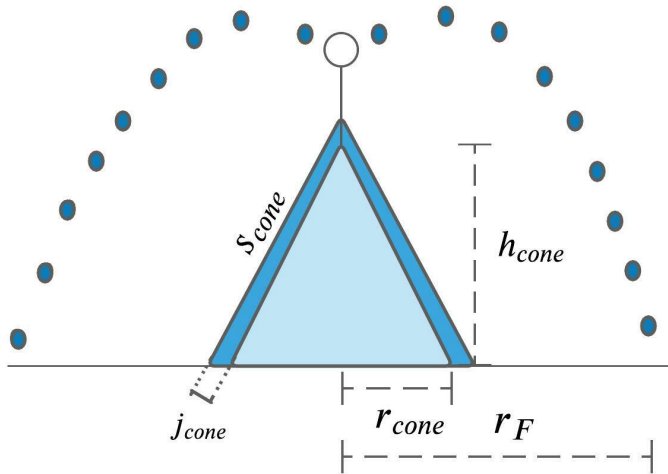


Fig. 3.4.: Shape variables of the AIR. r_{cone} is the radius, h_{cone} is the height, j_{cone} is the thickness change and s_{cone} is the slope of the ice cone. r_F is the spray radius of the fountain.

$$(r_{cone}, h_{cone}) = \begin{cases} (r_F, h_0) & \text{if } i = 0 \\ (r_{cone}^{i-1}, \frac{3 \cdot M_{ice}}{\pi \cdot \rho_{ice} \cdot (r_{cone}^{i-1})^2}) & \text{if } r_{cone}^{i-1} \geq r_F \text{ and } \Delta M_{ice} > 0 \\ (\frac{3 \cdot M_{ice}}{\pi \cdot \rho_{ice} \cdot s_{cone}})^{1/3} \cdot (1, s_{cone}) & \text{otherwise} \end{cases} \quad (3.6)$$

3.2.2 Energy balance calculation

We approximate the energy balance at the surface of an AIR by a one-dimensional description of energy fluxes into and out of a (thin) layer with thickness Δx :

$$\rho_{cone} \cdot c_{ice} \cdot \frac{\Delta T}{\Delta t} \cdot \Delta x = q_{SW} + q_{LW} + q_L + q_S + q_F + q_R + q_G \quad (3.7)$$

Upward and downward fluxes relative to the ice surface are positive and negative, respectively. The first term is the energy change of the surface layer, which can be translated into a phase change energy should phase changes occur. q_{SW} is the net shortwave radiation; q_{LW} is the net longwave radiation; q_L and q_S are the turbulent latent and sensible heat fluxes. q_F and q_R represent the heat exchange of the fountain water droplets and rain droplets with the AIR ice surface respectively. q_G represents ground heat flux between the AIR surface and its interior.

The energy flux acts upon the AIR surface layer, which has an upper and lower boundary defined by the atmosphere and the ice body of the AIR, respectively. Here, we define the surface temperature T_{ice} to be the modelled average temperature of the ice stupa surface layer.

Net Shortwave Radiation q_{SW}

The net shortwave radiation q_{SW} is computed as follows:

$$q_{SW} = (1 - \alpha) \cdot (SW_{direct} \cdot f_{cone} + SW_{diffuse}) \quad (3.8)$$

where SW_{direct} and $SW_{diffuse}$ are the direct and diffuse shortwave radiation, α is the modelled albedo and f_{cone} is the area fraction of the ice structure exposed to the direct shortwave radiation.

The albedo varies depending on the water source that formed the current AIR surface layer. During the fountain runtime, the albedo assumes a constant value corresponding to ice albedo. However, after the fountain is switched off, the albedo can reset to snow albedo during snowfall events and then decay back to ice albedo. We use the scheme described in Oerlemans and Knap, 1998 to model this process. The scheme records the decay of albedo with time after fresh snow is deposited on the surface. δt records the number of time steps after the last snowfall event. After snowfall, albedo changes over a time step, δt , as

$$\alpha = \alpha_{ice} + (\alpha_{snow} - \alpha_{ice}) \cdot e^{(-\delta t)/\tau} \quad (3.9)$$

where α_{ice} is the bare ice albedo value (0.25), α_{snow} is the fresh snow albedo value (0.85) and τ is a decay rate (16 days), which determines how fast the albedo of the ageing snow recedes back to ice albedo. Discharge events decrease the decay rate by a factor of $\alpha_{ice}/\alpha_{snow}$.

The solar area fraction f_{cone} of the ice structure exposed to the direct shortwave radiation depends on the shape considered. Using the solar elevation angle θ_{sun} , the solar beam can be considered to have a vertical component, impinging on the horizontal surface (semicircular base of the AIR), and a horizontal component impinging on the vertical cross section (a triangle). The solar elevation angle θ_{sun} used is modelled using the parametrization proposed by Woolf, 1968. Accordingly, f_{cone} is determined as follows:

$$f_{cone} = \frac{(0.5 \cdot r_{cone} \cdot h_{cone}) \cdot \cos\theta_{sun} + (\pi \cdot (r_{cone})^2/2) \cdot \sin\theta_{sun}}{\pi \cdot r_{cone} \cdot ((r_{cone})^2 + (h_{cone})^2)^{1/2}} \quad (3.10)$$

The diffuse shortwave radiation is assumed to impact the conical AIR surface uniformly.

Net Longwave Radiation q_{LW}

The net longwave radiation q_{LW} is determined as follows:

$$q_{LW} = LW_{in} - \sigma \cdot \epsilon_{ice} \cdot (T_{ice} + 273.15)^4 \quad (3.11)$$

where T_{ice} is the modelled surface temperature given in $[\text{ }^\circ\text{C}]$, $\sigma = 5.67 \cdot 10^{-8} \text{ J m}^{-2} \text{ s}^{-1} \text{ K}^{-4}$ is the Stefan-Boltzmann constant, LW_{in} denotes the incoming longwave radiation and ϵ_{ice} is the corresponding emissivity value for the Icestupa surface (0.97).

The incoming longwave radiation LW_{in} for the Indian site, where no direct measurements were available, is determined as follows:

$$LW_{in} = \sigma \cdot \epsilon_a \cdot (T_a + 273.15)^4 \quad (3.12)$$

here T_a represents the measured air temperature and ϵ_a denotes the atmospheric emissivity. We approximate the atmospheric emissivity ϵ_a using the equation suggested by Brutsaert, 1982, considering air temperature and vapor pressure (Eqn. 3.13). The vapor pressure of air over water and ice was obtained using Eqn. 3.16. The expression defined in Brutsaert, 1975 for clear skies (first term in equation 3.13) is extended with the correction for cloudy skies after Brutsaert, 1982 as follows:

$$\epsilon_a = 1.24 \cdot \left(\frac{p_{v,w}}{(T_a + 273.15)} \right)^{1/7} \cdot (1 + 0.22 \cdot cld^2) \quad (3.13)$$

with a cloudiness index cld , ranging from 0 for clear skies to 1 for complete overcast skies. For the Indian site, we assume cloudiness to be negligible.

Turbulent fluxes

The turbulent sensible q_S and latent heat q_L fluxes are computed with the following expressions proposed by Garratt, 1992:

$$q_S = \mu_{cone} \cdot c_a \cdot \rho_a \cdot p_a / p_{0,a} \cdot \frac{\kappa^2 \cdot v_a \cdot (T_a - T_{ice})}{\left(\ln \frac{h_{AWS}}{z_0}\right)^2} \quad (3.14)$$

$$q_L = \mu_{cone} \cdot 0.623 \cdot L_s \cdot \rho_a / p_{0,a} \cdot \frac{\kappa^2 \cdot v_a (p_{v,w} - p_{v,ice})}{\left(\ln \frac{h_{AWS}}{z_0}\right)^2} \quad (3.15)$$

where h_{AWS} is the measurement height above the ground surface of the Automatic Weather Station (AWS) (around 2 m for all sites), v_a is the wind speed in [$m s^{-1}$], c_a is the specific heat of air at constant pressure ($1010 J kg^{-1} K^{-1}$), ρ_a is the air density at standard sea level ($1.29 kg m^{-3}$), $p_{0,a}$ is the air pressure at standard sea level (1013 hPa), p_a is the measured air pressure, κ is the von Karman constant (0.4), z_0 is the surface roughness (3 mm) and L_s is the heat of sublimation (2848 $kJ kg^{-1}$). The vapor pressure of air with respect to water ($p_{v,w}$) and with respect to ice ($p_{v,ice}$) was obtained using the formulation given in Huang, 2018 :

$$p_{v,w} = e^{\frac{(34.494 - \frac{4924.99}{T_a + 237.1})}{(T_a + 105)^{1.57 \cdot 100}}} \cdot \frac{RH}{100} \quad (3.16)$$

$$p_{v,ice} = e^{\frac{(43.494 - \frac{6545.89}{T_{ice} + 278})}{(T_{ice} + 868)^{2 \cdot 100}}}$$

The dimensionless parameter μ_{cone} is an exposure parameter that deals with the fact that AIR has a rough appearance and forms an obstacle to the wind regime. This factor accounts for the larger turbulent fluxes due to the roughness of the surface (Oerlemans, Balasubramanian, et al., 2021), and is a function of the AIR slope as follows:

$$\mu_{cone} = 1 + \frac{s_{cone}}{2} \quad (3.17)$$

A possible source of error is the fact that wind measurements from the horizontal plane at the AWS are used, which might be different from those on a slope. However, without detailed datasets from the AIR surface, we retain this assumption.

Fountain discharge heat flux q_F

The fountain water temperature T_F is assumed to cool to $0\text{ }^{\circ}\text{C}$ after contact with the ice surface. T_F is equal to the measured source water temperature. But during time periods when the ambient temperature is subzero, T_F is assumed to be $0\text{ }^{\circ}\text{C}$. Thus, the heat flux caused by this process is:

$$q_F = \begin{cases} \frac{\Delta M_F \cdot c_{water} \cdot T_F}{\Delta t \cdot A_{cone}} & \text{if } T_{temp} > 0 \\ 0 & \text{otherwise} \end{cases} \quad (3.18)$$

with c_{water} as the specific heat of water ($4186\text{ J kg}^{-1}\text{K}^{-1}$).

Rain heat flux q_R

The influence of rain events on the albedo and on the Ice stupa's energy balance was assumed to be similar to that of discharge events. However, the water temperature of a rain event was assumed to equal to the air temperature. Accordingly, the heat flux generated due to a rain event was equal to:

$$q_R = \frac{\Delta M_{ppt} \cdot c_{water} \cdot T_a}{\Delta t \cdot A_{cone}} \quad (3.19)$$

Bulk Icestupa heat flux q_G

The bulk ice stupa heat flux q_G corresponds to the ground heat flux in normal soils and is caused by the temperature gradient between the surface layer (T_{ice}) and the ice body (T_{bulk}). It is expressed by using the heat conduction equation as follows:

$$q_G = k_{ice} \cdot (T_{bulk} - T_{ice}^{i-1}) / l_{cone} \quad (3.20)$$

where k_{ice} is the thermal conductivity of ice ($2.123\text{ W m}^{-1}\text{ K}^{-1}$), T_{bulk} is the mean temperature of the ice body within the ice stupa and l_{cone} is the average distance of any point in the surface to any other point in the ice body. T_{bulk} is initialised as $0\text{ }^{\circ}\text{C}$ and later determined from Eqn. 3.20 as follows:

$$T_{bulk}^{i+1} = T_{bulk} - (q_G \cdot A \cdot \Delta t) / (M_{ice} \cdot c_{ice}) \quad (3.21)$$

Since AIRs typically have conical shapes with $r_{cone} > h_{cone}$, we assume that the center of mass of the cone body is near the base of the fountain. Thus, the distance of every point in the AIR surface layer from the cone body's center of mass is between h_{cone} and r_{cone} . Therefore, we calculate q_G assuming $l_{cone} = (r_{cone} + h_{cone})/2$.

Phase changes

This section explains the numerical procedures to model phase changes at the surface layer. Let T_{temp} be the calculated surface temperature. Therefore, Eqn. 3.7 can be rewritten as:

$$q_{total} = \rho_{ice} \cdot c_{ice} \cdot \frac{(T_{temp} - T_{ice})}{\Delta t} \cdot \Delta x$$

where q_{total} represents the total energy available to be redistributed. Even if the numerical heat transfer solution produces temperatures which are $T_{temp} > 0^\circ C$, say from intense shortwave radiation, the ice temperature must remain at $T_{temp} = 0^\circ C$. The “excess” energy is used to drive the melting process. Moreover, the energy input is used to melt the surface ice layer, and not to raise the surface temperature to some unphysical value. Similarly, for freezing to occur, three conditions are required. Firstly, fountain water is present ($\Delta M_F > 0$) and secondly the calculated temperature of the ice, T_{temp} , is below $0^\circ C$. However, these two conditions are not sufficient as the latent heat turbulent fluxes can only contribute to temperature fluctuations. Therefore, an additional condition, namely, $(q_{total} - q_L) < 0$, is required. Depending on the above conditions, the total energy q_{total} can be redistributed for the melting (q_{melt}), freezing (q_{freeze}) and surface temperature change (q_T) processes as follows:

$$q_{total} = \begin{cases} q_{freeze} + q_T & \text{if } \Delta M_F > 0 \text{ and } T_{temp} < 0 \text{ and } (q_{total} - q_L) < 0 \\ q_{melt} + q_T & \text{otherwise} \end{cases} \quad (3.22)$$

Henceforth, time steps when the the total energy is redistributed to the freezing energy are called freezing events and the rest of the time steps are called melting events.

During a freezing event, the AIR surface is assumed to warm to $0^\circ C$. The available energy ($q_{total} - q_L$) is further increased due to this change in surface temperature represented by the energy flux:

$$q_0 = \frac{\rho_{ice} \cdot \Delta x \cdot c_{ice} \cdot T_{ice}^{i-1}}{\Delta t}$$

The available fountain discharge (ΔM_F) may not be sufficient to utilize all the freezing energy. At such times, the additional freezing energy further cools down the surface temperature. Accordingly, the surface energy flux distribution during a freezing event can be represented as:

$$(q_{freeze}, q_T) = \begin{cases} \left(\frac{\Delta M_F \cdot L_f}{A_{cone} \cdot \Delta t}, q_{total} + \frac{\Delta M_F \cdot L_f}{A_{cone} \cdot \Delta t} \right) & \text{if } \Delta M_F \text{ insufficient} \\ (q_{total} - q_L + q_0, q_L - q_0) & \text{otherwise} \end{cases} \quad (3.23)$$

If $T_{temp} > 0^\circ C$, then energy is reallocated from q_T to q_{melt} to maintain surface temperature at melting point. The total energy flux distribution during a melting event can be represented as:

$$(q_{melt}, q_T) = \begin{cases} (0, q_{total}) & \text{if } T_{temp} \leq 0 \\ \left(\frac{T_{temp} \cdot \rho_{ice} \cdot c_{ice} \cdot \Delta x}{\Delta t}, q_{total} - \frac{T_{temp} \cdot \rho_{ice} \cdot c_{ice} \cdot \Delta x}{\Delta t} \right) & \text{if } T_{temp} > 0 \end{cases} \quad (3.24)$$

3.2.3 Mass balance calculation

The mass balance equation for an AIR is represented as:

$$\frac{\Delta M_F + \Delta M_{ppt} + \Delta M_{dep}}{\Delta t} = \frac{\Delta M_{ice} + \Delta M_{water} + \Delta M_{sub} + \Delta M_{waste}}{\Delta t} \quad (3.25)$$

where M_F is the cumulative mass of the fountain discharge; M_{ppt} is the cumulative precipitation; M_{dep} is the cumulative accumulation through water vapour deposition; M_{ice} is the cumulative mass of ice; M_{water} is the cumulative mass of melt water; M_{sub} represents the cumulative water vapor loss by sublimation and M_{waste} represents the fountain wastewater that did not interact with the AIR. The left hand side of equation 3.25 represents the rate of mass input and the right hand side represents the rate of mass output for an AIR.

Precipitation input is calculated as shown in equation 3.26b where ρ_w is the density of water (1000 kg m^{-3}), $\Delta ppt/\Delta t$ is the measured precipitation rate in [$m s^{-1}$] and T_{ppt} is the temperature threshold below which precipitation falls as snow. Here,

snowfall events were identified using T_{ppt} as $1^{\circ}C$. Snow mass input is calculated by assuming a uniform deposition over the entire circular footprint of the AIR.

The latent heat flux is used to estimate either the evaporation and condensation processes or sublimation and deposition processes as shown in equation 3.26c. During the time steps at which the surface temperature is below $0^{\circ}C$ only sublimation and deposition can occur, but if the surface temperature reaches $0^{\circ}C$, evaporation and condensation can also occur. As the differentiation between evaporation and sublimation (and condensation and deposition) when the air temperature reaches $0^{\circ}C$ is challenging, we assume that negative (positive) latent heat fluxes correspond only to sublimation (deposition), i.e. no evaporation (condensation) is calculated.

Since we have categorized every time step as a freezing or melting event, we can determine the melting/freezing rates and the corresponding meltwater/ice quantities as shown in equations 3.26e, 3.26d and 3.26f. Having calculated all other mass components, the fountain wastewater generated every time step can be calculated using Eqn. 3.25.

$$\frac{\Delta M_F}{\Delta t} = \begin{cases} \frac{60}{\rho_w \cdot \Delta t} \cdot d_F & \text{if fountain is on} \\ 0 & \text{otherwise} \end{cases} \quad (3.26a)$$

$$\frac{\Delta M_{ppt}}{\Delta t} = \begin{cases} \pi \cdot (r_{cone})^2 \cdot \rho_w \cdot \frac{\Delta ppt}{\Delta t} & \text{if } T_a < T_{ppt} \\ 0 & \text{if } T_a \geq T_{ppt} \end{cases} \quad (3.26b)$$

$$\left(\frac{\Delta M_{dep}}{\Delta t}, \frac{\Delta M_{sub}}{\Delta t} \right) = \begin{cases} \frac{q_L \cdot A_{cone}}{L_s} \cdot (1, 0) & \text{if } q_L \geq 0 \\ \frac{q_L \cdot A_{cone}}{L_s} \cdot (0, -1) & \text{if } q_L < 0 \end{cases} \quad (3.26c)$$

$$\frac{\Delta M_{water}}{\Delta t} = \frac{q_{melt} \cdot A_{cone}}{L_f} \quad (3.26d)$$

$$\frac{\Delta M_{freeze/melt}}{\Delta t} = \frac{q_{freeze/melt} \cdot A_{cone}}{L_f} \quad (3.26e)$$

$$\frac{\Delta M_{ice}}{\Delta t} = \frac{q_{freeze} \cdot A_{cone}}{L_f} + \frac{\Delta M_{ppt}}{\Delta t} + \frac{\Delta M_{dep}}{\Delta t} - \frac{\Delta M_{sub}}{\Delta t} - \frac{\Delta M_{water}}{\Delta t} \quad (3.26f)$$

Considering AIRs as water reservoirs, their net water loss can be defined as:

$$\text{Net water losses} = \frac{M_{waste} + M_{sub}}{(M_F + M_{ppt} + M_{dep})} \cdot 100 \quad (3.27)$$

3.2.4 Uncertainty Quantification

The uncertainty in the model of estimating ice volumes is caused by three sources, namely model forcing data, model hyperparameters and model parameters. Model forcing data can further be divided into weather and fountain forcing data. Significant uncertainty exists in the weather forcing data, particularly for all the radiation measurements (SW_{direct} , $SW_{diffuse}$, LW_{in}) since they were taken from ERA5 dataset or an AWS far away from the construction sites. Since no other weather datasets exist for comparison, especially near the IN21 AIR, we are not accounting for uncertainties related to meteorological forcing data in this analysis. Uncertainty in the fountain forcing data arises due to only some fountain parameters listed in Table 3.3. Fountain runtime t_F has no uncertainty for the Swiss AIRs because no interruptions occurred during the study period. However, significant uncertainty exists for the IN21 AIR, where the interruptions due to pipeline freezing events happened overnight but this was ignored in this analysis. Fountain spray radius r_F was measured using the drone survey and therefore also doesn't contribute to model uncertainty. The choice of mean discharge rate d_F for both sites was just a best guess, based on a few observations made by the flowmeter. So we associate this parameter with a large uncertainty of $\pm 50\%$. For the fountain water temperature T_F , we assumed an upper bound of $3^{\circ}C$ since it is unlikely for it to have been beyond this range considering winter conditions at all the sites. The model structure introduces uncertainty through the spatial and temporal hyperparameters Δx and Δt . By definition, Δx is directly proportional to Δt . Therefore, we fix the temporal resolution of the model at hourly timesteps and only investigate the uncertainty caused by Δx here. Since the surface layer thickness for an AIR does not resemble any parameters in the glaciological literature, we attribute a wide range of values to it (from 1 cm to 10 cm). The model parameters are henceforth called as weather parameters to distinguish them from the fountain forcing parameters. These were fixed within a range based on literature values (Table 3.3).

The three types of uncertain parameters, namely model hyperparameters (Δx), fountain forcing parameters (d_F, T_F) and weather parameters ($\epsilon_{ice}, z_0, \alpha_{ice}, \alpha_{snow}, T_{ppt}, \tau$) are denoted as Q^M, Q^F and Q^W henceforth. Together, these nine parameters cause a large uncertainty in the ice volume estimates. In order to reduce this uncertainty, we perform a global sensitivity analysis with the net water loss as our objective. The objective of this sensitivity analysis was to reduce the dimension of the parameter space by calibrating the parameters with high total-order sensitivities ($S_{T_j} > 0.5$). The methodology to determine S_{T_j} is described in Appendix A.2. These sensitive model parameters were calibrated based on the Root Mean Squared Error (RMSE)

between the drone surveys and the model estimations of the ice volume. For this calibration procedure, all the other parameters were set to the median value of their respective ranges defined in Table 3.3. The sensitivity analysis and calibration were carried out with the drone surveys of CH21 and IN21 AIRs.

The model uncertainty was quantified separately for the remaining parameters in Q^M , Q^F and Q^W using the corresponding 90 % prediction interval I^M , I^F and I^W . The 90 % prediction interval, I^k , gives us the interval within which 90 % of the ice volume outcomes occur when all the parameters in Q^k are varied assuming each has an independent uniform probability density function. 5 % of the outcomes are above and 5 % are below this interval. The methodology to obtain this is described in Appendix A.2.

For validation, the calibrated model was tested with two datasets, namely the expiry date of all AIRs and the drone surveys of CH20 AIR.

3.3 Model calibration, uncertainty and validation

3.3.1 Calibration of sensitive parameters

The total-order sensitivities of all the nine parameters with respect to the net water loss objective are shown in Fig. 3.5 (a). In total, the global sensitivity analysis required 1432 model runs to determine these sensitivities for each site. The only sensitive parameter ($S_{T_j} > 0.5$) for both AIRs was the surface layer thickness. The RMSE between the drone surveys and the model ice volume estimates for different surface layer thickness are shown in Fig. 3.5 (b). The optimum value of Δx was found to be 45 mm and 65 mm with an RMSE of 9 m^3 and 30 m^3 for CH21 and IN21 AIRs respectively.

3.3.2 Weather and fountain forcing uncertainty quantification

The uncertainty in the ice volume estimates caused by the weather and fountain forcing parameters are shown in Fig. 3.6. The ranges highlighted represent the corresponding 90 % prediction interval of the ice volume estimates. Weather uncertainty determination required 422 simulations whereas fountain forcing uncertainty determination required 32 simulations for each AIR. Since the results presented below differ significantly during the fountain runtime, we divided the simulation

Tab. 3.3.: Free parameters in the model categorised as constant, derived, model hyperparameters, weather and fountain forcing parameters with their respective values/ranges.

Constant Parameters	Symbol	Value	Unit	Refs
Van Karman constant	κ	0.4	dimensionless	Cuffey and Paterson et al., 2000
Stefan Boltzmann constant	σ	5.67×10^{-8}	$W m^{-2} K^{-4}$	Cuffey and Paterson et al., 2000
Air pressure at sea level	$p_{0,a}$	1013	hPa	T. Mölg and Harder et al., 2007
Density of water	ρ_w	1000	$kg m^{-3}$	Cuffey and Paterson et al., 2000
Density of ice	ρ_{ice}	917	$kg m^{-3}$	Cuffey and Paterson et al., 2000
Density of air	ρ_a	1.29	$kg m^{-3}$	T. Mölg and Harder et al., 2007
Specific heat of water	c_w	4186	$J kg^{-1} {}^\circ C^{-1}$	Cuffey and Paterson et al., 2000
Specific heat of ice	c_{ice}	2097	$J kg^{-1} {}^\circ C^{-1}$	Cuffey and Paterson et al., 2000
Specific heat of air	c_a	1010	$J kg^{-1} {}^\circ C^{-1}$	T. Mölg and Harder et al., 2007
Thermal conductivity of ice	k_{ice}	2.123	$W m^{-1} K^{-1}$	Bonales et al., 2013
Latent Heat of Sublimation	L_s	2.848×10^6	$J kg^{-1}$	Cuffey and Paterson et al., 2000
Latent Heat of Fusion	L_f	3.34×10^5	$J kg^{-1}$	Cuffey and Paterson et al., 2000
Gravitational acceleration	g	9.81	$m s^{-2}$	Cuffey and Paterson et al., 2000
Weather station height	h_{AWS}	2	m	assumed
Model timestep	Δt	3600	s	assumed
Fountain spray radius	r_F		m	measured
Fountain runtime	t_F		hours	measured
Derived Parameters	Symbol		Unit	Section
Radius of AIR	r_{cone}		m	3.2.1
Height of AIR	h_{cone}		m	3.2.1
Slope of AIR	s_{cone}		dimensionless	3.2.1
Thickness change of AIR	j_{cone}		m	3.2.1
Atmospheric emissivity	ϵ_a		dimensionless	3.2.2
Cloudiness	cld		dimensionless	assumed
Vapour pressure over water	$p_{v,w}$		hPa	3.2.2
Vapour pressure over ice	$p_{v,ice}$		hPa	3.2.2
Solar elevation angle	θ_{sun}		${}^\circ$	3.2.2
Albedo	α		dimensionless	3.2.2
Solar area fraction	f_{cone}		dimensionless	3.2.2
Ice body and surface distance	l_{cone}		m	3.2.2
AIR surface temperature	T_{ice}		${}^\circ C$	3.2.2
AIR bulk temperature	T_{bulk}		${}^\circ C$	3.2.2
Model Hyperparameters	Symbol	Range	Unit	Refs
Surface layer thickness	Δx	$[1 \times 10^{-2}, 1 \times 10^{-1}]$	m	assumed
Weather Parameters	Symbol	Range	Unit	Refs
Ice Emissivity	ϵ_{ice}	$[0.95, 0.99]$	dimensionless	Hori et al., 2006
Surface Roughness	z_0	$[1 \times 10^{-3}, 5 \times 10^{-3}]$	m	Brock et al., 2006
Ice Albedo	α_{ice}	$[0.15, 0.35]$	dimensionless	Steiner et al., 2011
Snow Albedo	α_{snow}	$[0.8, 0.9]$	dimensionless	Zolles et al., 2019
Precipitation Temperature threshold	T_{ppt}	$[0, 2]$	${}^\circ C$	ShiChang et al., 2019
Albedo Decay Rate	τ	$[10, 22]$	days	L. S. Schmidt et al., 2019
Fountain Forcing Parameters	Symbol	Range	Unit	Refs
Discharge rate	d_F	$[0.5 \cdot d_F, 1.5 \cdot d_F]$	l/min	assumed
Water temperature	T_F	$[0, 3]$	${}^\circ C$	assumed

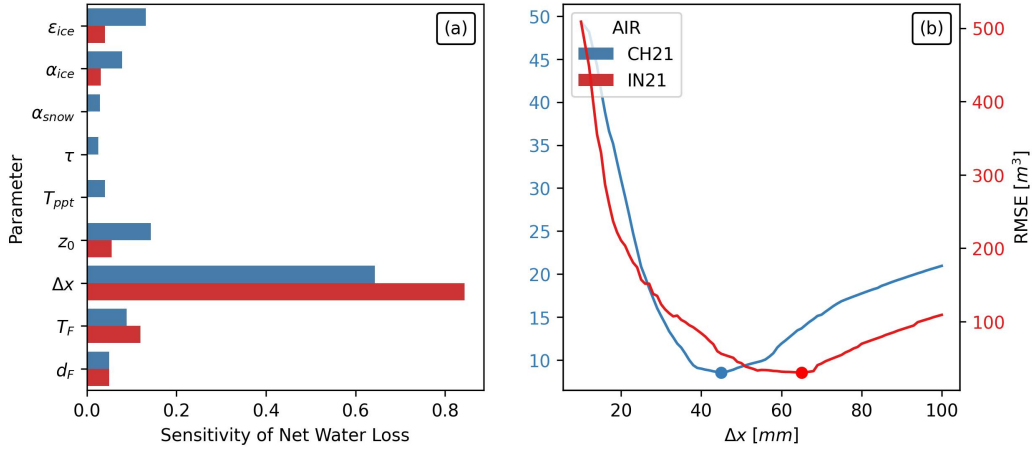


Fig. 3.5.: (a) Total-order sensitivities of all the uncertain parameters of the model with net water loss as the objective. (b) The calibration of the sensitive parameter, Δx with the RMSE between the drone and model estimates of the ice volume. The dots denote the optimum values. The estimates from the Swiss and Indian AIRs are denoted with blue and red colors respectively.

duration of the AIR into accumulation and ablation periods. The accumulation period ends and the ablation period starts after the last fountain discharge event.

The prediction interval of the weather and fountain forcing parameters behave differently during the accumulation and ablation period for all AIRs. Prediction interval of the weather parameters increase throughout the simulation period, but that of the fountain forcing parameters only increase during the accumulation period. This is to be expected since the fountain forcing parameters directly affect the model estimates only during the accumulation period.

Weather uncertainty for the Indian site was low compared to the Swiss one since precipitation and the associated variation in albedo was negligible. At the end of the accumulation period, the Indian weather prediction interval had a magnitude of $73 m^3$ which was 10 % of the maximum simulated volume, whereas the magnitude of the Swiss weather prediction interval was much higher (28 % of the maximum simulated volume for the CH21 AIR). This was expected since four out of the six uncertain Indian weather parameters were part of the albedo module. Among all the weather parameters, surface roughness caused the most variance in both Indian and the Swiss ice volume estimates.

Fountain forcing uncertainty for the Indian site was higher than its weather uncertainty (28 % of the maximum simulated volume at the end of the accumulation period). This was predominantly due to the uncertainty in the fountain's water temperature. However, for the Swiss site, the prediction interval of the fountain forcing

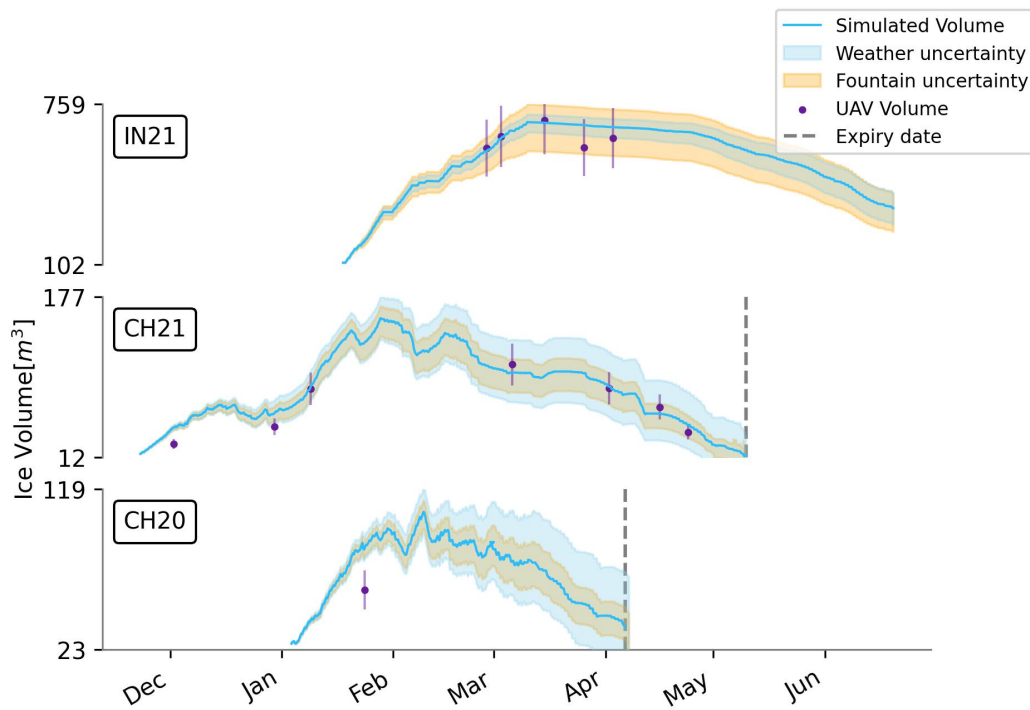


Fig. 3.6.: Simulated ice volume during the lifetime of the AIRs (blue curve). The shaded regions (light blue and orange) represent the 90% prediction interval of the AIR ice volume caused by the variations in weather and fountain forcing parameters, respectively. Violet points indicate the drone ice volume observations. The grey dashed line represents the observed expiry date for each AIR.

parameters was similar to that of the weather parameters during the accumulation period. Since the mean fountain discharge rate of the Indian location was eight times that of the Swiss, the uncertainty due to the fountain forcing parameters was expected to be larger for the Indian location.

3.3.3 Validation

Model performance can be judged based on the ice volume left on the expiry date of all AIRs. In the case of CH21 AIR no ice volume was left whereas for CH20 AIR ice volume of 12 m^3 was left on the expiry date. For the IN21 AIR, the determination of the expiry date was not possible. In reality, the IN21 AIR was found to have disintegrated into several ice blocks on 20th June, 2021.

There was also one drone survey of the CH20 AIR volume for validation purposes. The RMSE of that observation with the modelled volume was 19 m^3 which is 18 % of the maximum simulated ice volume of CH20 AIR.

3.4 Model limitations and suggestions for improvement

Model development is an art where subjective choices seek a balance between a model's simplicity and its accuracy. Below we detail some of these choices and recommend strategies that shift this balance towards further model accuracy.

3.4.1 Quality and quantity of calibration and validation datasets

The methodology used to acquire the radius, area and volume of AIRs (Appendix A.1) from each drone survey has several drawbacks. The calibration and validation process used has an inherent temporal and spatial bias due to the following subjective choices:

- **The number and timing of the drone surveys.** For example, among the five surveys of IN21 AIR, most of them were conducted around early March when the AIR volume was near its maximum whereas the seven surveys of the CH21 location were more evenly spaced out in comparison.
- **The weather conditions under which surveys were performed.** Particularly, precipitation events reduce DEM quality since they create uniform snow surfaces over AIRs. These surfaces dont have many identifiable features that can be used to extract the radius and area of the AIR.

Thus, the quality of AIR calibration and validation is severely limited by the high uncertainties attached with the drone processing methodology.

This limitation can be overcome by extending the model validation set with daily AIR meltwater measurements. However, the study site needs to satisfy two conditions in order to do this. First, the terrain of the site needs to be waterproof and oriented so that most of the AIR runoff can be collected. Second, the chosen location should not have high wind speeds, otherwise a significant fraction of AIR wastewater would be dispersed in the air.

3.4.2 Turbulent heat flux parametrization

The method used to calculate turbulent heat fluxes by Garratt (1992) assumes that these fluxes are acting over a uniform planar surface. This leads us to use the exposure/roughness parameter μ as a correction factor. However, equation 3.17

about μ is no more than an educated guess. It is hard to base estimates of this parameter on information in the literature. Many studies have been carried out on the effect of obstacles on atmospheric boundary layer flow (e.g. trees), but always in an ensemble setting, looking at the bulk effect of an ensemble of obstacles. We deal with a case of a single obstacle in open terrain, and we are confident that the roughness of the surface and the exposure will lead to larger turbulent fluxes.

3.4.3 Fountain quantification

Contrary to our model assumptions, the parameters used to define the fountain were not independent. The fountain height, fountain aperture diameter (both ignored in this analysis), discharge rate, water temperature and spray radius were related through the trajectories of the water droplets.

The model requires the fountain spray radius to be provided as input. This is a significant limitation since the model is very sensitive to the spray radius parameter. Moreover, spray radius is not only determined by the fountain characteristics but also due to wind-driven redistribution, refreezing and melting events across the AIR perimeter. The same fountain was observed to produce different spray radius corresponding to different winters for the Swiss experiments. Further discussion on this can be found at Section 5.1.3.

During the IN21 experiment, snow formation was observed, indicating that the fountain water droplets have the potential to freeze before deposition on the AIR surface. Modelling such processes would require modelling the conduction, convection and nucleation processes that all droplets undergo during their flight time. Therefore, a proper quantification of the fountain is much more complex and requires a closer look at the correlation of the fountain parameters amongst themselves and with the weather parameters.

3.4.4 Shape parameterization

The RMSE between the drone and the model estimates of the surface area for the IN21, CH21 and CH20 AIRs were 69 %, 25 % and 65 % of the maximum area of the respective AIRs. There are two crude assumptions that lead to such a large error, namely assuming a conical shape and assuming a constant spray radius.

Better quantification of the surface area can be achieved by assuming AIR cross section to be a Gaussian curve rather than a triangle.

Better quantification of the spray radius can be achieved by modelling the projectile motion of fountain water droplets using wind speed values and fountain characteristics as illustrated in Section 5.1.3.

3.4.5 Albedo parametrization

The albedo parametrization illustrated by Equation 3.9 had to be modified to accommodate the fountain discharge events. Little knowledge is available to understand the decay of albedo due to such events. Therefore, a simplistic approach of increasing the decay rate by a constant factor is used. However, the value of this factor is chosen without any basis on measurements. Field based albedo measurements are required to better parametrize the effect of water spray on the surface albedo decay rate.

3.4.6 COSISTUPA: COSIPY + AIR model

The model, in its current form, is not expected to perform well for locations where it has not been calibrated for before. This limits its ability to identify and classify other favourable locations worldwide.

In this section, we showcase a strategy to improve the AIR model's transferability to new locations. Specifically, the surface layer thickness parameter requires prior calibration for better model performance. However, the dependence of the model on this parameter can be removed if spatial temperature fluctuations across the ice structure are resolved.

In order to remove the calibration requirements for model performance, we combine the AIR model with the COupled Snowpack and Ice surface energy and mass balance model in PYthon (COSIPY). COSIPY is typically used for modelling distributed snow and glacier mass changes (Sauter et al., 2020). However, its flexible, user-friendly and modular framework makes it an ideal platform to implement the alternate modules required for modelling ice reservoirs. This modified COSIPY model will be referred to as COSISTUPA model henceforth.

Model configuration

In this section, we describe the main adjustments needed to convert COSIPY modules into the COSISTUPA model.

The COSIPY model input was extended to include discharge rate and cloudiness index measurements. Additionally, spray radius parameter was provided as input during model initialization. The model initialization of the ice cone dimensions were made identical to the AIR model.

Several parametrizations are available for estimating each of the surface processes in COSIPY. Most of the ones used in the AIR model are among the available options. But some required minor modifications to be applicable for processes on a conical surface. Additionally, new parametrizations were required to estimate the conical shape evolution and model the freezing process due to the fountain discharge events. To extend COSIPY into COSISTUPA, parametrizations of the following processes were modified:

- **Fountain rain heat flux** : The heat flux generated due to the difference in fountain water droplet temperature and surface temperature was introduced as a new energy balance component. This implementation is identical to that described in Sec. 3.2.2
- **Turbulent flux scaling** : The sensible and the latent heat fluxes were scaled by the μ_{cone} factor introduced in Sec. 3.2.2
- **Freezing process** : Phase transition processes were introduced during time periods when the fountain discharge was active. These processes created new ice layers whenever the energy balance allowed it following the algorithm introduced in Sec. 3.2.2
- **Conical shape evolution** : The surface mass balance estimation was converted to the volume estimation through the methodology introduced in Sec. 3.2.1

Please note the above list of changes are not exhaustive and represent only the major modifications necessary to develop the COSISTUPA model.

Advantages of the COSISTUPA model

The COSISTUPA model has a modular structure so that the exchange of routines or parametrizations of physical processes is possible with little effort for the user. The framework consists of a computational kernel, which forms the runtime environment and takes care of the initialization, the input-output routines, and the parallelization, as well as the grid and data structures. This structure offers maximum flexibility without having to worry about the internal numerical flow. The adaptive subsurface scheme allows an efficient and fast calculation of the otherwise computationally

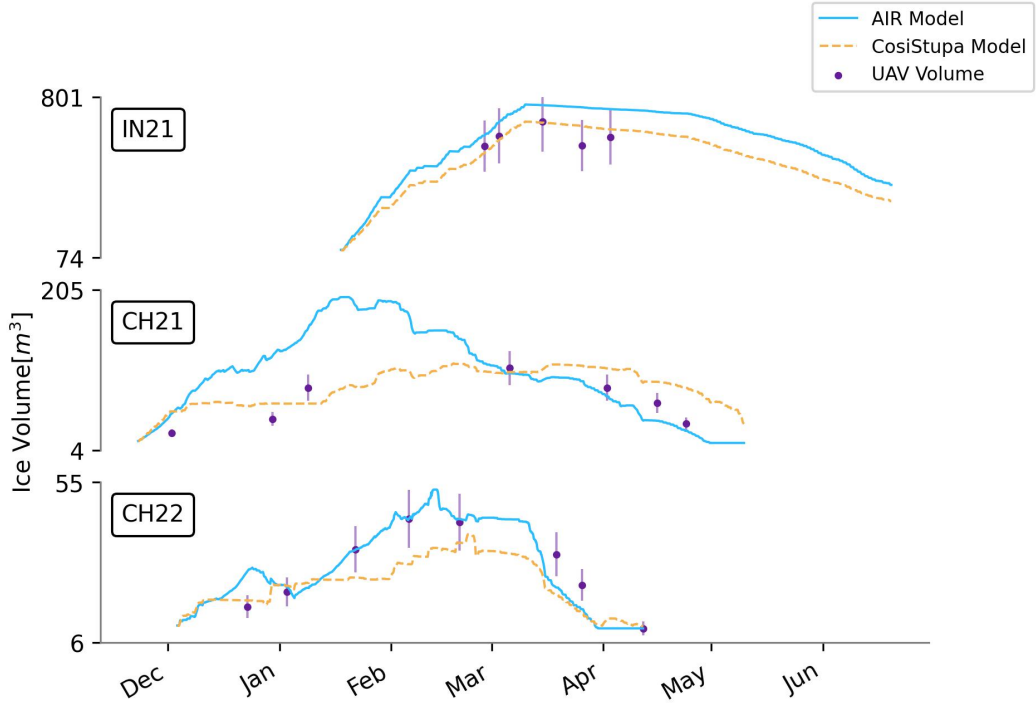


Fig. 3.7.: Comparison of volume estimates generated from the AIR and COSISTUPA models.

demanding fundamental equations. The surface energy balance scheme uses established standard parametrizations for radiation as well as for the energy exchange between the atmosphere and surface. The schemes are coupled by solving both surface energy balance and subsurface fluxes iteratively such that consistent skin temperature is returned at the interface. COSISTUPA uses a one-dimensional approach limited to the vertical fluxes of energy and matter but neglects any lateral processes. Accordingly, the model can be easily set up in parallel computational environments for calculating both energy balance and climatic surface mass balance of multiple AIRs based on flexible horizontal grids and with varying temporal resolution.

The RMSE error of the 5 icestupas studied in this thesis were within 20 % of their maximum ice volumes for both the models (Fig. 3.7). However, the COSISTUPA model was 3 times slower than the AIR model. This is likely due to the additional effort required to resolve the ice temperature spatially.

We consider the COSISTUPA model to be the better one among the two models due to these three reasons:

- **Better spatial temperature and density resolution :** It provides temperature and density information of subsurface layers of the AIR. In contrast, the

AIR model only computes the bulk and the surface temperature. Moreover, COSISTUPA is better able to approximate bulk density since it has records of previous snowfall events in its subsurface layers.

- **Better parametrization of snowfall** : The densification and albedo decay of snowfall are better handled in COSISTUPA due to its awareness of the snowfall content in each of its subsurface layers.
- **Better validation** : COSISTUPA, being a model derived from COSIPY is expected to validate better since the core parametrizations are unchanged and have been extensively validated before (Arndt et al., 2021).
- **Future support** : COSISTUPA will be extensively supported in the future through the COSIPY community.

Technology of ice reservoirs

“ In building ice stupas, it's necessary to engage enough workforce to extract the water over long distances and to keep water flowing in cold temperatures.

— Marcus Nüsser
(Professor, South Asia Institute)

There is a long tradition of developing ice harvesting structures in the upper Indus Basin, in both Ladakh, northern India (Labbal, 2000; Marcus Nüsser, S. Schmidt, et al., 2012) and various locations in northern Pakistan (Kreutzmann, 2011). AIRs, located at much lower altitudes than naturally occurring glaciers, serve to bridge the critical gap in water availability by providing meltwater earlier in the agricultural season. Such ice reservoirs utilize the hydrological process of icing under local conditions of frequent freeze-thaw cycles to capture water for seasonal storage. They are not water storage structures that freeze from the top down, rather they are produced through sequential, freezing of thin layers of water creating superimposed sheets of ice.

In this chapter, we present the various types of ice reservoirs that exist (Fig. 4.1), describe their construction strategy and explore the benefits of automated construction strategies.

4.1 Types of ice reservoirs

4.1.1 Ice terraces

According to oral history and corona imagery from 1969, the first ice terraces are older than 50 years and can be found in Phuktse and Igoo villages of Ladakh. Over the past 30 years, 14 ice terraces have been constructed in central Ladakh, located in tributary valleys of the Indus (Norphel, 2009; M. Nüsser et al., 2019). Chewang Norphel, a well known engineer of the Leh Nutrition Project, introduced this practice

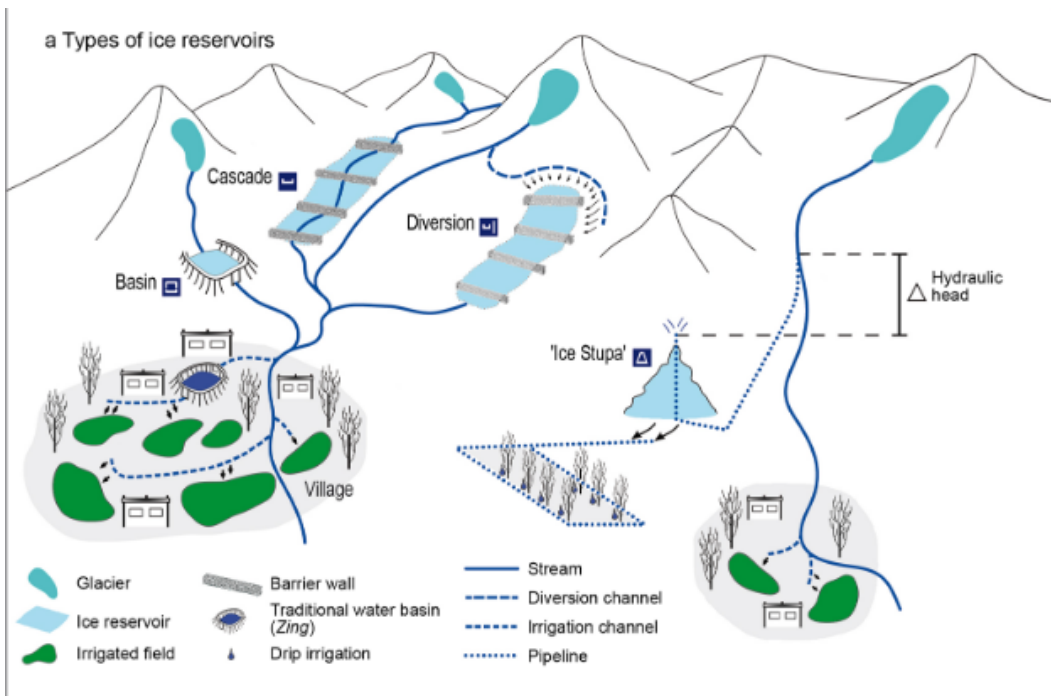


Fig. 4.1.: Different types of ice reservoirs. Adapted from M. Nüsser et al., 2019

to Ladakh (Vince, 2009). Cascades and diversions shown in Fig. 4.1 constitute the ice terrace type of AIRs.

There are two distinct types of ice terraces with site-specific modifications as shown in Fig. 4.1: the first type is built as cascades on perennial streams. A series of loose rock walls in the river bed reduces flow velocity, but still lets water pass through. Such cascades allow flowing water to freeze on exposed surfaces and form superimposed ice layers when temperatures drop (Fig. 4.3). An example of this is illustrated in Fig. 4.2.

The second type diverts water from streams with higher flow velocity to small side valleys, shaded by surrounding mountains. This design allows to integrate higher slope positions for additional ice formation. It consists of a series of partially cemented stone walls across the stream bed. Their dimensions are adjusted based on the valley topography. The water for the ice terrace is obtained through a long diversion channel.

The following construction guidelines are applied depending on the terrain of the construction site (Norphel and Tashi, 2015):

- If the section of the stream is very wide with a mild slope, then stone walls are constructed in a series parallel to each other. The number and dimension of

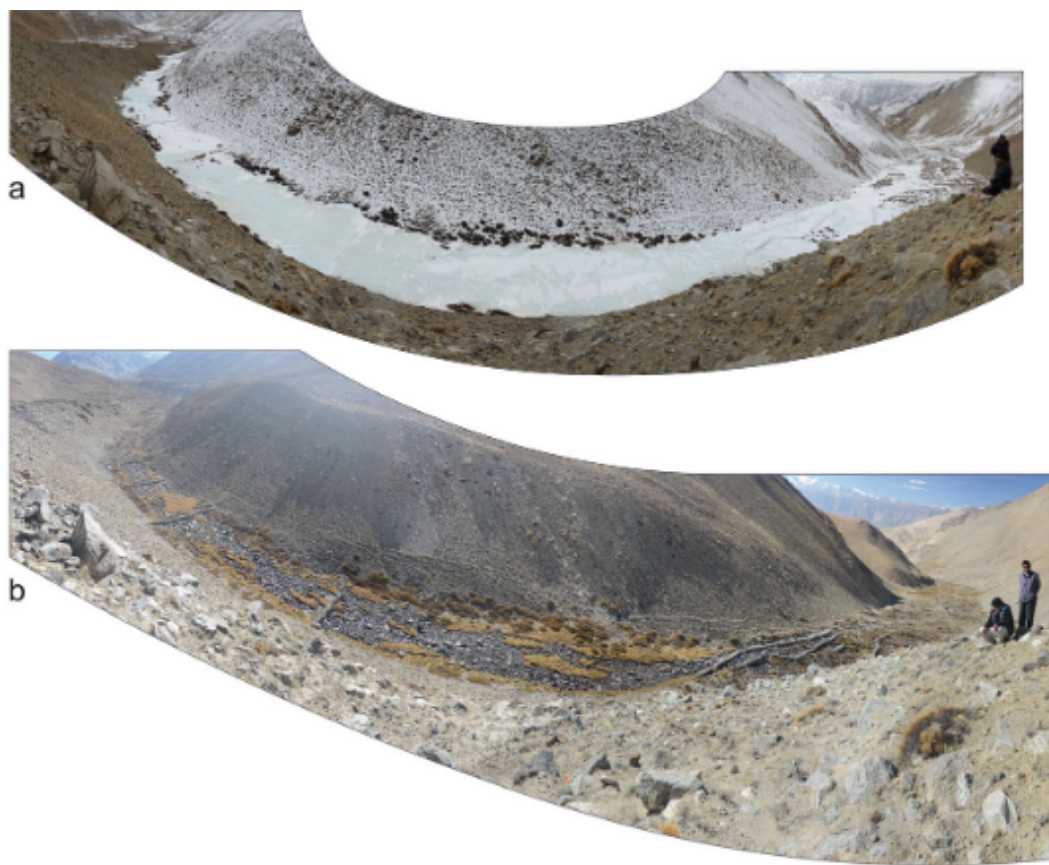


Fig. 4.2.: Ice terrace of Phuktse, viewpoint 4430 m. (a) February 2014 (b) October 2014
Adapted from: M. Nüsser et al., 2019

ice-retaining walls depend on the flow of water available in the main stream during peak winter.

- If the section of the stream is narrow with a steep gradient then it needs to be diverted to a shady area by constructing a gravitational channel with sufficient slope. When it reaches the ice terrace site the inclination should be gradually reduced, allowing the water to flow through small outlets thus accelerating freezing. Stone walls need to be constructed parallel to the channel in series, according to the natural slope of the terrain. The steeper the terrain, the smaller the distance and slope between the bunds.

Water storage and cost

The volume variations of ice terraces within Ladakh range from 510 m^3 to $81,040\text{ m}^3$ highlighting the importance of local topography and microclimate in their formation

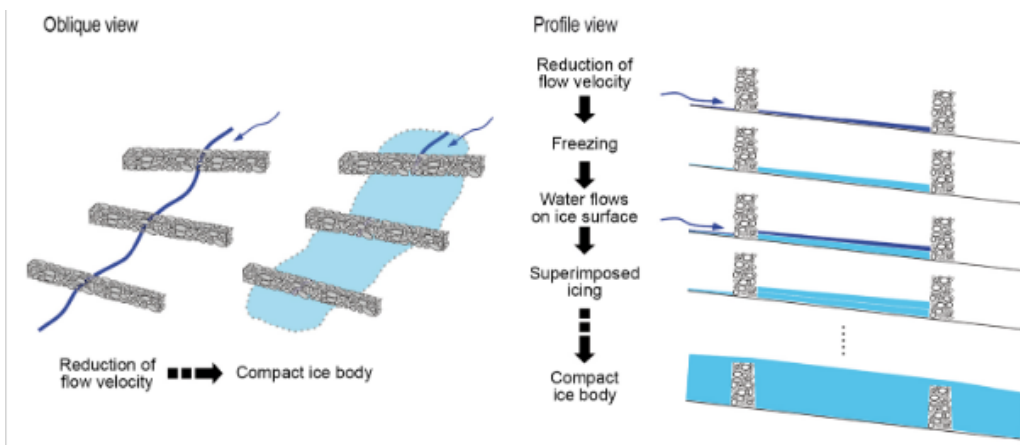


Fig. 4.3.: The process of ice accumulation for ice terraces. Adapted from M. Nüsser et al. (2019)

(M. Nüsser et al., 2019; Norphel and Tashi, 2015). The cost of construction depends on the size and number of stone walls required. The estimated material cost of ice terraces vary between 4600 to 15,330 USD (M. Nüsser et al., 2019). The building of ice terraces also relies on the participation of village communities for construction and maintenance.

4.1.2 Ice stupas



Fig. 4.4.: Ice stupa of Phyang village on March 2015.

Ice stupas, invented by Sonam Wangchuk in 2013, provide a much easier way to achieve water storage compared to ice terraces (S. Wangchuk, 2014). Ice stupas can be placed much closer to the plantations since they absorb less solar radiation per unit of volume compared to ice terraces due to their conical shape. However, the typical volume range of ice stupas is also much smaller than that of ice terraces (M. Nüsser et al., 2019). Over the past decade, several ice stupas have been built to supplement irrigation water supply of mountain villages in India (Sonam Wangchuk, 2020; Palmer, 2022; Aggarwal et al., 2021), Kyrgyzstan (BBC News, 2020), Nepal and Chile (Reuters, 2021).

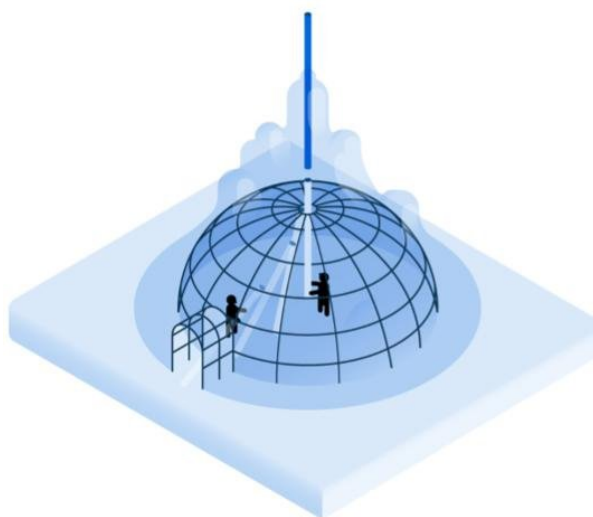


Fig. 4.5.: The construction process of ice stupas. Diagrams by: Francesco Muzzi

A typical ice stupa simply requires a fountain nozzle mounted on a supply pipeline (Fig. 4.4). The water source is usually a glacial stream. Due to the altitude difference between the pipeline input and fountain output, water ejects from the fountain nozzle as droplets which freeze under subzero winter conditions. The fountain is manually activated during winter nights. The fountain nozzle is raised through the addition of metal pipes when significant ice accumulates below (Fig. 4.5). Typically, a dome of branches is constructed around the metal pipes so that pipe extensions can be installed from within this dome. Threads, tree branches and fishing nets are used to guide and accelerate the ice formation.



Fig. 4.6.: Irrigation channel of the ice stupa at Phyang village. (P.C. Lobzang Dadul)

Water storage and cost

The cost of construction primarily depends on the material, size and length of the pipeline required. The fountain nozzle's cost is negligible in comparison. Typical pipeline configuration in Ladakh consists of a high density polyethylene pipeline of 63 mm diameter. The estimated cost of such a pipeline system is around 6,875 USD per km of pipeline length.

Figure 4.7 shows the temporal variation of daily meltwater quantities obtained from 3 different AIRs built in Ladakh during their melting periods (mid-April to mid-June). IN17 and IN18 AIRs were constructed in Phyang village and their meltwater quantities were measured manually (Fig. 4.6). These measurements were performed by recording the water level of a icestupa meltwater collection tank (Simant Verma, 2018). IN21 was constructed in Gangles village and its meltwater quantities were modelled. The differences between the AIRs reflect the corresponding interannual variability in the weather conditions. The median daily AIR meltwater quantities measured were higher than 11 thousand litres.

4.2 The need for water supply management

A common issue of AIR construction systems is water supply management, namely answering the questions "when to water?", "how much?", and "for how long?". Starting water supply too early, spraying too much water, or running water supply for too long might lead to overwatering; at the very least, this practice wastes water. Similarly, starting the water supply too late, supplying too little water, or not running the water supply long enough might lead to underwatering and can cause reduced ice volume. The management of water supply differs based on the type of the AIR

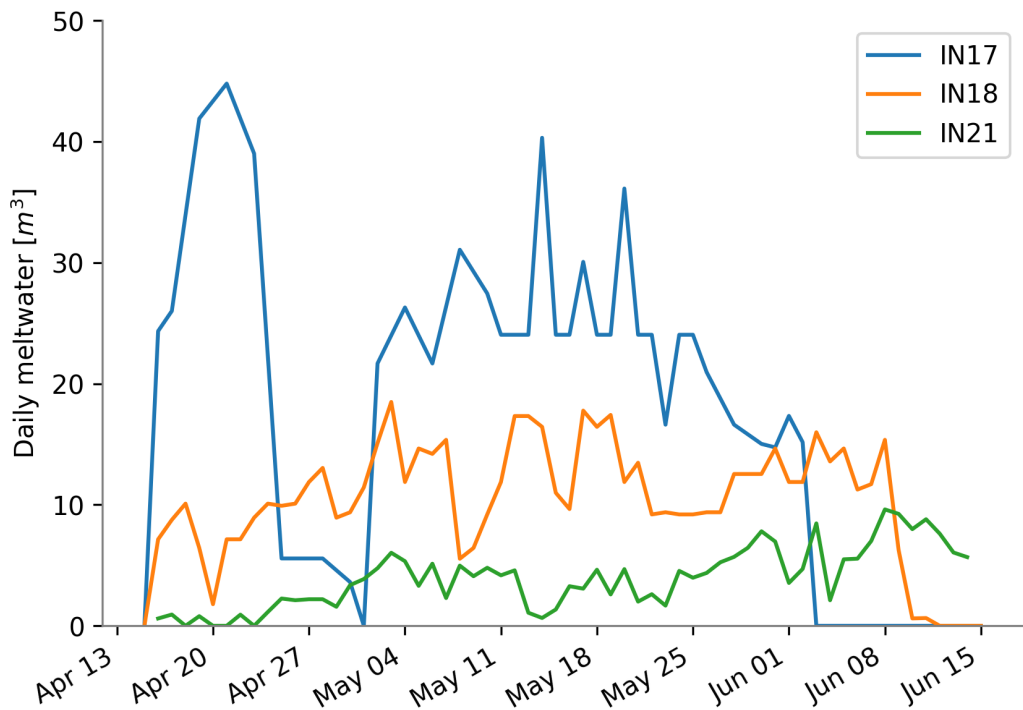


Fig. 4.7.: Daily meltwater measurements for the IN17 and IN18 AIRs along with the corresponding model estimations for the IN21 AIR.

used. In the following analysis, we restrict ourselves to the ice stupa form of AIRs where water supply management can also be referred to as fountain scheduling.

Paper I has shown that traditional ice stupa construction systems suffer from overwatering. For example, in Indian AIRs, the fountain discharge rate could theoretically be halved since it is always twice as high as the modelled freezing rate. However, in practice, the reduction of discharge rate could increase maintenance costs due to higher risk of freezing events in the fountain pipeline.

An optimum construction strategy, therefore, should first prevent the occurrence of freezing events in the fountain pipeline. These events can be prevented by setting a minimum threshold for the recommended discharge rate. The discharge scheduler software developed in the previous chapter satisfies these requirements.

Adjusting the fountain discharge rate manually is not practical due to two reasons: first, this would involve constant adjustments of discharge rates in response to the significant diurnal and seasonal variations of the freezing rates; second, frequent pipeline water drainage would be required to avoid water losses. Therefore, operation of scheduled fountains via automation systems is preferred to reduce long-term

maintenance costs. The hardware used to implement such an automation system is described in paper II.

This section aims to compare the water-use efficiency, maximum ice volume and maintenance effort between traditional and automated construction strategies. First, two AIRs were built in the same location but with and without automated fountain scheduling strategies; both were measured and compared (Fig. 4.8). The associated datasets and the methods used to analyze them are described in paper II. In a second step, differences in construction strategies between the Indian and Swiss AIRs studied in previous winters were quantified using model simulations. Later we discuss how these construction strategies can help scale the ice volumes and survival duration of AIRs.



Fig. 4.8.: Unscheduled and scheduled fountains used for construction of traditional and automated AIRs at Guttannen. Picture credits: Daniel Bürki

4.2.1 Automated fountain scheduling system

Recommended discharge rates can only be produced if more information about the AIR surface properties and weather conditions are available. Particularly, resolving the uncertainty in the expected freezing rate requires quantification of the following three model variables: slope, albedo and cloudiness. But these properties cannot be

predicted beforehand. Therefore, we instead associate the upper and lower bound of each variable to a different model depending on whether they increase the freezing rate or not. Higher slope and albedo values decrease the shortwave radiation impact. Higher cloudiness values increase both the shortwave and the longwave radiation impact. The model overestimating the freezing rate will be referred to as Ice Volume Optimised Model (IVOM) and the model underestimating the freezing rate will be referred to as Water-use Efficiency Optimised Model (WEOM), respectively. Accordingly, the values assigned for all the three variables in the respective model is shown in Table 4.1.

The fountain scheduling software implements two types of fountain scheduling strategies depending on which model type is suitable. WEOM model type is used if the location has limited water availability since it is expected to produce better water-use efficiency. IVOM model type is used if the location had limited duration of favourable weather windows since it is expected to produce higher ice volumes. These two kinds of scheduled fountains will be referred to as water-sensitive fountain and weather-sensitive fountain henceforth.

Tab. 4.1.: Assumptions for the parametrisation introduced to simplify the ice volume optimised model (IVOM) and water-use efficiency optimised model (WEOM). $\alpha_{snow/ice}$ represents albedo of snow or ice respectively.

Estimation of	Symbol	IVOM	WEOM
Slope	s_{cone}	1	0
Albedo	α	α_{snow}	α_{ice}
Cloudiness	cld	0	1

We apply the assumptions described in Table 4.1 on the one-dimensional description of energy fluxes through Eqn. 3.7. The derivation of the individual energy and mass balance terms for the IVOM and WEOM model versions are discussed in the Appendix A.3.

Equation 3.7 is implemented in the automation software. The user interface of the software enables input of the spray radius, altitude, latitude and longitude of the construction location. The automation hardware consists of an AWS, flowmeter, control valve, drain valves, air valves, fountain, pipeline and a logger. The logger feeds the AWS data to the automation software and informs the recommended discharge rate to the flowmeter. The flowmeter adjusts the control valve to match the recommendation. When a termination criteria is met, the drain and air valves allow the removal of water from the pipeline and the entry of air in the pipeline respectively.

The recommended discharge rate is equal to the mass change rate. However, certain termination criteria listed below override the discharge rate recommendation and drain the pipeline to prevent water loss or fountain freezing events:

- High water loss is assumed if wind speed is greater than the user-defined critical wind speed.
- High risk of fountain freezing event is assumed if mass change rate is lower than the user-defined minimum fountain discharge rate.
- Freezing events in the fountain pipeline are assumed if measured discharge rate is zero for at least 20 seconds.
- Pipeline leakage is assumed if measured discharge rate is greater than the user-defined maximum fountain discharge rate.

4.2.2 Comparison of traditional and automated construction strategies

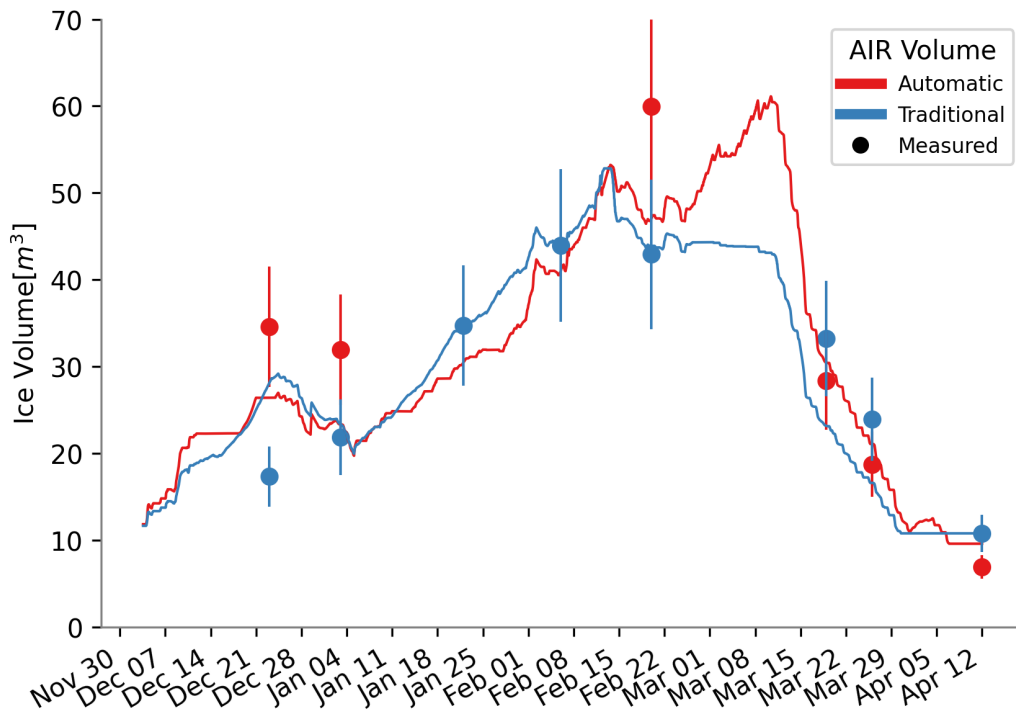


Fig. 4.9.: Volume validation of the scheduled and unscheduled fountain construction strategies.

Fountain scheduling reduced the fountain discharge input and fountain wastewater output by an order of magnitude. However, this does not result in an appreciable difference in the volume evolution of the automated or traditional AIR, as shown in Fig. 4.9. This is due to two counteracting surface processes during fountain spray: process A consists in the dampening of albedo to ice albedo and process B consists in the absorption of heat energy from the fountain water droplets. The temporal variation of the magnitude of these processes is shown in Fig. 4.10.

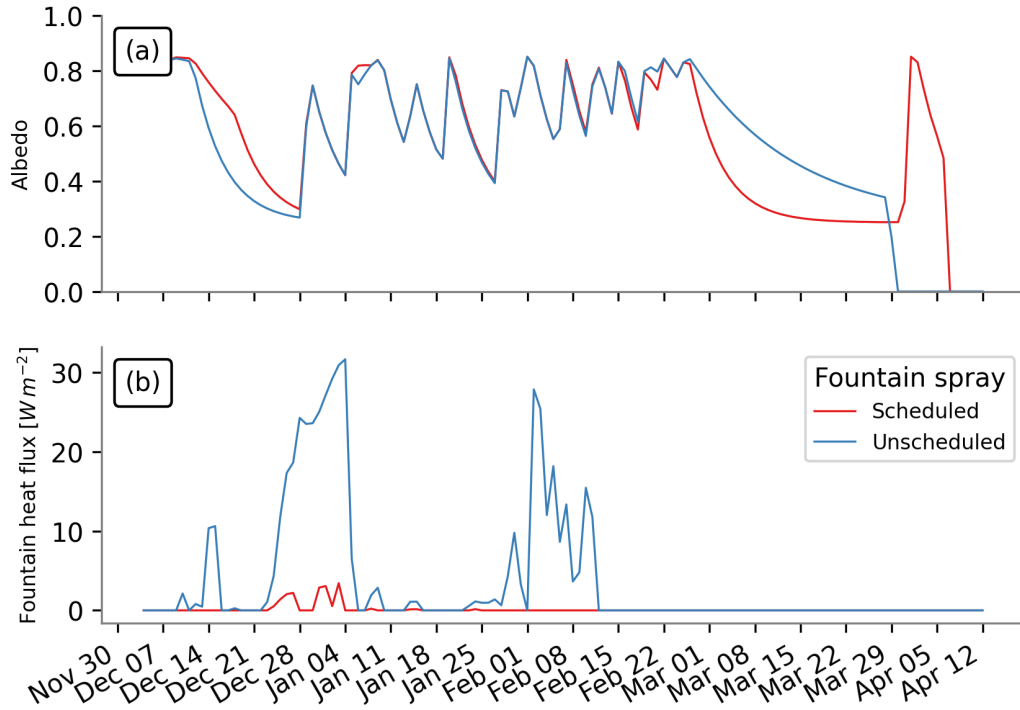


Fig. 4.10.: (a) Surface albedo and (b) fountain discharge heat flux showed significant variations between the two AIRS due to the differences in their discharge rates.

The difference in water-use efficiency and maximum ice volume between unscheduled and scheduled fountains in the Indian and Swiss locations across two winters is shown in Fig. 4.11a. Four experimental values (highlighted in circles) and five simulated values (highlighted in squares) are shown together. The experimental values were taken from the IN21 and CH21 AIRs studied in paper I and the CH22 AIR investigated in paper II.

The water-use efficiency of all the unscheduled fountains is below 20 %. In general, water-use efficiency exhibits a threefold increase when the weather- or water-sensitive fountains are used in both locations.

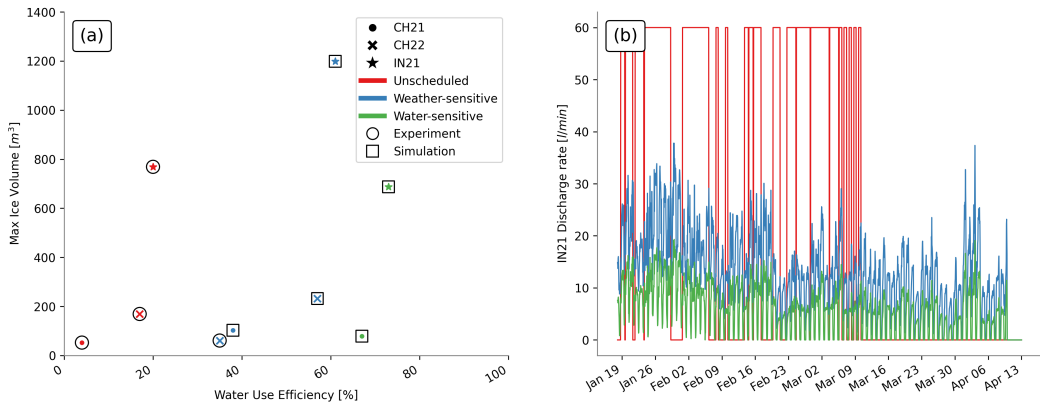


Fig. 4.11.: (a) The maximum volume and water-use efficiency estimated for AIRs constructed in different locations (represented by symbols) with different fountain scheduling strategies (represented by colours). Experimental values are highlighted in circles and simulated values are highlighted in squares. (b) Comparison of the unscheduled and scheduled fountain discharge rates at the IN21 location.

For the Indian location, the three different kinds of fountains yielded significantly different results owing to discharge duration and max discharge rate (Fig. 4.11b). The unscheduled fountain showed a maximum discharge rate more than twice that of the scheduled fountains, resulting in higher water loss; freezing events in its pipeline caused frequent interruptions in the unscheduled discharge rate (Fig. 4.11b). In contrast, the mean freezing rates of the other two fountains during these events were above their median values. This is because very cold temperatures freeze the water inside rather than outside the fountain system, instigating such freezing events in the fountain pipeline. Therefore, the discharge duration of the unscheduled fountain was much lower, resulting in lower ice volume. The water-sensitive fountain underestimated the freezing rate during the construction period and therefore produced much lower ice volume compared with the weather-sensitive fountain.

For the Swiss locations, scheduled fountains yielded better water-use efficiency but did not significantly alter the maximum volume obtained.

Habitat of ice reservoirs

“ Ice stupas offer a solution to the shortage of water all our mountain regions are facing.

— Pema Gyamtsho
(Director General, International Center for Integrated Mountain Development)

AIRs cannot be built anywhere. They require favourable weather conditions, sufficient water supply, and specific topography to amass a seasonal stock of ice. However, these three requirements exhibit drastic spatio-temporal variations. Therefore, high-resolution datasets are necessary to judge any location's AIR suitability.

In this chapter, we base our analysis on the ice stupas built in Swiss and the Indian regions where such datasets are available. We examine their observed volume variations across different spatial and temporal scales. Later, we discuss some useful metrics to qualitatively assess the suitability of new construction locations in a regional and local scale.

5.1 Observed ice volume variability

5.1.1 Interregional scale

AIRs built in the Himalayas, Andes and the Alps show drastic ice volume variations (Fig. 5.1). Comparison of ice stupa volume evolution show that the Indian structures grew four times larger than the Swiss ones (Fig. 3.1). The corresponding freezing rate of the Indian ice stupa was more than ten times higher than the Swiss one. Sublimation was identified as the driving process of this difference (paper I). These results indicate that the colder, drier and less cloudy weather characteristics of the Ladakh region made it more suitable to build AIRs compared to the Guttannen region.

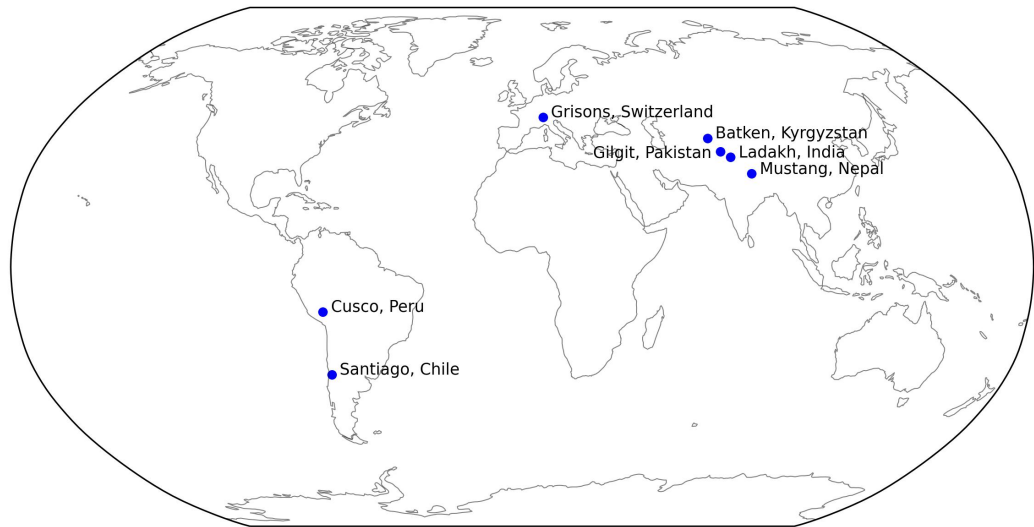


Fig. 5.1.: Regions where AIRs have been built.

5.1.2 Intraregional scale

We measured ice volumes in more than 14 villages in Ladakh (Fig. 5.2). Their volume variation reveals a correlation with the altitude of the construction location (Fig. 5.3). This correlation indicates that elevation gain of 100 m causes a corresponding ice volume gain of 1 million litres. However, some locations with lower altitude exhibit higher volumes compared to those with a higher altitude. This is due to topographic effects of shadow valleys that reduce the sunshine hours of the location (Maria Gruber, 2022).

Some ice stupas built in villages above 4200 m a.s.l. (Shara and Igoo) have also been observed to last beyond a summer melt season (Fig. 5.4). However, such favourable weather conditions remain to be discovered in the Swiss mountains. A possible way to study this question is to decrease the air temperature uniformly (temperature change ΔT). This will imply a stronger negative sensible heat flux in summer, thus accelerating ice stupa growth and slowing down its decay. Such simulations were produced in paper III for an ice stupa grown in the Diavolezza site at an altitude of 2080 m a.s.l. . We found a break-even point for $\Delta T = -2^{\circ}\text{C}$ (Fig. 5.5). For larger negative values of ΔT the ice stupa does not disappear in summer and keeps growing from year to year. For $\Delta T = -3^{\circ}\text{C}$, the maximum volume in the fifth year is about 4 times that in the first year (Fig. 5.5). Therefore, we hypothesize that ice stupas can last beyond a year even in Switzerland if built in locations with an elevation above 2388 m (based on a standard atmospheric lapse rate of 0.0065 $^{\circ}\text{C m}^{-1}$).

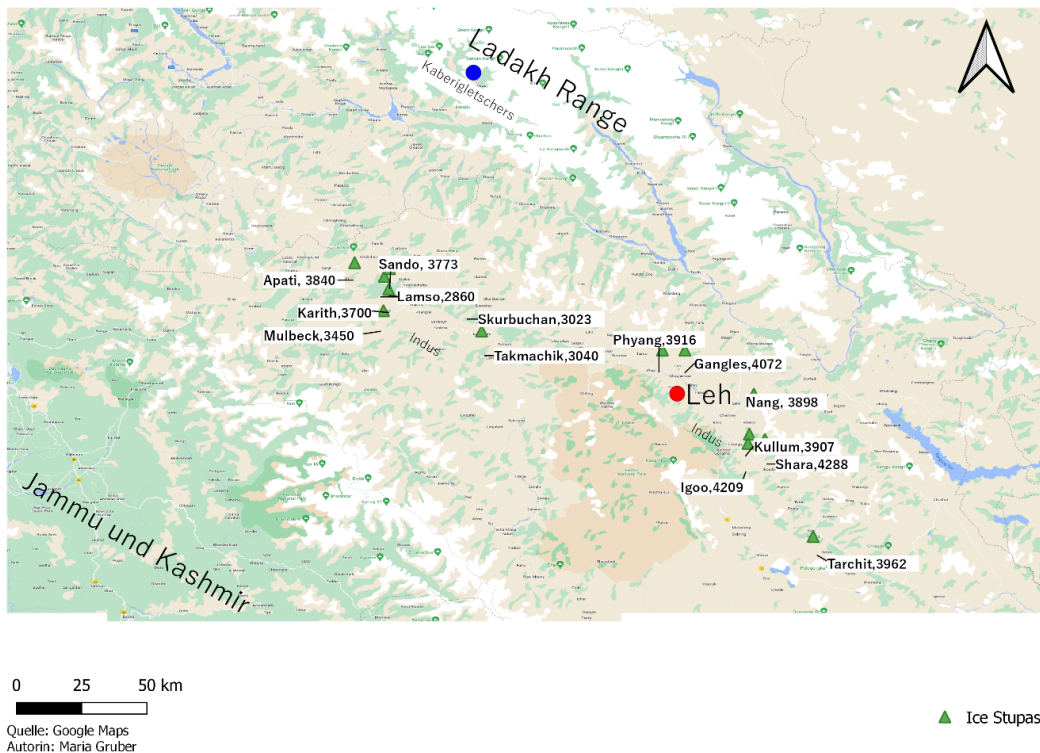


Fig. 5.2.: Some villages of Ladakh where AIRs have been built. Adapted from Maria Gruber (2022).

5.1.3 Interannual scale

AIRs built in Switzerland across three winters (CH20, CH21 and CH22) show a decreasing trend in their ice volume changes for the month of January. Contrary to expectations, this decreasing trend was not caused by increasing temperatures but rather by decreasing wind speeds (Fig. 5.6). A process-based analysis revealed that wind driven redistribution could explain these differences (paper II). The influence of this process on the fountain spray radius managed to generate AIRs six times bigger in spite of temperatures being 3°C warmer (Fig. 5.6 (b)).

5.2 Metrics to judge site suitability

Accordingly, we propose two sets of guidelines to identify future construction sites at a regional and a local scale. These decisions are guided by both the different case studies presented in this thesis and my field experiences in Ladakh over the past six winters.

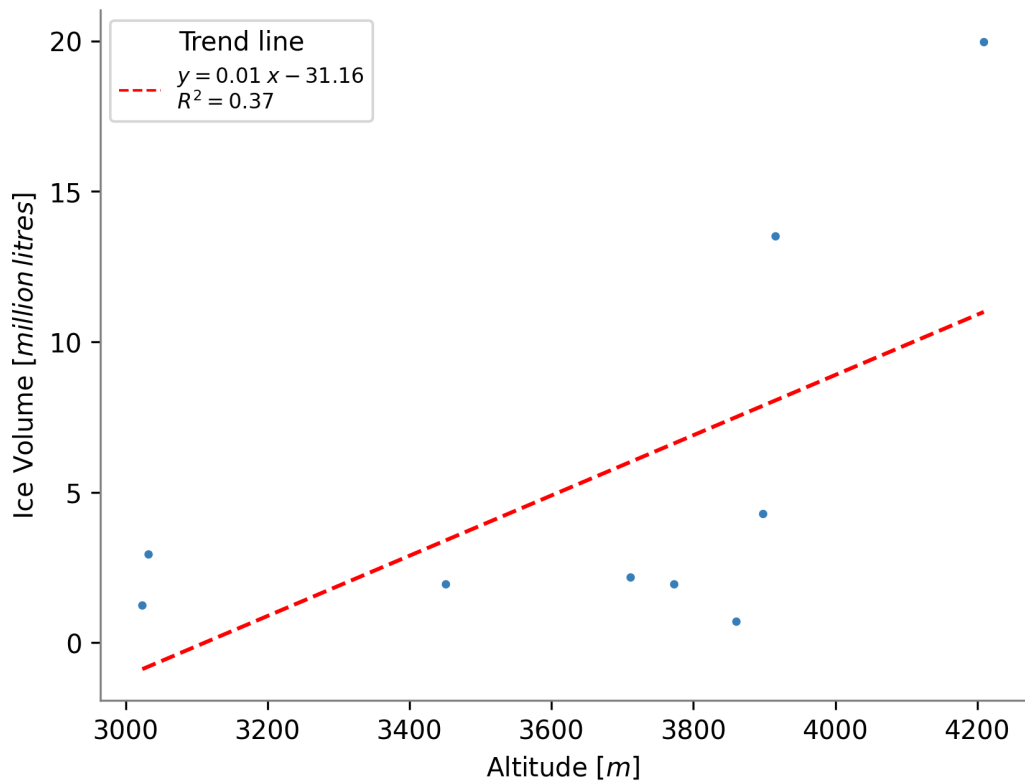


Fig. 5.3.: Relationship of measured ice volume with altitude of AIRs built during winter of 2019-20 across different villages in Ladakh. Adapted from Maria Gruber (2022).

5.2.1 Regional scale

1. Minimum median monthly temperature less than $0^\circ C$.
2. Water supply with median discharge rate more than $2 l/min$.
3. Terrain slope between water source and site greater than 20 m every km.

5.2.2 Local scale

Given a valley or a region satisfying the above requirements, further selection of sites around the particular water supply can be performed using the criterions below:

1. Water source temperature is higher.
2. Daylight hours are lower due to shadows.
3. Altitude is higher.



Fig. 5.4.: Icestupa at Shara, Ladakh, built by local farmers in the winter of 2019-20, survived a full summer melt season and released around 8 million litres of water.

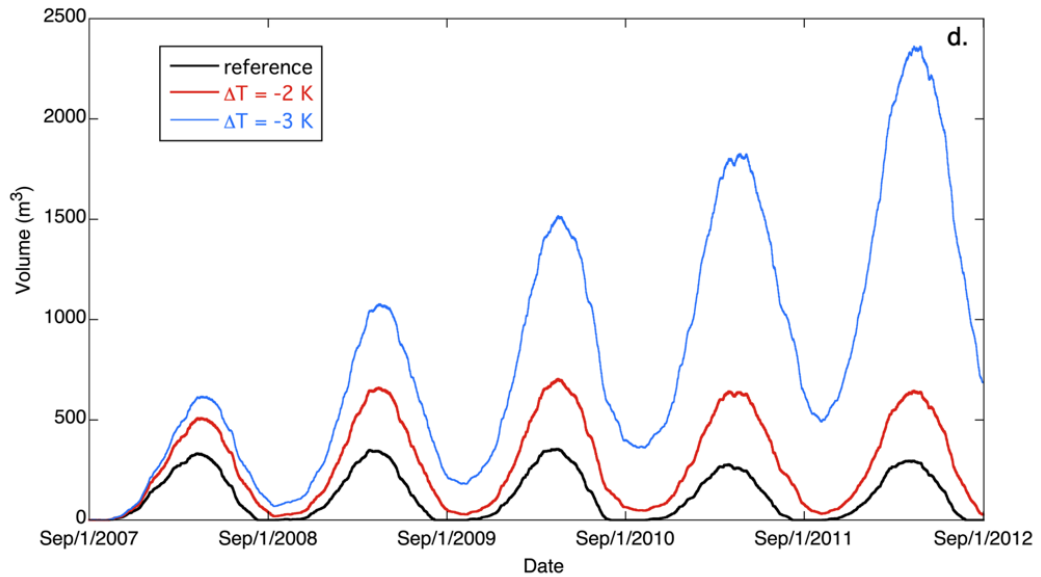


Fig. 5.5.: The effect of a negative temperature perturbation. For $\Delta T = -3^{\circ}\text{C}$ the icestupa does not disappear anymore but is growing from year to year.

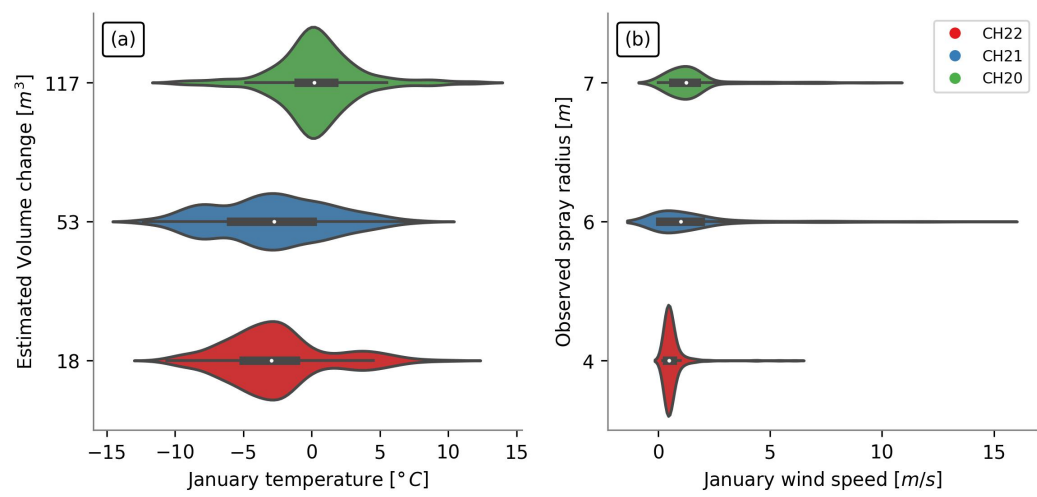


Fig. 5.6.: (a) Estimated volume change and temperature and (b) Observed spray radius and wind speed during January for AIRs built across three winters.

Heritage of ice reservoirs

“ Before the artificial glacier, we struggled to get any barley. But now we can grow many crops, even potatoes, which need to be planted earlier in the spring, but sell for much more money.

— Tashi Tundup

(A 76 year old farmer in Ladakh)

This chapter provides conclusions based on research findings from data collected on AIRs in Switzerland and India, as well as discussion and recommendations for future research. This chapter will review the purpose of the study, research questions, literature review, and findings of the study. It will then present conclusions, discussion of the conclusions, and recommendations for practice and for further research.

6.1 Summary

Irrigation networks in arid mountain regions are completely dependant on the timely availability of meltwater from glaciers, snow and permafrost. With the accelerated decline of glaciers, these irrigation networks can no longer deliver adequate water to sustain agricultural output and take advantage of the complete growing season. As a consequence, some mountain villages have either been abandoned or lie on the brink of desertification (Grossman, 2015).

In the past few decades, AIR technologies have provided much needed relief to these water-stressed communities. These strategies involve augmenting their glacial ice reservoirs with man-made ones that provide supplementary irrigation during the spring. In the context of the observed present and predicted global glacier shrinkage, the development of such water storage technologies is crucial to ensure continued sustenance of cryosphere-fed irrigation networks.

AIR observations and investigations date back to the mid-2000s (Tveiten, 2007). The vast majority have been published in the 2010s, mostly using qualitative methods.



Fig. 6.1.: Compilation of AIRs built in different villages of Ladakh.

However, quantifications of their storage capacity differ widely amongst these publications (Bagla, 1998; Norphel and Tashi, 2015; M. Nüsser et al., 2019). Because small-scale processes, complex feedbacks and non-linearities govern their evolution, modelling the volume evolution of ice stupas is only feasible if backed up with comprehensive input, calibration and validation datasets.

In response, we conducted measurement campaigns using drones, flowmeters and weather stations on almost a dozen AIRs across two locations (India and Switzerland), over four winters (2019, 2020, 2021 and 2022) and using two different construction methods (traditional and automated). Each dataset contained information on the meteorological conditions, fountain characteristics and AIR volume evolution.

The primary objective of this thesis was to improve our understanding of AIRs' response to changes in their construction location. The secondary objective was to propose automated construction strategies that reduce water losses and maintenance efforts.

6.2 Conclusions

In paper I, an AIR model was designed to resolve surface processes and used to compare their volume evolution in Indian Himalayas and the Swiss Alps. In paper II, the evolution of AIRs using different fountain scheduling strategies were compared. In paper III, the possibility of sustaining artificial ice reservoirs perpetually was explored. The results of these papers can be summarised as follows:



Fig. 6.2.: One of the deserted villages in Ladakh where AIR meltwater supported a harvest of 1300 kgs of potatoes in October 2021. (P.C. Icestupa Project)

1. Volumes of ice stupas located in different regions may differ by an order of magnitude. The differences could be attributed to the accelerated sublimation process in colder and drier regions.
2. Water losses of ice stupas may be upto 80 % due to excessive water input. However, water supply management through fountain scheduling strategies can produce ice stupas of similar volumes while reducing up to one-tenth of their water supply.
3. Traditional construction systems demand significant maintenance efforts since they are prone to freezing events in the fountain pipeline. However, automated construction systems can prevent these events to make the construction process maintenance-free.
4. There exist locations with favourable weather conditions that can sustain artificial ice reservoirs perpetually.

6.3 Discussion

6.3.1 The state of ice stupa technology

The thesis shows one strategy that can improve the water-use efficiency of AIRs. We chose this strategy because it enables the use of the AIR model in a simple and effective manner. But all these construction strategies are limited by the tools they use, namely the fountain and the pipeline. The fountain nozzle design is crucial for increasing the ice volume obtained. However, no methodology currently exists to rank the several fountain nozzles used for construction. An ideal pipeline configuration could make this technology cheaper and maintenance free. However, optimization of the pipeline material and diameters is yet to be performed—despite the time lost on pipeline freezing events and the potential cost reduction with cheaper pipeline materials and sizes. Therefore, we strongly encourage the engineering community to get involved and push the limits of the cost-effectiveness, size, and survival duration of artificial ice reservoirs.

6.3.2 Adaptation potential of glacierized catchments with AIRs

Vanishing glaciers, natural hazards (like inundations, mudflows, and landslides), decreasing river discharge, drying springs, next to shifts in precipitation patterns are apparent climate change impacts which affect glacierized catchments.

In the Peruvian Andes, both water scarcity (low-flow water risk) and glacial lake outburst floods (high flow water risks) could have important impacts on local population, infrastructure and economic activities (Motschmann, Huggel, et al., 2020). For example, the estimated loss in wheat output due to reduced glacial runoff would be to the tune of 18 million USD in the low emission scenario of Quillcay catchment of Peru (Motschmann, Teutsch, et al., 2022). Similarly, in the Stok catchment of Ladakh, glacial ice reserves have shrunk by more than 18 % in the past 16 years, leading to a decline in crop productivity (Soheb et al., 2022).

We believe AIRs can already buffer against low flow water risks in certain catchments. For example, ice terraces in nearby valleys have been measured with areas up to 19 % of the Stok glacier (0.8 km^2). With further technology development, AIRs can also be used to mitigate high flow water risks. The glacial lakes of the Andes and Himalayas can be siphoned to form AIRs in scale that last perpetually. Such AIRs

can compound over the years to become another source of perennial water supply for the respective catchments.

6.4 Future research direction

Any future research can take advantage of the weather, fountain and drone datasets acquired in the two field sites described in this thesis. Both AIR and COSISTUPA models are also freely provided through git repositories for non-profit purposes (<https://github.com/gayashiva>, last access: August 1, 2022).

Insights from this research could contribute to efforts to better estimate the future potential of AIRs for climate change adaptation and mitigation under multiple plausible future climatic, demographic, economic, and land use scenarios.

6.4.1 Model development

The COSISTUPA model developed in section 3.4.6 should be used for future estimations for AIR volume. This model needs to be extended so that it can account for future climate variability and produce accurate meltwater predictions. Modelling the future is fundamentally different from simulating the past: In the past the model serves as a tool for interpreting and best exploiting field measurements - and can be directly constrained by these. Models for the future must understand climate variability to be able to yield realistic projections. Almost all methodological steps in the modelling of future AIR runoff are subject to possible enhancements, always bearing in mind that we will only know whether the effort led to an enhanced or even a worsened performance, when we're old...

6.4.2 Quantification and development of ice terraces

Although this thesis focuses on ice stupas, their ice volumes pale in comparison with ice terraces (M. Nüsser et al., 2019). This is because ice stupas are limited by their fountain's spray radius. However, ice terraces have no such limitations. Their thickness is only limited by the water supply rate or weather conditions and they can occupy any construction area provided. But despite this, ice stupas are the preferred method of ice harvesting due to their longer survival duration and reduced construction effort.

With a suitable redesign of the automation hardware, automated construction strategies can also be applied on ice terraces. Such a construction strategy can potentially compound their size every consecutive winter with minimal maintenance requirements. Therefore, future research direction should aim to answer the following questions:

- How can ice terrace construction systems be engineered to reduce their water losses and maintenance efforts?

The methodology developed in this thesis should also apply for such an analysis.

6.4.3 Quantifying sustenance of glacierized catchments with AIRs

Glaciers provide an important buffer for highly seasonal precipitation regimes (Kaser et al., 2010). Under the currently available climate change projections it is expected that glacial mass loss will continue in future decades, and that several smaller glaciers will continue to disappear completely (Rabatel et al., 2013).

In arid and semiarid regions, in particular, it is estimated that between 50 % and 90 % of freshwater resources originate from mountain catchments (Messerli et al., 2004). During drought conditions in the tropical mountain regions, glacial meltwater is used by upto 3.92 million domestic users and to irrigate 2096 km^2 of land (Buytaert et al., 2017).

These trends stress the importance of increased water storage capacity for glacierized catchments as a pathway for climate adaptation. Because of the challenges and cost related to traditional storage efforts, AIRs can be a better tool to adapt against reduced glacial runoff. In order to quantify their adaptation potential, it is necessary to understand the changing dynamics of AIR melting, but also map how their meltwater contributes to current and future water use. While the spatiotemporal dynamics of AIR melt are increasingly well understood and documented in this thesis, major uncertainty remains on how their meltwater contribution propagates through the hydrological system and compares against the total discharge of mountain catchments.

Future research needs to determine which catchments can benefit most from the supplementary water supply provided by these ice harvesting technologies and flag off the urgent climate action required to increase their water security.

Peer-reviewed papers

7.1 Paper I

Influence of Meteorological Conditions on Artificial Ice Reservoir (Icestupa) Evolution

Balasubramanian, S., Hoelzle, M., Lehning, M., Bolibar, J., Wangchuk, S., Oerlemans, J., and Keller, F.

Frontiers in Earth Science 9 (February 23, 2022): 771342. doi:10.3389/feart.2021.771342.



Influence of Meteorological Conditions on Artificial Ice Reservoir (Icestupa) Evolution

Suryanarayanan Balasubramanian^{1,2*}, Martin Hoelzle¹, Michael Lehning³, Jordi Bolíbar⁴, Sonam Wangchuk², Johannes Oerlemans⁴ and Felix Keller^{5,6}

¹Department of Geosciences, University of Fribourg, Fribourg, Switzerland, ²Himalayan Institute of Alternatives Ladakh, Leh, India, ³WSL Institute for Snow and Avalanche Research, Davos, Switzerland, ⁴Institute for Marine and Atmospheric Research, Utrecht University, Utrecht, Netherlands, ⁵Academia Engiadina, Samedan, Switzerland, ⁶ETH, Zürich, Switzerland

Since 2014, mountain communities in Ladakh, India have been constructing dozens of Artificial Ice Reservoirs (AIRs) by spraying water through fountain systems every winter. The meltwater from these structures is crucial to meet irrigation water demands during spring. However, there is a large variability associated with this water supply due to the local weather influences at the chosen location. This study compared the ice volume evolution of an AIR built in Ladakh, India with two others built in Guttannen, Switzerland using a surface energy balance model. Model input consisted of meteorological data in conjunction with fountain discharge rate (mass input of an AIR). Model calibration and validation were completed using ice volume and surface area measurements taken from several drone surveys. The model was successful in estimating the observed ice volume evolution with a root mean square error within 18% of the maximum ice volume for all the AIRs. The location in Ladakh had a maximum ice volume four times larger compared to the Guttannen site. However, the corresponding water losses for all the AIRs were more than three-quarters of the total fountain discharge due to high fountain wastewater. Drier and colder locations in relatively cloud-free regions are expected to produce long-lasting AIRs with higher maximum ice volumes. This is a promising result for dry mountain regions, where AIR technology could provide a relatively affordable and sustainable strategy to mitigate climate change induced water stress.

OPEN ACCESS

Edited by:

Thomas Vikhamar Schuler,
University of Oslo, Norway

Reviewed by:

Alan Rempel,
University of Oregon, United States
Lukas U. Arenson,
BGC Engineering, Canada

*Correspondence:

Suryanarayanan Balasubramanian
suryanarayanan.balasubramanian@
unifr.ch

Specialty section:

This article was submitted to
Cryospheric Sciences,
a section of the journal
Frontiers in Earth Science

Received: 06 September 2021

Accepted: 23 December 2021

Published: 23 February 2022

Citation:

Balasubramanian S, Hoelzle M, Lehning M, Bolíbar J, Wangchuk S, Oerlemans J and Keller F (2022) Influence of Meteorological Conditions on Artificial Ice Reservoir (Icestupa) Evolution. *Front. Earth Sci.* 9:771342.
doi: 10.3389/feart.2021.771342

1 INTRODUCTION

Seasonal snow cover and glaciers are expected to change their water storage capacity due to climate change with major consequences for downriver water supply (Immerzeel et al., 2019). The challenges brought about by these changes are especially important for dry mountain environments such as in Central Asia or the Andes, which directly rely on the seasonal meltwater for their farming and drinking needs (Unger-Shayesteh et al., 2013; Chen et al., 2016; Buytaert et al., 2017; Apel et al., 2018; Hoelzle et al., 2019).

Ladakh, sandwiched between the Himalayan ranges and the Karakoram in India, is one such region experiencing climate change induced water stress. Glaciers in the Ladakh region are vital for sustaining agricultural activities which form the basis for regional food security and socio-economic



FIGURE 1 | Icestupa in Ladakh, India on March 2017 was 24 m tall and contained around 3,700 m³ of water. Picture Credits: Lobzang Dadul.

development (Labbal, 2000; Schmidt and Nüsser, 2012). During a low precipitation year, glaciernelt and snowmelt are the only sources of water supply to the region (Thayyen and Gergan, 2010). Some villages in Ladakh have already been forced to relocate due to glacial retreat and the corresponding loss of their main fresh water resources (Grossman, 2015).

Around 26 villages in this region (Wangchuk, 2021) have been using artificial ice reservoirs (AIR) to adapt to these changes since they require very little infrastructure, skills and energy to be constructed in comparison to other water storage technologies (Nüsser et al., 2019b; Hock et al., 2019). An AIR is a human-made ice structure typically constructed during the cold winter months and designed to slowly release freshwater during the warm spring and summer months. The main purpose of AIRs is irrigation. Therefore, AIRs are designed to store water in the form of ice as long into the summer as possible. The energy required to construct an AIR is usually derived from the gravitational head of the source water body. Some are constructed horizontally by freezing water using a series of checkdams while others are built vertically by spraying water through fountain systems (Nüsser et al., 2019a). The latter are colloquially referred to as Icestupas and are the subject of this study.

A typical AIR (see **Figure 1**) simply requires a fountain nozzle mounted on a supply pipeline. The water source is usually a high altitude lake or glacial stream. Due to the altitude difference between the pipeline input and fountain output, water ejects from the fountain nozzle as droplets which freeze under subzero winter conditions. The fountain is manually activated during winter nights. The fountain nozzle is raised through the addition of metal pipes when significant ice accumulates below. Typically, a dome of branches is constructed around the metal pipes so that pipe extensions can be done from within this dome. Threads, tree branches and fishing nets are used to guide and accelerate the ice formation.

However, to date, no reliable estimates exist about the quantity of meltwater an AIR can provide (Nüsser et al., 2019a). Moreover, preliminary estimates of AIRs in Ladakh

indicate that they generate high water losses during their lifetimes (see **Supplementary Appendix 7.1**). During their accumulation period, AIRs can lose excessive fountain water and, during the ablation period, sublimation losses could also be significant. However, the relative contribution of these processes in the total water loss remains unknown.

In this paper, we develop a physically-based model of vertical AIRs (or Icestupas) that can estimate their freezing and melting rates. Mass and energy balance equations were used to estimate the quantity of ice, meltwater, sublimation and wastewater. Sensitivity and uncertainty analysis were performed to identify the most sensitive parameters and the variance they caused. For calibration, we chose two AIRs built across the winter of 2020/21 in India and Switzerland, and validated the model on a Swiss AIR built during winter 2019/20. Our model results provide a first step towards evaluating the potential of this decade old water storage technology worldwide (Wangchuk, 2014).

2 STUDY SITES AND DATA

The model requires three kinds of datasets containing weather, fountain and AIR volume measurements to accurately calibrate, estimate and validate the ice volume of AIRs. Through the winters of 2018/19, 2019/20 and 2020/21, such datasets were acquired for four AIRs in both Switzerland and India. Here, we present the results of three AIRs, which have a complete dataset. Two of them were constructed in the same Swiss location called Guttannen (referred to with the prefix CH) but during different winters, and the other was constructed at Gangles, India (referred to with the prefix IN). The 2020/21 AIR constructed on both these locations are shown in **Figure 2**.

The Guttannen site (46.66 °N, 8.29 °E) in the Bern region lies at 1047 m a.s.l.. In the winter (Oct-Apr), mean daily minimum and maximum air temperatures vary between -13 and 15 °C. Clear skies are rare, averaging around 7 days during winter. Daily winter precipitation can sometimes be as high as 100 mm. These values are based on 30 years of hourly weather model simulations (Meteoblue, 2021). The site was situated adjacent to a stream resulting in high humidity values across the study period as shown in **Figure 2**. AIR were constructed here by the Guttannen Bewegt Association during the winters of 2019–20 (CH20) and 2020–21 (CH21). Tree branches were laid covering the fountain pipe to initiate the ice formation process. The fountain height varied between 2 and 5 m during the construction period. The water was transferred from a spring water source and flowed via a flowmeter to the nozzle. In addition, a webcam guaranteed a continuous survey of the site during the construction of the AIR.

The Gangles site (34.22 °N, 77.61 °E) is located around 20 km north of Leh city in the Ladakh region, lying at 4025 m a.s.l.. The mean annual temperature is 5.6 °C, and the thermal range is characterized by high seasonal variation. During January, the coldest month, the mean temperature drops to -7.2 °C. During August, the warmest month, the mean temperature rises to

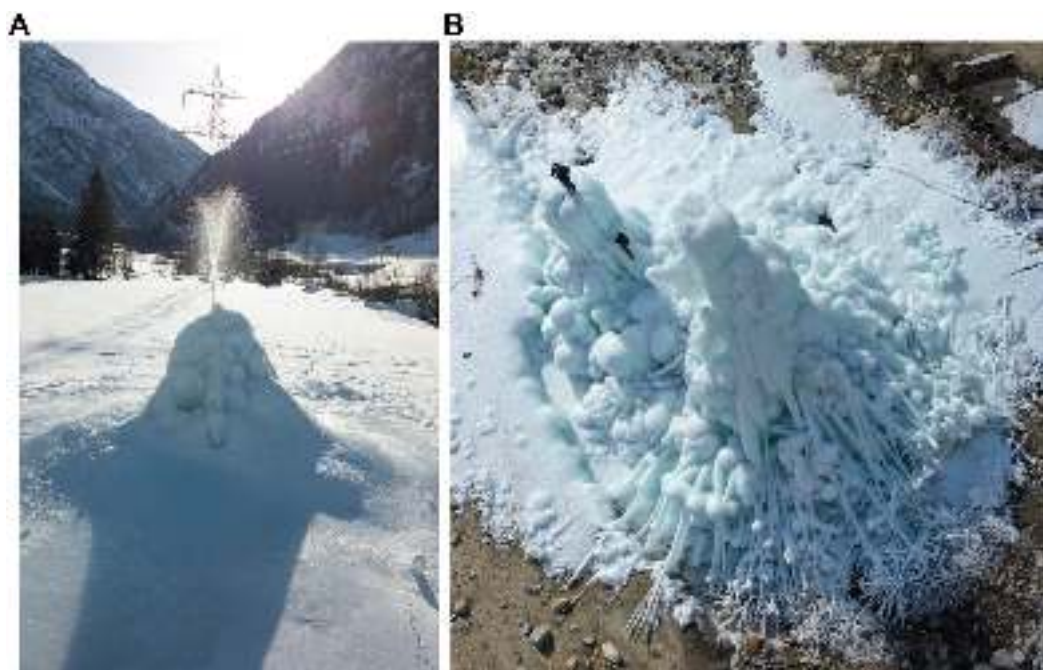


FIGURE 2 | The Swiss and Indian AIRs were 5 m and 13 m tall on January 9 and March 3, 2021 respectively. Picture credits: Daniel Bürki (**A**) and Thinles Norboo (**B**).

TABLE 1 | Summary of the weather and fountain observations. The expiry date refers to the date when all of the ice of the AIR completely disappeared and only the dome volume remains. The weather measurements are shown using their mean (μ) and standard deviation (σ) during the study period as $\mu \pm \sigma$.

	Name	Symbol	IN21	CH21	CH20	Units
Weather	Air temperature	T_a	0 ± 7	2 ± 6	2 ± 4	°C
	Relative humidity	RH	35 ± 20	79 ± 18	77 ± 17	%
	Wind speed	v_a	3 ± 1	2 ± 2	2 ± 2	m/s
	Direct Shortwave	SW_{direct}	246 ± 333	80 ± 156	80 ± 150	$W\ m^{-2}$
	Diffuse Shortwave	$SW_{diffuse}$	0 ± 0	58 ± 87	51 ± 74	$W\ m^{-2}$
	Incoming Longwave Radiation	LW_{in}	194 ± 31	239 ± 35	236 ± 34	$W\ m^{-2}$
	Hourly Precipitation	ppt	0 ± 0	139 ± 457	95 ± 404	mm
	Pressure	ρ_a	623 ± 3	794 ± 9	798 ± 7	hPa
	Start Date		Jan 18 2021	Nov 22 2020	Jan 3 2020	
	Expiry Date		June 20 2021	May 10 2021	April 6 2020	
Fountain	Discharge rate	d_F	60	7.5	7.5	l/min
	Runtime	t_F	829	2155	1553	hours
	Spray radius	r_F	10.2	6.9	7.7	m
	Water temperature	T_F	1.5	1.5	1.5	°C

17.5 °C (Nüsser et al., 2012). Because of the rain shadow effect of the Himalayan Range, the mean annual precipitation in Leh totals less than 100 mm, and there is high interannual variability. Whereas the average summer rainfall between July and September reaches 37.5 mm, the average winter precipitation between January and March amounts to 27.3 mm and falls almost entirely as snow. AIRs were constructed here as part of the Ice Stupa Competition by the Himalayan Institute of Alternatives, Ladakh (HIAL). The fountain height of the AIR varied between 5 and 9 m.

2.1 Meteorological Data

Air temperature, relative humidity, wind speed, pressure, longwave, shortwave direct and diffuse radiation are required to calculate the surface energy balance of an AIR (see Table 1). The study period starts when the fountain was first switched on and ends when the respective AIR melted completely. These two dates are denoted as start and expiry dates henceforth.

For the CH site, the primary weather data source was a meteoswiss AWS located 184 m away (Station ID: 0-756-0-GTT). In addition, we used ERA5 reanalysis dataset

TABLE 2 | Summary of the drone surveys.

	No.	Date	Volume (m ³)	Radius (m)	Surface Area (m ²)
IN21	1	Jan 18, 2021	103	9.1	411
	2	Feb 27, 2021	580	10.2	668
	3	Mar 3, 2021	626	10.3	694
	4	Mar 15, 2021	692	10	681
	5	Mar 26, 2021	582	10.2	671
	6	Apr 3, 2021	620	10.1	658
CH21	1	Nov 22, 2020	13	5.4	136
	2	Dec 2, 2020	26	5.7	118
	3	Dec 30, 2020	43	7.5	189
	4	Jan 9, 2021	82	6.5	150
	5	Mar 6, 2021	108	7.5	183
	6	Apr 2, 2021	83	6.5	150
	7	Apr 16, 2021	64	6.2	134
	8	Apr 24, 2021	37	4.7	80
CH20	1	Jan 3, 2020	24	6.7	170
	2	Jan 24, 2020	59	7.7	228

(Copernicus Climate Change Service (C3S), 2017) for filling data gaps and adding the shortwave and longwave radiation data that were not measured directly. The ERA5 reanalysis dataset is known to have a high correlation with sites in Switzerland (Scherrer, 2020). The Guttannen temperature dataset had a correlation greater than 0.8 with the ERA5 temperature for both winters. The ERA5 grid point chosen (46.64 °N, 8.25 °E) for the Swiss site was around 3.6 km away from the actual site. ERA5 variables (except incoming shortwave and longwave radiation) were fitted to the meteoswiss dataset via linear regressions. The zero wind speed values recorded by the meteoswiss AWS whenever snow accumulated on the ultrasonic wind sensor were replaced using the ERA5 dataset.

For the IN site, two different weather data sources were used to log all weather parameters required for the model. Temperature, humidity, wind speed and pressure data were logged with a weather station located 440 m away from the construction site. Shortwave radiation data were derived from another weather station located 15 km away. Unfortunately, precipitation was not logged. Since winter precipitation in Ladakh is less than 30 mm (Nüsser et al., 2012), we can safely assume negligible precipitation and mostly clear skies. As a consequence, the diffuse fraction of the global shortwave radiation was also assumed to be negligible. Temperature and humidity were measured with a rotronic sensor with an accuracy of ± 0.3 °C and ± 1% respectively. A young sensor measured the wind speed with an accuracy of ± 0.3 ms⁻¹ and a setra sensor measured the pressure with an accuracy of ± 0.01 hPa.

2.2 Fountain Observations

We define the fountain used through four attributes; namely, its spray radius, mean discharge rate, discharge runtime and water temperature as shown in **Table 1**. Continuous measurement of the discharge rate was unsuccessful in all sites due to data logger malfunctions of the associated flowmeter. Instead the discharge

duration was first determined and then the available discharge measurement was used to determine the average discharge rate d_F during these periods. The spray radius r_F was estimated from the mean AIR circumference measured in the drone surveys during the fountain runtime.

The Swiss fountain discharge duration was extrapolated from just one fountain on and off event each. Even though the Indian fountain was never manually switched off, there were many pipeline freezing events that interrupted the discharge duration. Discharge rate was extrapolated to be the mean discharge rate d_F except during these pipeline freezing events.

2.3 Drone Surveys

Several photogrammetric surveys using drones were conducted on the Swiss and Indian sites. The details of these surveys and the methodology used to produce the corresponding outputs are explained in **Supplementary Appendix 7.2**. The digital elevation maps (DEMs) generated from the obtained imagery were analysed to document the radius, surface area and volume of the ice structure. The number of surveys conducted for the IN21, CH21 and CH20 AIRs were six, eight and two, respectively (see **Table 2**). The first drone flight was used to set the dome volume (V_{dome}) for model initialisation. The remaining surveys were used for model calibration and validation. Since the Indian AIR was built on top of another ice structure (see **Figure 2**), it had a much higher dome volume compared to the other AIRs.

3 MODEL SETUP

A bulk energy and mass balance model is used to calculate the amounts of ice, meltwater, water vapour and wastewater of the AIR. In each hourly time step, the model uses the AIR surface area, energy balance and mass balance calculations to estimate its ice volume, surface temperature and wastewater as shown in **Figure 3**.

3.1 Surface Area Calculation

The model assumes the AIR shape to be a cone and assigns the following shape attributes:

$$A_{cone}^i = \pi \cdot r_{cone}^i \cdot \sqrt{(r_{cone}^i)^2 + (h_{cone}^i)^2} \quad (1a)$$

$$V_{cone}^i = \pi / 3 \cdot (r_{cone}^i)^2 \cdot h_{cone}^i \quad (1b)$$

$$j_{cone}^i = \frac{\Delta M_{ice}^i}{\rho_{water} * A_{cone}^i} \quad (1c)$$

where i denotes the model time step, r_{cone}^i is the radius; h_{cone}^i is the height; A_{cone}^i is the surface area; V_{cone}^i is the volume and j_{cone}^i is the AIR surface normal thickness change as shown in **Figure 4**. M_{ice}^i is the mass of the AIR and $\Delta M_{ice}^i = M_{ice}^{i-1} - M_{ice}^{i-2}$. Henceforth, the equations used display the model time step superscript i only if it is different from the current time step.

AIR volume can also be expressed as:

$$V_{cone} = \frac{M_{ice}}{\rho_{ice}} \quad (2)$$

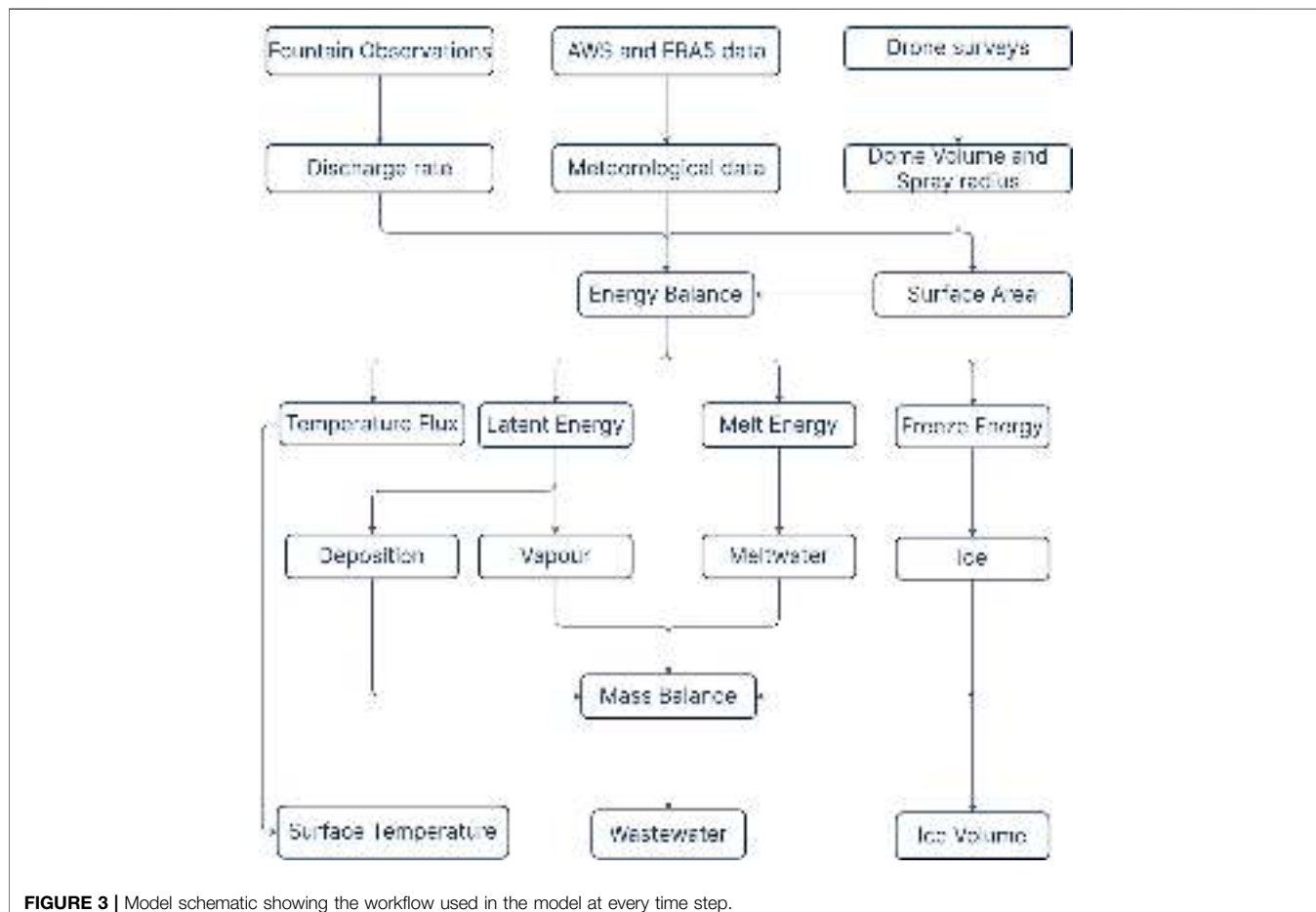


FIGURE 3 | Model schematic showing the workflow used in the model at every time step.

where ρ_{ice} is the density of ice (917 kg m^{-3}).

The initial radius of the AIR is assumed to be r_F . The initial height h_0 depends on the dome volume V_{dome} used to construct the AIR as follows:

$$h_0 = \Delta x + \frac{3 \cdot V_{dome}}{\pi \cdot (r_F)^2} \quad (3)$$

where Δx is the surface layer thickness (defined in Section 3.2)

During the subsequent time steps, the dimensions of the AIR evolve assuming a uniform thickness change (j_{cone}) across its surface area with an invariant slope $s_{cone} = \frac{j_{cone}}{r_{cone}}$. During these time steps, the volume is parameterised using Eq. 1b as:

$$V_{cone} = \frac{\pi \cdot (r_{cone})^3 \cdot s_{cone}}{3} \quad (4)$$

We define the Icestupa boundary through its spray radius, i.e. we assume ice formation is negligible when $r_{cone} > r_F$. Combining Eqs 1b, 2 Eqs 3, 4, 4, the geometric evolution of the Icestupa at each time step i can be determined by considering the following rules:

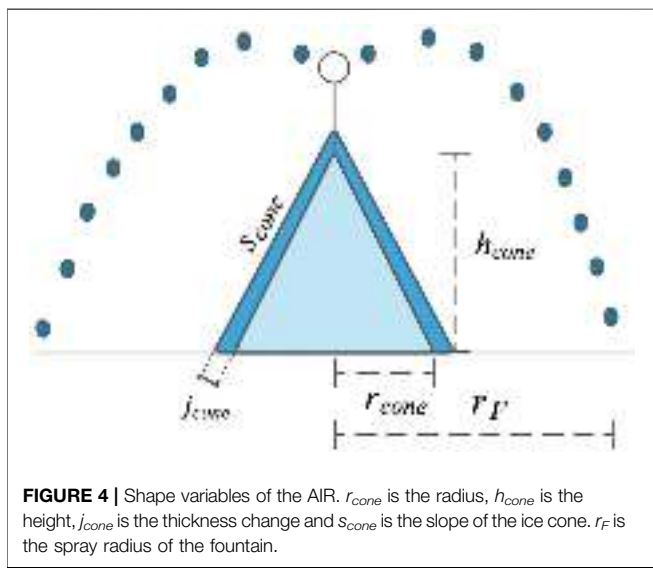
$$(r_{cone}, h_{cone}) = \begin{cases} (r_F, h_0) & \text{if } i = 0 \\ \left(r_{cone}^{i-1}, \frac{3 \cdot M_{ice}}{\pi \cdot \rho_{ice} \cdot (r_{cone}^{i-1})^2}\right) & \text{if } r_{cone}^{i-1} \geq r_F \text{ and } \Delta M_{ice} > 0 \\ \left(\frac{3 \cdot M_{ice}}{\pi \cdot \rho_{ice} \cdot s_{cone}}\right)^{1/3} \cdot (1, s_{cone}) & \text{otherwise} \end{cases} \quad (5)$$

3.2 Energy Balance Calculation

We approximate the energy balance at the surface of an AIR by a one-dimensional description of energy fluxes into and out of a (thin) layer with thickness Δx :

$$\rho_{ice} \cdot c_{ice} \cdot \frac{\Delta T}{\Delta t} \cdot \Delta x = q_{SW} + q_{LW} + q_L + q_S + q_F + q_G \quad (6)$$

Upward and downward fluxes relative to the ice surface are positive and negative, respectively. The first term is the energy change of the surface layer, which can be translated into a phase change energy should phase changes occur; q_{SW} is the net shortwave radiation; q_{LW} is the net longwave radiation; q_L and q_S are the turbulent latent and sensible heat fluxes. q_F represents the heat exchange of the fountain water droplets with the AIR ice surface. q_G represents ground heat flux between the AIR surface and its interior.



The energy flux acts upon the AIR surface layer, which has an upper and lower boundary defined by the atmosphere and the ice body of the AIR, respectively. A sensitivity analysis was later performed to understand the influence of this factor and decide its value. Here, we define the surface temperature T_{ice} to be the modelled average temperature of the icestupa surface layer.

3.2.1 Net Shortwave Radiation q_{SW}

The net shortwave radiation q_{SW} is computed as follows:

$$q_{SW} = (1 - \alpha) \cdot (SW_{direct} \cdot f_{cone} + SW_{diffuse}) \quad (7)$$

where SW_{direct} and $SW_{diffuse}$ are the direct and diffuse shortwave radiation, α is the modelled albedo and f_{cone} is the area fraction of the ice structure exposed to the direct shortwave radiation.

The albedo varies depending on the water source that formed the current AIR surface layer. During the fountain runtime, the albedo assumes a constant value corresponding to ice albedo. However, after the fountain is switched off, the albedo can reset to snow albedo during snowfall events and then decay back to ice albedo. We use the scheme described in Oerlemans and Knap (1998) to model this process. The scheme records the decay of albedo with time after fresh snow is deposited on the surface. δt records the number of time steps after the last snowfall event. After snowfall, albedo changes over a time step, δt , as

$$\alpha = \alpha_{ice} + (\alpha_{snow} - \alpha_{ice}) \cdot e^{(-\delta t)/\tau} \quad (8)$$

where α_{ice} is the bare ice albedo value (0.25), α_{snow} is the fresh snow albedo value (0.85) and τ is a decay rate (16 days), which determines how fast the albedo of the ageing snow recedes back to ice albedo.

The solar area fraction f_{cone} of the ice structure exposed to the direct shortwave radiation depends on the shape considered. Using the solar elevation angle θ_{sun} , the solar beam can be considered to have a vertical component, impinging on the

horizontal surface (semicircular base of the AIR), and a horizontal component impinging on the vertical cross section (a triangle). The solar elevation angle θ_{sun} used is modelled using the parametrisation proposed by Woolf (1968). Accordingly, f_{cone} is determined as follows:

$$f_{cone} = \frac{(0.5 \cdot r_{cone} \cdot h_{cone}) \cdot \cos \theta_{sun} + (\pi \cdot (r_{cone})^2 / 2) \cdot \sin \theta_{sun}}{\pi \cdot r_{cone} \cdot ((r_{cone})^2 + (h_{cone})^2)^{1/2}} \quad (9)$$

The diffuse shortwave radiation is assumed to impact the conical AIR surface uniformly.

3.2.2 Net Longwave Radiation q_{LW}

The net longwave radiation q_{LW} is determined as follows:

$$q_{LW} = LW_{in} - \sigma \cdot \epsilon_{ice} \cdot (T_{ice} + 273.15)^4 \quad (10)$$

where T_{ice} is the modelled surface temperature given in $^{\circ}\text{C}$, $\sigma = 5.67 \cdot 10^{-8} \text{ J m}^{-2} \text{s}^{-1} \text{K}^{-4}$ is the Stefan-Boltzmann constant, LW_{in} denotes the incoming longwave radiation and ϵ_{ice} is the corresponding emissivity value for the Icestupa surface (0.97).

The incoming longwave radiation LW_{in} for the Indian site, where no direct measurements were available, is determined as follows:

$$LW_{in} = \sigma \cdot \epsilon_a \cdot (T_a + 273.15)^4 \quad (11)$$

here T_a represents the measured air temperature and ϵ_a denotes the atmospheric emissivity. We approximate the atmospheric emissivity ϵ_a using the equation suggested by Brutsaert (1982), considering air temperature and vapor pressure (Eqn. 12). The vapor pressure of air over water and ice was obtained using Eq. (15). The expression defined in Brutsaert (1975) for clear skies (first term in equation 12) is extended with the correction for cloudy skies after Brutsaert (1982) as follows:

$$\epsilon_a = 1.24 \cdot \left(\frac{P_{v,w}}{(T_a + 273.15)} \right)^{1/7} \cdot (1 + 0.22 \cdot cld^2) \quad (12)$$

with a cloudiness index cld , ranging from 0 for clear skies to 1 for complete overcast skies. For the Indian site, we assume cloudiness to be negligible.

3.2.3 Turbulent Fluxes

The turbulent sensible q_s and latent heat q_L fluxes are computed with the following expressions proposed by Garratt (1992):

$$q_s = \mu_{cone} \cdot c_a \cdot \rho_a \cdot p_a / P_{0,a} \cdot \frac{\kappa^2 \cdot v_a \cdot (T_a - T_{ice})}{(\ln \frac{h_{AWS}}{z_0})^2} \quad (13)$$

$$q_L = \mu_{cone} \cdot 0.623 \cdot L_s \cdot \rho_a / P_{0,a} \cdot \frac{\kappa^2 \cdot v_a (P_{v,w} - P_{v,ice})}{(\ln \frac{h_{AWS}}{z_0})^2} \quad (14)$$

where h_{AWS} is the measurement height above the ground surface of the AWS (around 2 m for all sites), v_a is the wind speed in $[\text{m s}^{-1}]$, c_a is the specific heat of air at constant pressure ($1010 \text{ J kg}^{-1} \text{K}^{-1}$), ρ_a is the air density at standard sea level (1.29 kg m^{-3}), $P_{0,a}$ is the air pressure at standard sea level

(1013 hPa), p_a is the measured air pressure, κ is the von Karman constant (0.4), z_0 is the surface roughness (3 mm) and L_s is the heat of sublimation (2848 kJ kg⁻¹). The vapor pressure of air with respect to water ($p_{v,w}$) and with respect to ice ($p_{v,ice}$) was obtained using the formulation given in Huang (2018) :

$$\begin{aligned} p_{v,w} &= e^{\left(\frac{34.494 - \frac{4924.99}{T_a + 237.1}}{(T_a + 105)^{1.57 \cdot 100}}\right)} \cdot \frac{RH}{100} \\ p_{v,ice} &= e^{\left(\frac{43.494 - \frac{6545.89}{T_{ice} + 278}}{(T_{ice} + 868)^{2 \cdot 100}}\right)} \end{aligned} \quad (15)$$

The dimensionless parameter μ_{cone} is an exposure parameter that deals with the fact that AIR has a rough appearance and forms an obstacle to the wind regime. This factor accounts for the larger turbulent fluxes due to the roughness of the surface (Oerlemans et al., 2021), and is a function of the AIR slope as follows:

$$\mu_{cone} = 1 + \frac{s_{cone}}{2} \quad (16)$$

A possible source of error is the fact that wind measurements from the horizontal plane at the AWS are used, which might be different from those on a slope. However, without detailed datasets from the AIR surface, we retain this assumption.

3.2.4 Fountain Discharge Heat Flux q_F

The fountain water, at temperature T_F , is assumed to cool to 0 °C. Thus, the heat flux caused by this process is:

$$q_F = \frac{\Delta M_F \cdot c_{water} \cdot T_F}{\Delta t \cdot A_{cone}} \quad (17)$$

with c_{water} as the specific heat of water (4186 J kg⁻¹ K⁻¹).

3.2.5 Bulk Icestupa Heat Flux q_G

The bulk Icestupa heat flux q_G corresponds to the ground heat flux in normal soils and is caused by the temperature gradient between the surface layer (T_{ice}) and the ice body (T_{bulk}). It is expressed by using the heat conduction equation as follows:

$$q_G = k_{ice} \cdot (T_{bulk} - T_{ice}^{i-1}) / l_{cone} \quad (18)$$

where k_{ice} is the thermal conductivity of ice (2.123 W m⁻¹ K⁻¹), T_{bulk} is the mean temperature of the ice body within the icestupa and l_{cone} is the average distance of any point in the surface to any other point in the ice body. T_{bulk} is initialised as 0 °C and later determined from Eq. 18 as follows:

$$T_{bulk}^{i+1} = T_{bulk} - (q_G \cdot A \cdot \Delta t) / (M_{ice} \cdot c_{ice}) \quad (19)$$

Since AIRs typically have conical shapes with $r_{cone} > h_{cone}$, we assume that the center of mass of the cone body is near the base of the fountain. Thus, the distance of every point in the AIR surface layer from the cone body's center of mass is between h_{cone} and r_{cone} . Therefore, we calculate q_G assuming $l_{cone} = (r_{cone} + h_{cone})/2$.

3.2.6 Phase Changes

In this section, the numerical procedures to model phase changes at the surface layer are explained. Let T_{temp} be the calculated surface temperature. Therefore, Eq. (6) can be rewritten as:

$$q_{total} = \rho_{ice} \cdot c_{ice} \cdot \frac{(T_{temp} - T_{ice})}{\Delta t} \cdot \Delta x$$

where q_{total} represents the total energy available to be redistributed. Even if the numerical heat transfer solution produces temperatures which are $T_{temp} > 0^\circ\text{C}$, say from intense shortwave radiation, the ice temperature must remain at $T_{temp} = 0^\circ\text{C}$. The “excess” energy is used to drive the melting process. Moreover, the energy input is used to melt the surface ice layer, and not to raise the surface temperature to some unphysical value. Similarly, for freezing to occur, three conditions are required. Firstly, fountain water is present ($\Delta M_F > 0$) and secondly the calculated temperature of the ice, T_{temp} , is below 0 °C. However, these two conditions are not sufficient as the latent heat turbulent fluxes can only contribute to temperature fluctuations. Therefore, an additional condition, namely, $(q_{total} - q_L) < 0$, is required. Depending on the above conditions, the total energy q_{total} can be redistributed for the melting (q_{melt}), freezing (q_{freeze}) and surface temperature change (q_T) processes as follows:

$$q_{total} = \begin{cases} q_{freeze} + q_T & \text{if } \Delta M_F > 0 \text{ and } T_{temp} < 0 \text{ and } (q_{total} - q_L) < 0 \\ q_{melt} + q_T & \text{otherwise} \end{cases} \quad (20)$$

Henceforth, time steps when the total energy is redistributed to the freezing energy are called freezing events and the rest of the time steps are called melting events.

During a freezing event, the AIR surface is assumed to warm to 0 °C. The available energy ($q_{total} - q_L$) is further increased due to this change in surface temperature represented by the energy flux:

$$q_0 = \frac{\rho_{ice} \cdot \Delta x \cdot c_{ice} \cdot T_{ice}^{i-1}}{\Delta t}$$

The available fountain discharge (ΔM_F) may not be sufficient to utilize all the freezing energy. At such times, the additional freezing energy further cools down the surface temperature. Accordingly, the surface energy flux distribution during a freezing event can be represented as:

$$(q_{freeze}, q_T) = \begin{cases} \left(\frac{\Delta M_F \cdot L_f}{A_{cone} \cdot \Delta t}, q_{total} + \frac{\Delta M_F \cdot L_f}{A_{cone} \cdot \Delta t} \right) & \text{if } \Delta M_F \text{ insufficient} \\ (q_{total} - q_L + q_0, q_L - q_0) & \text{otherwise} \end{cases} \quad (21)$$

If $T_{temp} > 0^\circ\text{C}$, then energy is reallocated from q_T to q_{melt} to maintain surface temperature at melting point. The total energy flux distribution during a melting event can be represented as:

$$(q_{melt}, q_T) = \begin{cases} (0, q_{total}) & \text{if } T_{temp} \leq 0 \\ \left(\frac{T_{temp} \cdot \rho_{ice} \cdot c_{ice} \cdot \Delta x}{\Delta t}, q_{total} - \frac{T_{temp} \cdot \rho_{ice} \cdot c_{ice} \cdot \Delta x}{\Delta t} \right) & \text{if } T_{temp} > 0 \end{cases} \quad (22)$$

3.3 Mass Balance Calculation

The mass balance equation for an AIR is represented as:

$$\frac{\Delta M_F + \Delta M_{ppt} + \Delta M_{dep}}{\Delta t} = \frac{\Delta M_{ice} + \Delta M_{water} + \Delta M_{sub} + \Delta M_{waste}}{\Delta t} \quad (23)$$

where M_F is the cumulative mass of the fountain discharge; M_{ppt} is the cumulative precipitation; M_{dep} is the cumulative accumulation through water vapour deposition; M_{ice} is the cumulative mass of ice; M_{water} is the cumulative mass of melt water; M_{sub} represents the cumulative water vapor loss by sublimation and M_{waste} represents the fountain wastewater that did not interact with the AIR. The left hand side of Eq. 23 represents the rate of mass input and the right hand side represents the rate of mass output for an AIR.

Precipitation input is calculated as shown in Eq. 24b where ρ_w is the density of water (1000 kg m^{-3}), $\Delta ppt/\Delta t$ is the measured precipitation rate in [m s^{-1}] and T_{ppt} is the temperature threshold below which precipitation falls as snow. Here, snowfall events were identified using T_{ppt} as 1°C . Snow mass input is calculated by assuming a uniform deposition over the entire circular footprint of the AIR.

The latent heat flux is used to estimate either the evaporation and condensation processes or sublimation and deposition processes as shown in Equation (24c). During the time steps at which the surface temperature is below 0°C only sublimation and deposition can occur, but if the surface temperature reaches 0°C , evaporation and condensation can also occur. As the differentiation between evaporation and sublimation (and condensation and deposition) when the air temperature reaches 0°C is challenging, we assume that negative (positive) latent heat fluxes correspond only to sublimation (deposition), i.e. no evaporation (condensation) is calculated.

Since we have categorized every time step as a freezing or melting event, we can determine the melting/freezing rates and the corresponding meltwater/ice quantities as shown in Eqs 24e, 24d, and 24f. Having calculated all other mass components, the fountain wastewater generated every time step can be calculated using Eq. 23.

$$\frac{\Delta M_F}{\Delta t} = \begin{cases} \frac{60}{\rho_w \cdot \Delta t} \cdot d_F & \text{if fountain is on} \\ 0 & \text{otherwise} \end{cases} \quad (24a)$$

$$\frac{\Delta M_{ppt}}{\Delta t} = \begin{cases} \pi \cdot (r_{cone})^2 \cdot \rho_w \cdot \frac{\Delta ppt}{\Delta t} & \text{if } T_a < T_{ppt} \\ 0 & \text{if } T_a \geq T_{ppt} \end{cases} \quad (24b)$$

$$\left(\frac{\Delta M_{dep}}{\Delta t}, \frac{\Delta M_{sub}}{\Delta t} \right) = \begin{cases} \frac{q_L \cdot A_{cone}}{L_s} \cdot (1, 0) & \text{if } q_L \geq 0 \\ \frac{q_L \cdot A_{cone}}{L_s} \cdot (0, -1) & \text{if } q_L < 0 \end{cases} \quad (24c)$$

$$\frac{\Delta M_{water}}{\Delta t} = \frac{q_{melt} \cdot A_{cone}}{L_f} \quad (24d)$$

$$\frac{\Delta M_{freeze/melt}}{\Delta t} = \frac{q_{freeze/melt} \cdot A_{cone}}{L_f} \quad (24e)$$

$$\frac{\Delta M_{ice}}{\Delta t} = \frac{q_{freeze} \cdot A_{cone}}{L_f} + \frac{\Delta M_{ppt}}{\Delta t} + \frac{\Delta M_{dep}}{\Delta t} - \frac{\Delta M_{sub}}{\Delta t} - \frac{\Delta M_{water}}{\Delta t} \quad (24f)$$

Considering AIRs as water reservoirs, their net water loss can be defined as:

$$\text{Net water losses} = \frac{M_{waste} + M_{sub}}{(M_F + M_{ppt} + M_{dep})} \cdot 100 \quad (25)$$

3.4 Uncertainty Quantification

The uncertainty in the model of estimating ice volumes is caused by three sources, namely, model forcing data, model hyperparameters and model parameters. Model forcing data can further be divided into weather and fountain forcing data. Significant uncertainty exists in the weather forcing data, particularly for all the radiation measurements (SW_{direct} , $SW_{diffuse}$, LW_{in}) since they were taken from ERA5 dataset or an AWS far away from the construction sites. Since no other weather datasets exist for comparison, especially near the IN21 AIR, we are not accounting for uncertainties related to meteorological forcing data in this analysis. Uncertainty in the fountain forcing data arises due to only some fountain parameters listed in Table 3. Fountain runtime t_F has no uncertainty for the Swiss AIRs because no interruptions occurred during the study period. However, significant uncertainty exists for the IN21 AIR, where the interruptions due to pipeline freezing events happened overnight but this was ignored in this analysis. Fountain spray radius r_F was measured using the drone survey and therefore also doesn't contribute to model uncertainty. The choice of mean discharge rate d_F for both sites was just a best guess, based on few observations made by the flowmeter. So we associate this parameter by a large uncertainty of $\pm 50\%$. For the fountain water temperature T_F , we assumed an upper bound of 3°C since it is unlikely for it to have been beyond this range considering winter conditions at all the sites. The model structure introduces uncertainty through the spatial and temporal hyperparameters Δx and Δt . By definition, Δx is directly proportional to Δt . Therefore, we fix the temporal resolution of the model at hourly timesteps and only investigate the uncertainty caused by Δx here. Since the surface layer thickness for an AIR does not resemble to any parameter in the glaciological literature, we attribute a wide range of values for it (from 1 to 10 cm). The model parameters are henceforth called as weather parameters to distinguish them from the fountain forcing parameters. These were fixed within a range based on literature values (see Table 3).

The three types of uncertain parameters namely, model hyperparameters (Δx), fountain forcing parameters (d_F , T_F) and weather parameters (ϵ_{ice} , z_0 , α_{ice} , α_{snow} , T_{ppt} , τ) are denoted as Q^M , Q^F and Q^W henceforth. Together, these nine parameters cause a large uncertainty in the ice volume estimates. In order to reduce this uncertainty, we perform a global sensitivity analysis with the net water loss as our objective. The objective of this sensitivity analysis was to reduce the dimension of the parameter space by calibrating the parameters with high total-order sensitivities ($S_{T_j} > 0.5$). The methodology to determine S_{T_j} is described in Supplementary Appendix 7.3. These sensitive model parameters were calibrated based on the root mean squared error (RMSE) between the drone

TABLE 3 | Free parameters in the model categorised as constant, derived, model hyperparameters, weather and fountain forcing parameters with their respective values/ranges.

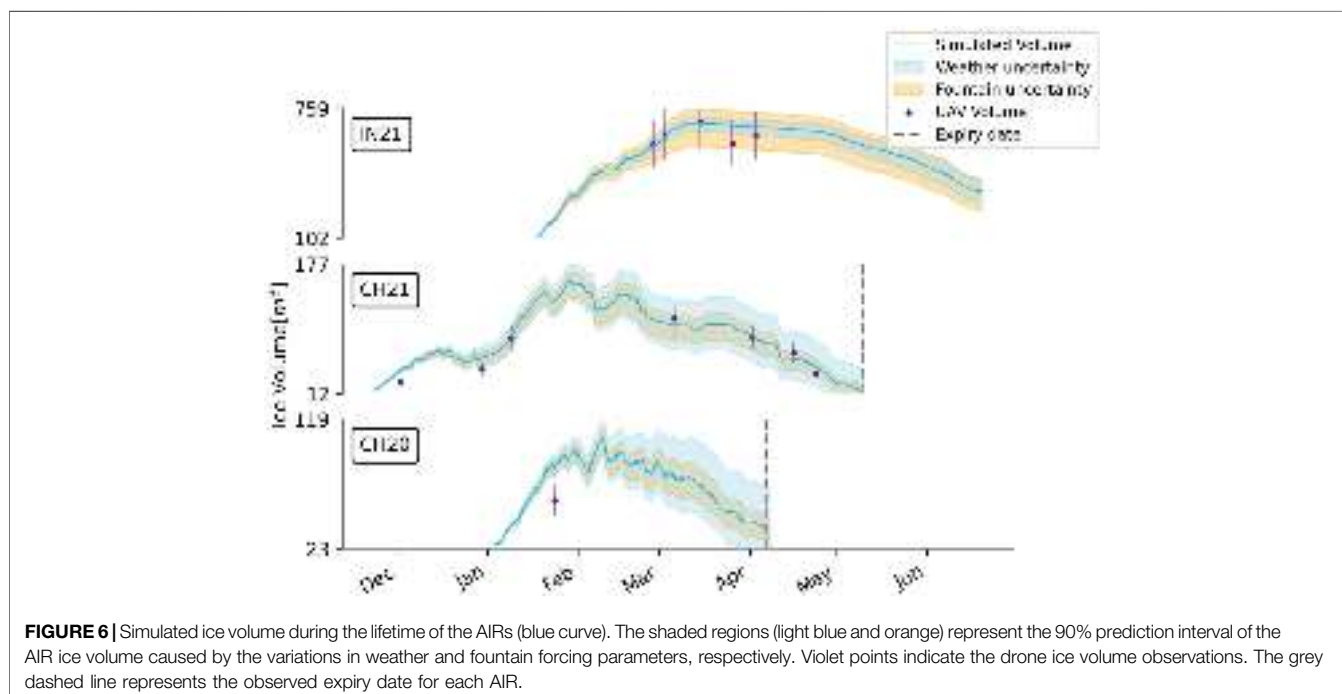
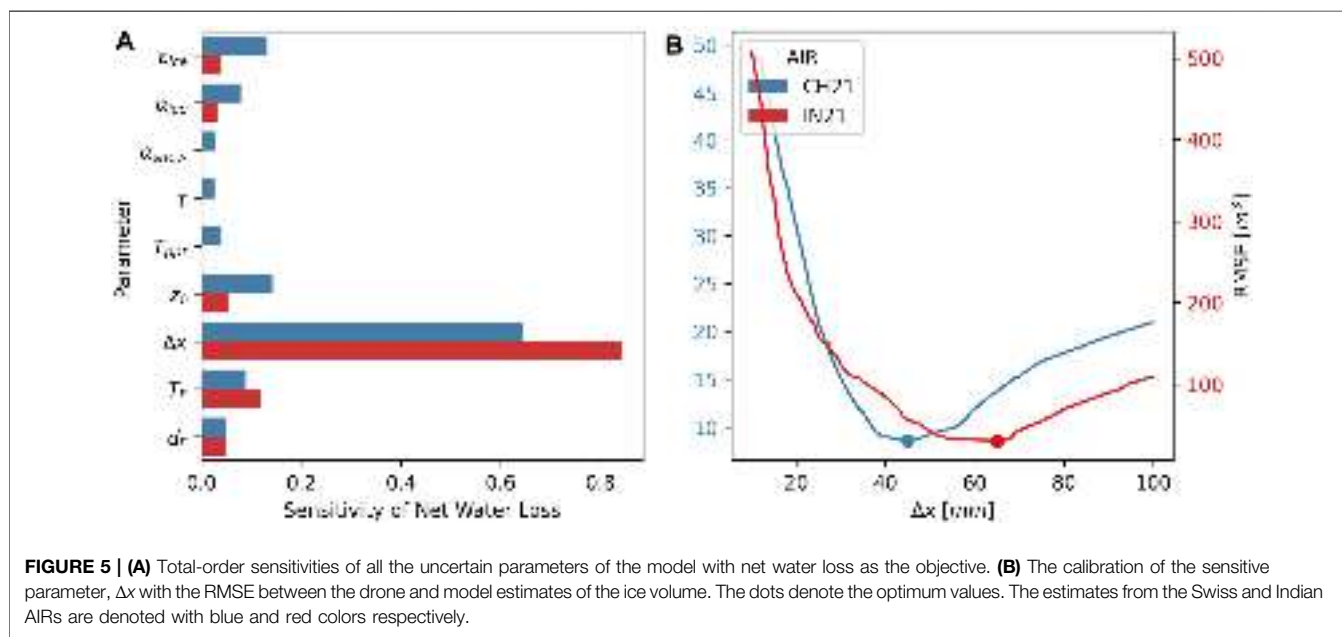
Constant parameters	Symbol	Value	Unit	References
Van Karman constant	κ	0.4	dimensionless	Cuffey and Paterson (2010)
Stefan Boltzmann constant	σ	5.67×10^{-8}	$W m^{-2} K^{-4}$	Cuffey and Paterson (2010)
Air pressure at sea level	$P_{0,a}$	1013	hPa	Mölg and Hardy (2004)
Density of water	ρ_w	1000	$kg m^{-3}$	Cuffey and Paterson (2010)
Density of ice	ρ_{ice}	917	$kg m^{-3}$	Cuffey and Paterson (2010)
Density of air	ρ_a	1.29	$kg m^{-3}$	Mölg and Hardy (2004)
Specific heat of water	c_w	4186	$J kg^{-1} ^\circ C^{-1}$	Cuffey and Paterson (2010)
Specific heat of ice	c_{ice}	2097	$J kg^{-1} ^\circ C^{-1}$	Cuffey and Paterson (2010)
Specific heat of air	c_a	1010	$J kg^{-1} ^\circ C^{-1}$	Mölg and Hardy (2004)
Thermal conductivity of ice	k_{ice}	2.123	$W m^{-1} K^{-1}$	Bonales et al. (2017)
Latent Heat of Sublimation	L_s	2.85×10^6	$J kg^{-1}$	Cuffey and Paterson (2010)
Latent Heat of Fusion	L_f	3.34×10^5	$J kg^{-1}$	Cuffey and Paterson (2010)
Gravitational acceleration	g	9.81	$m s^{-2}$	Cuffey and Paterson (2010)
Weather station height	h_{AWS}	2	m	assumed
Model timestep	Δt	3600	s	assumed
Fountain spray radius	r_F		m	measured
Fountain runtime	t_F		hours	measured
Derived Parameters	Symbol		Unit	Section
Radius of AIR	r_{cone}		m	3.1
Height of AIR	h_{cone}		m	3.1
Slope of AIR	s_{cone}		dimensionless	3.1
Thickness change of AIR	j_{cone}		m	3.1
Atmospheric emissivity	ϵ_a		dimensionless	3.2.2
Cloudiness	cl_d		dimensionless	assumed
Vapour pressure over water	$P_{v,w}$		hPa	3.2.3
Vapour pressure over ice	$P_{v,ice}$		hPa	3.2.3
Solar elevation angle	θ_{sun}		°	3.2.1
Albedo	α		dimensionless	3.2.1
Solar area fraction	f_{cone}		dimensionless	3.2.1
Ice body and surface distance	l_{cone}		m	3.2.5
AIR surface temperature	T_{ice}		°C	3.2.5
AIR bulk temperature	T_{bulk}		°C	3.2.5
Model Hyperparameters	Symbol	Range	Unit	References
Surface layer thickness	Δx	[$1e - 2, 1e - 1$]	m	assumed
Weather Parameters	Symbol	Range	Unit	References
Ice Emissivity	ϵ_{ice}	[0.95, 0.99]	dimensionless	Hori et al. (2006)
Surface Roughness	Z_0	[$1e - 3, 5e - 3$]	m	Brock et al. (2006)
Ice Albedo	α_{ice}	[0.15, 0.35]	dimensionless	Steiner et al. (2015)
Snow Albedo	α_{snow}	[0.8, 0.9]	dimensionless	Zolles et al. (2019)
Precipitation Temperature threshold	T_{ppt}	[0, 2]	°C	Zhou et al. (2010)
Albedo Decay Rate	τ	[10, 22]	days	Schmidt et al. (2017)
				Oerlemans and Knap (1998)
Fountain Forcing Parameters	Symbol	Range	Unit	References
Discharge rate	d_F	[$0.5 \cdot d_F, 1.5 \cdot d_F$]	l/min	assumed
Water temperature	T_F	[0, 3]	°C	assumed

surveys (see **Table 2**) and the model estimations of the ice volume. For this calibration procedure, all the other parameters were set to the median value of their respective ranges defined in **Table 3**. The sensitivity analysis and calibration were carried out with the drone surveys of CH21 and IN21 AIRs.

The model uncertainty was quantified separately for the remaining parameters in Q^M , Q^F and Q^W using the corresponding 90 % prediction interval I^M , I^F and I^W . The 90 % prediction interval, I^k ,

gives us the interval within which 90 % of the ice volume outcomes occur when all the parameters in Q^k are varied assuming each has an independent uniform probability density function. 5 % of the outcomes are above and 5 % are below this interval. The methodology to obtain this is described in **Supplementary Appendix 7.3**.

For validation, the calibrated model was tested with two datasets namely, the expiry date of all AIRs and the drone surveys of CH20 AIR.



4 RESULTS

4.1 Calibration of Sensitive Parameters

The total-order sensitivities of all the nine parameters with respect to the net water loss objective are shown in **Figure 5A**. In total, the global sensitivity analysis required 1432 model runs to determine these sensitivities for each site. The only sensitive parameter ($S_{T_j} > 0.5$) for both AIRs was the surface layer thickness. The RMSE between the drone surveys and the model ice volume estimates for different surface layer thickness are shown in **Figure 5B**. The optimum value of Δx was

found to be 45 and 65 mm with an RMSE of 9 m^3 and 30 m^3 for CH21 and IN21 AIRs respectively.

4.2 Weather and Fountain Forcing Uncertainty Quantification

The uncertainty in the ice volume estimates caused by the weather and fountain forcing parameters are shown in **Figure 6**. The ranges highlighted represent the corresponding 90 % prediction interval of the ice volume estimates. Weather

uncertainty determination required 422 simulations whereas fountain forcing uncertainty determination required 32 simulations for each AIR. Since the results presented below differ significantly during the fountain runtime, we divided the simulation duration of the AIR into accumulation and ablation periods. The accumulation (ablation) period ends (starts) at the last fountain discharge event.

The prediction interval of the weather and fountain forcing parameters behave differently during the accumulation and ablation period for all AIRs. Prediction interval of the weather parameters increase throughout the simulation period, but that of the fountain forcing parameters only increase during the accumulation period. This is to be expected since the fountain forcing parameters directly affect the model estimates only during the accumulation period.

Weather uncertainty for the Indian site was low compared to the Swiss since precipitation and the associated variation in albedo was negligible. At the end of the accumulation period, the Indian weather prediction interval had a magnitude of 73 m^3 which was 10 % of the maximum simulated volume, whereas the magnitude of the Swiss weather prediction interval was much higher (28 % of the maximum simulated volume for the CH21 AIR). This was expected since four out of the six uncertain Indian weather parameters were part of the albedo module. Among all the weather parameters, surface roughness caused the most variance in both Indian and the Swiss ice volume estimates.

Fountain forcing uncertainty for the Indian site was higher than its weather uncertainty (28 % of the maximum simulated volume at the end of the accumulation period). This was predominantly due to the uncertainty in the fountain's water temperature. However, for the Swiss site, the prediction interval of the fountain forcing parameters was similar to that of the weather parameters during the accumulation period. Since the mean fountain discharge rate of the Indian location was eight times that of the Swiss, the uncertainty due to the fountain forcing parameters was expected to be larger for the Indian location.

4.3 Validation

Model performance can be judged based on the ice volume left on the expiry date of all AIRs. In the case of CH21 AIR no ice volume was left whereas for CH20 AIR ice volume of 12 m^3 was left on the expiry date. For the IN21 AIR, the determination of the expiry date was not possible. In reality, the IN21 AIR was found to have disintegrated into several ice blocks on 20th June 2021.

There was also one drone survey of the CH20 AIR volume for validation purposes (see Table 2). The RMSE of that observation with the modelled volume was 19 m^3 which is 18 % of the maximum simulated ice volume of CH20 AIR.

4.4 AIR Ice Volume Estimates

Since this model used a surface energy balance model commonly applied on glaciers, we analyse the AIR temporal and spatial variation similar to how it is done for a glacier. Particularly, we used the AIR surface normal thickness change (j_{cone}) as a measure to quantify the location influence. Note that j_{cone} is

similar to the "specific mass balance" of a glacier with units *m w.e.*. The thickness change during the accumulation and ablation period was referred to as thickness growth and decay, respectively.

The construction decisions responsible for the observed magnitude and variance of the ice volume estimates can be categorised based on the fountain used and the location selected. According to Eq. 24e, the freezing/melting rate of the AIRs can be decomposed to the corresponding freezing/melting energy and the surface area. The construction location chosen determines the thickness growth/decay through the freezing/melting energy flux and the fountain determines the surface area through its spray radius.

The influence of location can be further comprehended if we analyse the daily surface normal thickness change together with the corresponding energy fluxes. Figure 7 shows the daily thickness and energy balance components calculated with the calibrated surface layer thickness for the first and last 20 days for each AIR. The two time periods selected were characteristic of the accumulation and ablation period, respectively. A strong variability was evident between the accumulation and ablation periods and between the CH21 and the IN21 AIRs.

The daily mean thickness change of the Indian location was positive (3 mm w.e.) with a daily mean growth of 31 mm w.e. and a mean decay of 11 mm w.e. In the Swiss location, the daily mean thickness change was negative (-4 mm w.e.) with a daily mean thickness growth of 8 mm w.e. and a mean decay of 18 mm w.e. The difference in magnitude between the growth and the decay corresponds to the difference between the freezing and the melting energy balance components. For the Indian site, q_{freeze} accounted for 73 %, q_{melt} accounted for 23 % and q_T just 4 % of overall energy turnover. The energy turnover is calculated as the sum of energy fluxes in absolute values. For the Swiss site, q_{freeze} accounted for 37 %, q_{melt} accounted for 61 % and q_T just 2 % of overall energy turnover. The freezing events occurred for 19 and 34% of the simulation duration (see Table 1) for the Indian and Swiss sites, respectively. The accumulation period is characteristic of these freezing events and the ablation period is characteristic of the melting events. We compare the energy turnover of different energy fluxes between these two periods to quantify the influence of different surface processes.

To understand the overall impact of the radiation fluxes (longwave and shortwave) and the turbulent fluxes (sensible and latent) on the freezing and melting energies, we sum their respective energy turnover by taking into account the sign of their mean energy during the accumulation/ablation period (see Table 4). A negative sign indicates that the corresponding energy flux increased/decreased the freezing/melting energy respectively. Note that all energy fluxes maintain the same sign for both accumulation and ablation periods for the Indian location, but the latent heat changes sign for the Swiss location. The radiation fluxes contributed -27 and 0 % to the freezing and melting energies for the Indian location and -20 % and -6 % to the Swiss location, respectively. Similarly, the turbulent fluxes at the Indian location contribute -11 and 10 % and at the Swiss location contribute 12 and 49% respectively. Therefore, the

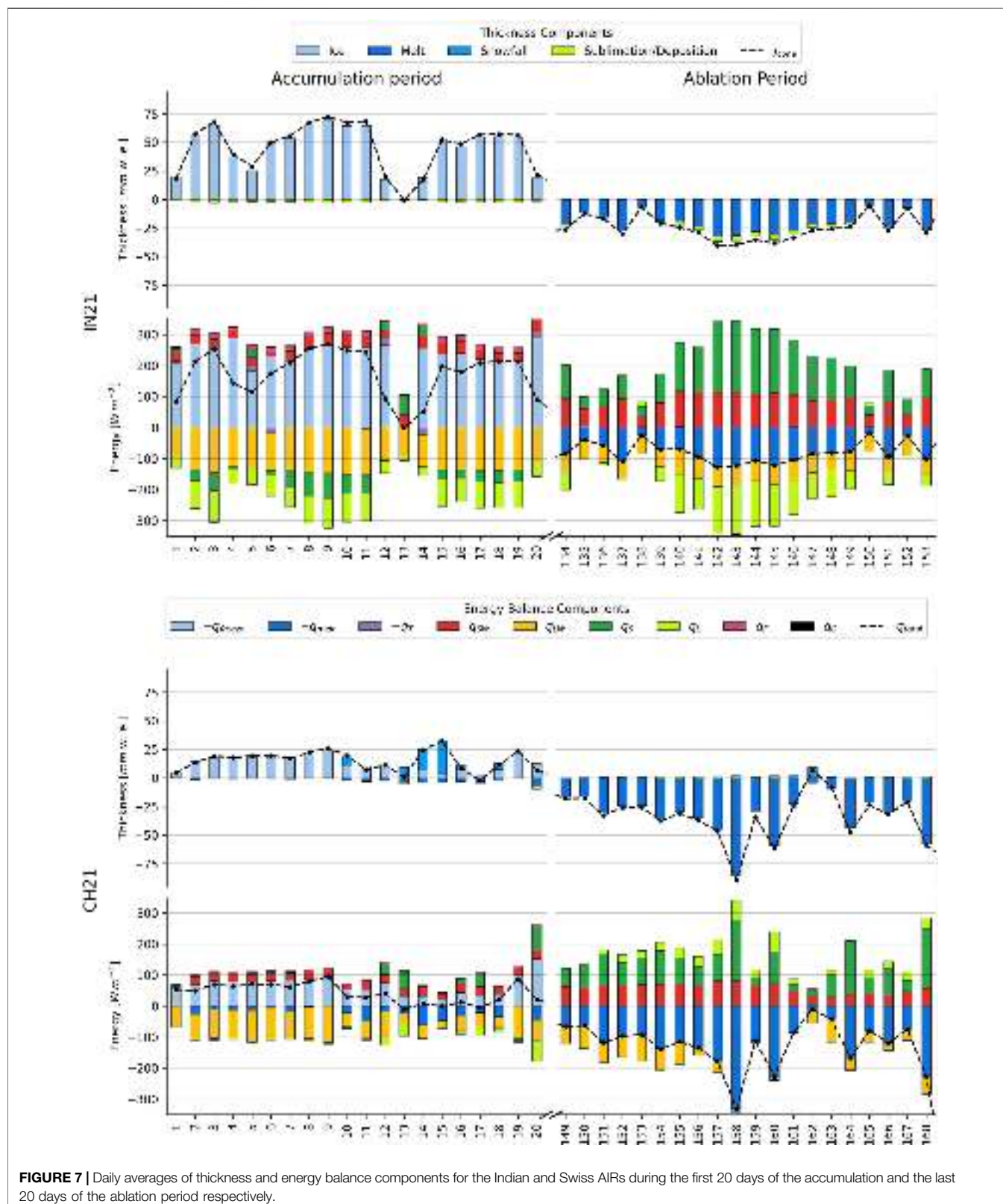


FIGURE 7 | Daily averages of thickness and energy balance components for the Indian and Swiss AIRs during the first 20 days of the accumulation and the last 20 days of the ablation period respectively.

AIR thickness growth was driven by the net radiation fluxes and the AIR thickness decay was driven by the net turbulent fluxes.

The longwave radiation flux had the highest energy turnover during the accumulation period for both locations. It increased and decreased the freezing and melting energy balance

components during the accumulation and ablation period, respectively. However, its magnitude was much lower in the ablation period compared to the accumulation period since the rising air temperature increased the incoming longwave radiation in the ablation period. The mean longwave radiation flux (see **Table 4**) was lower for the Indian site as its incoming longwave radiation was strongly reduced due to cloud free skies. (see **Table 1**).

Global shortwave radiation was around two times higher for the Indian location due to its higher altitude and lower latitude. However, the energy turnover of the shortwave radiation for both sites were similar (see **Table 4**). The main cause of this is the differential exposure of a conical structure to direct and diffuse fractions of global shortwave radiation. This effect is quantified by the area fraction parameter f_{cone} . Less than 20 % of the AIR surface area on average was exposed to direct shortwave radiation flux for both locations. Cloudy days increase the diffuse fraction of global shortwave radiation. Therefore, the net shortwave radiation impact for the Indian site was significantly reduced as the study period had mostly clear days. Since the Swiss site had many cloudy days, its higher diffuse shortwave radiation enhanced the net shortwave radiation impact (see **Table 1**). Temporal variation in the f_{cone} factor due to increasing solar elevation angle and decreasing AIR slope leads to higher shortwave radiation in the ablation period compared to the accumulation period. Albedo, on the other hand, only varied temporally for the Swiss location because there was no precipitation for the Indian site.

Turbulent fluxes play an essential role in the energy balance. Sensible heat fluxes had the highest energy turnover during the ablation period for both locations. It decreased and increased the freezing and melting energy balance components respectively. The Indian location had a much higher sensible heat due to higher wind speeds and higher temperature gradient between the AIR surface and the atmosphere. The sensible heat contributes much more to the energy turnover during ablation period than the latent heat flux due to rising air temperature. Alternatively, latent heat flux does not vary much in energy turnover between the accumulation and ablation periods. For the Indian site, latent heat flux increased and decreased the freezing and melting energy, since sublimation was favoured throughout the simulation duration. On the contrary, for the Swiss location, latent heat increased both the freezing and the melting energy, as sublimation and deposition were favoured during the accumulation and ablation periods, respectively.

The mass contribution of the sublimation/deposition process (shown in **Table 5**) was significantly smaller than the energy flux contribution of this process (shown in **Table 4**), since the heat of vaporization is around nine times higher than the heat of fusion. The magnitude of the sublimation/deposition process was significantly different for both AIRs: IN21 AIR lost 2 % of its mass input to sublimation compared to the 1 % mass loss of CH21 AIR (see **Table 5**). For the IN21 AIR, the mass gain due to deposition was an order of magnitude smaller than the mass loss due to sublimation. For the CH21 AIR, there were no significant differences between the mass lost by sublimation and the mass gained by deposition. This was expected, since glaciers near the

TABLE 4 | Contribution of the energy balance components (EBC) to the total energy turnover (the sum of energy fluxes in absolute values) during the accumulation and ablation periods with their daily mean (μ) and standard deviation (σ) for each site. The positive/negative sign is indicative of the upward/downward direction of the mean energy flux during the respective period.

	EBC	Accumulation	Ablation	$\mu \pm \sigma$
IN21	q_{SW}	16 %	25 %	$65 \pm 99 W m^{-2}$
	q_{LW}	-43 %	-25 %	$-89 \pm 27 W m^{-2}$
	q_S	13 %	30 %	$63 \pm 73 W m^{-2}$
	q_L	-24 %	-20 %	$-63 \pm 62 W m^{-2}$
	q_F	4 %	0 %	$4 \pm 7 W m^{-2}$
	q_G	0 %	0 %	$1 \pm 1 W m^{-2}$
CH21	q_{SW}	21 %	23 %	$38 \pm 58 W m^{-2}$
	q_{LW}	-41 %	-29 %	$-60 \pm 32 W m^{-2}$
	q_S	23 %	39 %	$47 \pm 99 W m^{-2}$
	q_L	-11 %	10 %	$-6 \pm 40 W m^{-2}$
	q_F	3 %	0 %	$3 \pm 3 W m^{-2}$
	q_G	0 %	0 %	$0 \pm 1 W m^{-2}$

IN21 location have been hypothesized to lose a significant amount of their mass through sublimation, as suggested by Azam et al. (2018).

The fountain had some influence on the energy fluxes through its water temperature, temperature forcing and albedo forcing. However, this influence was insignificant compared to its influence on the surface area which was directly proportional to the fountain's spray radius during the accumulation period. Therefore, the thickness growth was uniformly scaled to produce the corresponding ice volume. Additionally, the higher spray radius of the Indian fountain resulted in a higher maximum ice volume. Nonetheless, this was accompanied by an earlier expiry date, as a larger surface area increased both the freezing and the melting rate.

5 DISCUSSION

5.1 Model Limitations

5.1.1 Fountain Quantification

The model requires the fountain spray radius to be provided as input. This is a significant limitation since the model is very sensitive to the spray radius parameter. Moreover, r_F is not only determined by the fountain characteristics but also due to refreezing and melting events across the AIR perimeter. Therefore, the same fountain may produce different spray radius under different weather conditions.

Contrary to our model assumptions, the parameters used to define the fountain were not independent. The fountain height, fountain aperture diameter (both ignored in this analysis), discharge rate, water temperature and spray radius were related through the trajectories of the water droplets. Particularly, the temporal variation of both the spray radius and the water temperature were completely ignored in the model. During the IN21 experiment, snow formation was observed, indicating that the fountain water droplets have the potential to freeze before deposition on the AIR surface. Modelling such processes would require modelling the conduction, convection and nucleation processes that all droplets undergo during their flight time. Therefore, a proper quantification of the fountain is

TABLE 5 | Summary of the mass balance and AIR characteristics estimated at the end of the respective simulation duration.

	Name	Symbol	IN21	CH21	Units
Input	Fountain discharge	M_F	2.90×10^6	9.70×10^5	kg
	Snowfall	M_{ppt}	0	5.60×10^4	kg
	Deposition	M_{dep}	6.30×10^3	4.10×10^3	kg
Output	Meltwater	M_{water}	2.40×10^5	2.30×10^5	kg
	Ice	M_{ice}	2.20×10^5	2.90×10^2	kg
	Sublimation	M_{sub}	4.80×10^4	5.20×10^3	kg
	Fountain wastewater	M_{waste}	2.50×10^6	8.00×10^5	kg
AIR	Freezing rate	$\Delta M_{freeze}/\Delta t$	11 ± 7	1 ± 2	l/min
	Melting rate	$\Delta M_{melt}/\Delta t$	2 ± 4	1 ± 2	l/min
	Thickness change	j_{cone}	3 ± 25	-4 ± 27	mm w. e.
	Net Water Loss		81	77	%
	Maximum Ice Volume		685	155	m^3
	Surface Area	A_{cone}	350 ± 38	127 ± 34	m^2
Model	Surface layer thickness	Δx	65	45	mm
	RMSE with ice volume		41	10	m^3
	Correlation with ice volume		0.98	0.96	N.A.

much more complex and requires a closer look at the correlation of the fountain parameters amongst themselves and with the weather parameters. This will be investigated in a follow-up study, with this study focusing on the weather aspects of the model.

5.1.2 Shape Assumption

The RMSE between the drone and the model estimates of the surface area for the IN21, CH21 and CH20 AIRs were 69 %, 25 and 65 % of the maximum area of the respective AIRs (see Table 2). There are two crude assumptions that lead to such a large error namely, assuming a conical shape and assuming a constant spray radius.

Both these assumptions are a consequence of favoring model simplicity over accuracy. One could, for example, model the AIR shape assuming its cross section is a gaussian curve instead of a triangle. But such methodologies will involve the inclusion of even more model parameters.

5.2 Model Calibration, Validation and Uncertainty

The calibration process used has an inherent temporal and spatial bias due to the choice of when and how many drone surveys were possible in each location. Among the five surveys of IN21 AIR used for calibration, most of them were conducted around early March when the AIR volume was near its maximum whereas the seven surveys of the CH21 location were more evenly spaced out in comparison (see Table 2). Moreover, the fountain spray radius is also biased as a consequence leading to further model error. Overestimation of CH20 AIR's spray radius could be one of the reasons we observe an overestimation of its volume since the spray radius is derived from just one drone survey closer to the end of the accumulation period.

The calibration methodology assumed no correlation between the sensitive model hyperparameter Δx and the other eight parameters. Since for all AIRs, the total order sensitivity of Δx

and the rest of the parameters was greater and lesser than 0.6 and 0.1, respectively, this was a reasonable assumption to make.

Theoretically, the parameter selection for Δx is based on the following two arguments: (a) the ice thickness Δx should be small enough to represent the surface temperature variations at every model time step Δt and (b) Δx should be large enough for these temperature variations to not reach the bottom of the surface layer. The minimum modelled ice and bulk temperatures decrease and increase with increasing Δx . Thus, we can reframe conditions (a) and (b) in terms of the relationship between T_{ice} , T_{bulk} and Δx . For example, all three AIRs studied had similar minimum modelled surface and bulk temperature around -24°C and -3°C respectively. Compared to T_{bulk} , the value of T_{ice} is not too high in accordance with (a) and not too low in accordance with (b). The magnitude of the difference expected between T_{ice} and T_{bulk} can be fixed with additional spatial and temporal ice temperature measurements of the AIR. This would lead to a better calibrated Δx . Therefore, uncertainty of the model could have been significantly reduced if such a temperature dataset had been available.

Practically, the surface layer thickness was also the only parameter compensating for the model's shape assumption. Since two AIRs merged to create the IN21 AIR, it had a drastically different shape evolution compared to the CH21 AIR. This also resulted in the different calibrated values of Δx in the Indian and the Swiss locations.

Uncertainty caused due to the other model parameters could also have been significantly reduced with further measurements. In particular, the fountain forcing parameters could have been avoided with a complete discharge rate dataset. Four out of the six uncertain weather parameters namely, α_{ice} , α_{snow} , τ and T_{ppt} could have been better constrained through periodic measurements with an albedometer and a snow height sensor.

The model results highlight the high water losses in all the chosen locations. This could have been verified independently if all AIR meltwater and wastewater had been stored in a tank. But there were

two location-specific conditions that prevented us from doing so. First, the terrain of the site needs to be waterproof and oriented so that most of the AIR runoff can be collected. Second, the chosen location should not have high wind speeds, otherwise a significant fraction of AIR wastewater would be dispersed in the air. Both these conditions were not met for our chosen locations, hence efforts to measure the AIR runoff were abandoned. However, in an ideal location, this dataset could serve as a superior way to validate the model compared to the drone surveys which are also used for determining the spray radius.

5.3 Water Losses of AIRs

The net water losses of IN21 and CH21 AIR were 81 and 77 % of the total mass input, respectively. The high water losses were caused by the fountain wastewater for both AIRs. Therefore, AIRs lose water mostly during the accumulation period. The freezing rate of the IN21 AIR was less than 20 l min^{-1} for more than 90 % of the accumulation period, meaning that the growth was not limited by the water supply rate but rather by the freezing rate. The CH21 AIR freezing rate was able to reach the mean fountain discharge rate provided, albeit for only 2 h out of the 2155 h of fountain runtime available.

5.4 Fountain Optimization

Water losses could have been reduced in two ways: (a) reducing the fountain runtime t_F and (b) decreasing the mean fountain discharge rate d_F . For the CH21 AIR, strategy (a) could have saved considerable wastewater as no freezing was possible for 37 % of the accumulation period. For the IN21 site, strategy (b) would have yielded the least water loss as the freezing rate was more than half the mean discharge rate for just 2 hours. However, strategy (b) will also lead to a reduction in r_F if it is not accompanied by a suitable change in the fountain height and aperture diameter. So it can only be applied using the model if the corresponding fountain parameters are better parameterised.

Practically, both strategies are difficult to apply. It is unrealistic to expect someone constantly switching the fountain on and off under subzero conditions in accordance with strategy (a). Yes, strategy (b) is comparatively easier, but the minimum discharge rate is further constrained by the critical discharge rate below which the pipeline will freeze. However, both strategies can simultaneously be applied if the construction process is completely automated via a system that regulates the discharge in accordance with the model freezing estimates. Such a system can also drain the complete pipeline to prevent any pipeline freezing events. Since none of these functions are energy intensive, this system can be deployed anywhere using a solar powered energy source.

5.5 Favourable AIR Locations

Weather conditions play a significant role in making the Indian AIR larger and survive longer than the Swiss AIR, namely cloudiness, temperature and relative humidity. The lower cloudiness and mean winter temperature of the Indian location significantly reduced the net radiation flux during the accumulation period, enabling a faster AIR thickness growth. The lower winter temperature and humidity favour the sublimation over the deposition process, thus decreasing the magnitude of net turbulent fluxes during the ablation period. This results in a slower thickness decay. For AIRs with similar

fountain parameters, we expect locations with lower cloudiness, lower mean winter temperature to augment freezing rates and locations with lower humidity to dampen melting rates. Hence, AIRs should be considered in the water resource management strategy particularly of dry and cold mountain regions such as in Central Asia or the Andes where few other sustainable and affordable alternatives exist.

5.6 Model Application in New Locations

Since the model has been validated in two drastically different weather conditions and uses a methodology similar to the ones used on glaciers worldwide, we believe its performance should be similar in any other location.

The meteorological data and some fountain parameters are necessary to obtain modelled ice volume estimates. The necessary fountain parameters are r_F and t_F . The fountain runtime can be defined either with a fountain on and off date parameter or with a CSV file. Additionally, if d_F is known, the associated water losses can also be determined. As discussed before, the model is very sensitive to r_F , therefore it is recommended to manually measure the spray radius with the chosen fountain and pipeline.

All weather parameters can be assumed to have the median values of their ranges defined in **Table 3**. The model hyperparameter Δx needs to be calibrated beforehand. For a new location, we can use the surface layer thickness of CH21 AIR (45 mm) since it is representative of the shape evolution of a conical AIR.

The model is written in Python and completely based on open-source libraries. The model, source code, case studies and code examples for data preprocessing are provided on a freely accessible Git repository (https://github.com/Gayashiva/air_model, last access: December 17, 2021) for non-profit purposes. As a vision for the future, it is conceivable to extend the model for automatic AIR construction and foster a space where scientific and mountain communities can develop and apply various water resource management strategies together.

6 CONCLUSION

In this paper, we have developed a bulk energy and mass balance model to simulate AIR evolution using data from field measurements in Ganges, India and Guttannen, Switzerland. The use of these datasets, in combination with the novel model, allowed for an accurate representation of the complex evolution that is typical of an AIR. The model was calibrated and validated with ice volume and surface area observations obtained via drone surveys. We calculated the freezing and melting rates for each of the three AIRs and explained their corresponding magnitudes in terms of the influence of the chosen location and the fountain used. Our main conclusions are summarized below:

- The model was successful in reproducing the observed ice volume evolution with a correlation greater than 0.96 and an RMSE less than 18 % of the maximum ice volume for all AIRs.
- The ice volume achieved after the accumulation period was much higher for the Indian AIR compared to the Swiss AIRs. The lower net radiation fluxes of the Indian location favored a

faster thickness growth and the spray radius of the Indian fountain produced a higher surface area compared to the Swiss counterparts. Thus, the more than three times higher mean surface area and four times higher mean thickness growth during the two times shorter accumulation period of the Indian location resulted in a four times higher maximum ice volume of the Indian AIR compared to the Swiss.

- The ablation period of the Indian AIR was longer than the Swiss AIRs. However, the lower turbulent fluxes resulted in a slower thickness decay on a larger surface area. This rendered the differences between the IN21 and CH21 melting rates negligible. Since the accumulation period produced much higher ice volumes, the Indian AIR was able to last much longer than the Swiss AIRs.
- Water losses were high (> 77 %) mostly due to fountain wastewater for all AIRs. Vapour losses were insignificant (< 2 %) in comparison. However, a significant reduction in water loss is possible through optimization of fountain discharge rate.
- The Indian construction site produced long-lasting AIRs with higher maximum ice volumes since it was colder, drier and less cloudy compared to the Swiss construction site. Thus, the AIR technology is ideally suited to serve as a water management strategy, especially in dry and cold mountain regions such as in Central Asia or the Andes impacted by climate change induced water stress.

DATA AVAILABILITY STATEMENT

Model code is freely available on GitHub (https://github.com/Gayashiva/air_model, last access: 17 December 2021) for non-profit purposes. The drone data can be obtained from the authors upon request.

AUTHOR CONTRIBUTIONS

SB, MH, SW, and FK designed the study. SB developed the methodology with inputs from MH. MH, ML, and JO reviewed the algorithm and helped improve it. SB processed the drone data.

REFERENCES

- Apel, H., Abdykerimova, Z., Agalhanova, M., Baimaganbetov, A., Gavrilenko, N., Gerlitz, L., et al. (2018). Statistical Forecast of Seasonal Discharge in central Asia Using Observational Records: Development of a Generic Linear Modelling Tool for Operational Water Resource Management. *Hydrol. Earth Syst. Sci.* 22, 2225–2254. doi:10.5194/hess-22-2225-2018
- Azam, M. F., Wagnon, P., Berthier, E., Vincent, C., Fujita, K., and Kargel, J. S. (2018). Review of the Status and Mass Changes of Himalayan-Karakoram Glaciers. *J. Glaciol.* 64, 61–74. doi:10.1017/jog.2017.86
- Bonales, L. J., Rodriguez, A. C., and Sanz, P. D. (2017). Thermal Conductivity of Ice Prepared under Different Conditions. *Int. J. Food Properties* 20, 610–619. doi:10.1080/10942912.2017.1306551
- Brock, B. W., Willis, I. C., and Sharp, M. J. (2006). Measurement and Parameterization of Aerodynamic Roughness Length Variations at Haut Glacier d'Arolla, Switzerland. *J. Glaciol.* 52, 281–297. doi:10.3189/172756506781828746
- Brutsaert, W. (1982). *Evaporation into the Atmosphere. Theory, History and Application.* Kluwer Academic Publishers.
- Brutsaert, W. (1975). On a Derivable Formula for Long-Wave Radiation from clear Skies. *Water Resour. Res.* 11, 742–744. doi:10.1029/WR011i005p00742
- Buytaert, W., Moulds, S., Acosta, L., De Bièvre, B., Olmos, C., Villacis, M., et al. (2017). Glacial Melt Content of Water Use in the Tropical andes. *Environ. Res. Lett.* 12, 114014. doi:10.1088/1748-9326/aa926c
- Chen, Y., Li, W., Deng, H., Fang, G., and Li, Z. (2016). Changes in central Asia's Water tower: Past, Present and Future. *Nature* 6, 35458. doi:10.1088/1748-9326/aa926c
- [Dataset] Copernicus Climate Change Service (C3S) (2017). Era5: Fifth Generation of Ecmwf Atmospheric Reanalyses of the Global Climate. Available at <https://cds.climate.copernicus.eu/cdsapp#!/home> (Accessed 10 01, 2019).
- Cuffey, K. M., and Paterson, W. S. B. (2010). *The Physics of Glaciers.* Elsevier.
- Furukawa, Y., and Ponce, J. (2010). Accurate, Dense, and Robust Multiview Stereopsis. *IEEE Trans. Pattern Anal. Mach. Intell.* 32, 1362–1376. doi:10.1109/TPAMI.2009.161

SB wrote the model code. JB helped with model validation and uncertainty assessment. SB, MH, FK, and SW participated in the fieldwork. SB led the writing of the paper and all co-authors contributed to it.

FUNDING

This work was supported and funded by the University of Fribourg and by the Swiss Government Excellence Scholarship (SB). The associated fieldwork in India was supported by the Himalayan Institute of Alternatives and funded by the Swiss Polar Institute.

ACKNOWLEDGMENTS

This work would not have been possible without the untiring efforts of the Swiss and Indian icerupa construction teams through the winters of 2019, 2020, and 2021. We thank Mr. Adolf Kaeser and Mr. Flavio Catillaz from Eispalast Schwarzsee (CH19); Daniel Bürki from the Guttannen Bewegt Association (CH20 and CH21); Norboo Thinles, Nishant Tiku, Sourabh Maheshwari and the rest of the HIAL team (IN21). We would also like to thank Hansueli Gubler for designing the Swiss AWS; Dr. Tom Matthews for designing the Indian AWS; Michelle Stirnimann for conducting the CH20 drone surveys and Digmesa AG for subsidising their flowmeter used in the experiment. We would particularly like to thank Prof. Thomas Schuler and 4 reviewers who gave us important inputs to improve the paper. We also thank Prof. Christian Hauck, Prof. Nanna B. Karlsson Dr. Andrew Tedstone and Alizé Carrère for valuable suggestions that improved the manuscript.

SUPPLEMENTARY MATERIAL

The Supplementary Material for this article can be found online at: <https://www.frontiersin.org/articles/10.3389/feart.2021.771342/full#supplementary-material>

- Garratt, J. R. (1992). *The Atmospheric Boundary Layer*. Cambridge University Press.
- Grossman, D. (2015). As Himalayan Glaciers Melt, Two Towns Face the Fallout. Available at https://e360.yale.edu/features/as_himalayan_glaciers_melt_two_towns_face_the_fallout (Accessed 10 01, 2019).
- Hock, R., Rasul, G., Adler, C., Cáceres, B., Gruber, S., Hirabayashi, Y., et al. (2019). "2019: High Mountain Areas," in *IPCC Special Report on the Ocean and Cryosphere in a Changing Climate*. Editors H.-O. Pörtner, D. C. Roberts, V. Masson-Delmotte, P. Zhai, M. Tignor, E. Poloczanska, et al. (Cambridge, United Kingdom: Cambridge University Press).
- Hoelzle, M., Barandun, M., Bolch, T., Fiddes, J., Gafurov, A., Muccione, V., et al. (2019). The Status and Role of the alpine Cryosphere in Central Asia, 100, 121. doi:10.4324/9780429436475-8
- Hori, M., Aoki, T., Tanikawa, T., Motoyoshi, H., Hachikubo, A., Sugiura, K., et al. (2006). In-situ Measured Spectral Directional Emissivity of Snow and Ice in the 8–14 μm Atmospheric Window. *Remote Sensing Environ.* 100, 486–502. doi:10.1016/j.rse.2005.11.001
- Huang, J. (2018). A Simple Accurate Formula for Calculating Saturation Vapor Pressure of Water and Ice. *AMETSO* 57, 1265–1272. doi:10.1175/JAMC-D-17-0334.1
- Immerzeel, W. W., Lutz, A. F., Andrade, M., Bahl, A., Biemans, H., Bolch, T., et al. (2019). Importance and Vulnerability of the World's Water Towers. *Nature* 577, 364–369. doi:10.1038/s41586-019-1822-y
- Küng, O., Strecha, C., Beyeler, A., Zufferey, J.-C., Floreano, D., Fuia, P., et al. (2011). The Accuracy of Automatic Photogrammetric Techniques on Ultra-light Uav Imagery. *Int. Arch. Photogramm. Remote Sens. Spat. Inf. Sci.* XXXVIII-1/C22, 125–130. doi:10.5194/isprsarchives-XXXVIII-1-C22-125-2011
- Labbal, V. (2000). *Traditional Oases of Ladakh: A Case Study of Equity in Water Management*. Oxford, UK: Oxford University Press, 163–183.
- Lowe, D. G. (2004). Distinctive Image Features from Scale-Invariant Keypoints. *Int. J. Comp. Vis.* 60, 91–110. doi:10.1023/B:VISL.0000029664.99615.94
- Meteoblue (2021). Climate Guttannen. Available at https://www.meteoblue.com/en/weather/historyclimate/climatemodelled/guttannen_switzerland_2660433 (Accessed 07 19, 2021).
- Mölg, N., and Bolch, T. (2017). Structure-from-motion Using Historical Aerial Images to Analyse Changes in Glacier Surface Elevation. *Remote Sensing* 9, 1021. doi:10.3390/rs9101021
- Mölg, T., and Hardy, D. R. (2004). Ablation and Associated Energy Balance of a Horizontal Glacier Surface on Kilimanjaro. *J. Geophys. Res.* 109, 1–13. doi:10.1029/2003JD004338
- Nüsser, M., Dame, J., Kraus, B., Baghel, R., and Schmidt, S. (2019a). Socio-hydrology of "artificial Glaciers" in Ladakh, India: Assessing Adaptive Strategies in a Changing Cryosphere. *Reg. Environ. Change* 19, 1327–1337. doi:10.1007/s10113-018-1372-0
- Nüsser, M., Dame, J., Parveen, S., Kraus, B., Baghel, R., and Schmidt, S. (2019b). Cryosphere-Fed Irrigation Networks in the Northwestern Himalaya: Precarious Livelihoods and Adaptation Strategies under the Impact of Climate Change. *Mountain Res. Dev.* 39. doi:10.1659/MRD-JOURNAL-D-18-00072.1
- Nüsser, M., Schmidt, S., and Dame, J. (2012). Irrigation and Development in the Upper Indus Basin: Characteristics and Recent Changes of a Socio-Hydrological System in Central Ladakh, India. *Mountain Res. Dev.* 32, 51–61. doi:10.1659/MRD-JOURNAL-D-11-00091.1
- Oerlemans, J., Balasubramanian, S., Clavuot, C., and Keller, F. (2021). Brief Communication: Growth and Decay of an Ice Stupa in alpine Conditions - a Simple Model Driven by Energy-Flux Observations over a Glacier Surface. *The Cryosphere* 15, 3007–3012. doi:10.5194/tc-15-3007-2021
- Oerlemans, J., and Knap, W. H. (1998). A 1 Year Record of Global Radiation and Albedo in the Ablation Zone of Morteratschgletscher, switzerland. *J. Glaciol.* 44, 231–238. doi:10.3189/S00221430000257410.1017/s002214300002574
- Sa, P. (2020). Pix4dMapper 4.1 User Manual. Available at <https://support.pix4d.com/hc/en-us/articles/204272989-Offline-Getting-Started-and-Manual-pdf> (Accessed 12 09, 2021).
- Scherrer, S. C. (2020). Temperature Monitoring in Mountain Regions Using Reanalyses. Lessons from the Alps. *Environ. Res. Lett.* 15, 044005. doi:10.1088/1748-9326/ab702d
- Schmidt, L. S., Ædalgeirsðóttir, G., Guðmundsson, S., Langen, P. L., Pálsson, F., Mottram, R., et al. (2017). The Importance of Accurate Glacier Albedo for Estimates of Surface Mass Balance on Vatnajökull: Evaluating the Surface Energy Budget in a Regional Climate Model with Automatic Weather Station Observations. *The Cryosphere* 11, 1665–1684. doi:10.5194/tc-11-1665-2017
- Schmidt, S., and Nüsser, M. (2012). Changes of High Altitude Glaciers from 1969 to 2010 in the Trans-himalayan Kang Yatze Massif, Ladakh, Northwest india. *Arctic, Antarctic, Alpine Res.* 44, 107–121. doi:10.1657/1938-4246-44.1.107
- Steiner, J. F., Pellicciotti, F., Buri, P., Miles, E. S., Immerzeel, W. W., and Reid, T. D. (2015). Modelling Ice-Cliff Backwasting on a Debris-Covered Glacier in the Nepalese Himalaya. *J. Glaciol.* 61, 889–907. doi:10.3189/2015JoG14J194
- Tennøe, S., Halnes, G., and Einevoll, G. T. (2018). Uncertainpy: A python Toolbox for Uncertainty Quantification and Sensitivity Analysis in Computational Neuroscience. *Front. Neuroinform.* 12, 49. doi:10.3389/fninf.2018.00049
- Thayyen, R. J., and Gergan, J. T. (2010). Role of Glaciers in Watershed Hydrology: a Preliminary Study of a "Himalayan Catchment". *The Cryosphere* 4, 115–128. doi:10.5194/tc-4-115-2010
- Turner, D., Lucieer, A., and Watson, C. (2012). An Automated Technique for Generating Georectified Mosaics from Ultra-high Resolution Unmanned Aerial Vehicle (Uav) Imagery, Based on Structure from Motion (Sfm) point Clouds. *Remote Sensing* 4, 1392–1410. doi:10.3390/rs4051392
- Unger-Shayesteh, K., Vorogushyn, S., Farinotti, D., Gafurov, A., Duethmann, D., Mandychev, A., et al. (2013). What Do We Know about Past Changes in the Water Cycle of central Asian Headwaters? a Review. *Glob. Planet. Change* 110, 4–25. doi:10.1016/j.gloplacha.2013.02.004
- Wangchuk, S. (2015b). Ice Stupa Artificial Glacier Inaugurated. Available at <http://icestupa.org/news/ice-stupa-artificial-glacier-inaugurated-5th-of-march> (Accessed 10 01, 2019).
- Wangchuk, S. (2014). Ice Stupa Artificial Glaciers of Ladakh. Available at http://www.indiegogo.com/projects/ice-stupa-artificial-glaciers-of-ladakh# (Accessed 10 01, 2019).
- Wangchuk, S. (2021). Ice Stupa Competition. Available at <https://tribal.nic.in/IceStupa.aspx> (Accessed 12 13, 2021).
- Wangchuk, S. (2015c). Ice Stupa Surpasses Guinness World Record. Available at <http://icestupa.org/news/ice-stupa-surpasses-guinness-world-record> (Accessed 10 01, 2019).
- Wangchuk, S. (2015d). Ice Stupa Way of Celebrating a Special Day. Available at <http://icestupa.org/news/ice-stupa-way-of-celebrating-a-special-day6th-of-june> (Accessed 10 01, 2019).
- Wangchuk, S. (2015a). The Good News at Ice Stupa. Available at <http://icestupa.org/news/the-good-news-at-ice-stupa> (Accessed 10 01, 2019).
- Wangchuk, S. (2015e). World Water Day at Ice Stupa. Available at <http://icestupa.org/news/world-water-day-at-ice-stupa> (Accessed 10 01, 2019).
- Woolf, H. M. (1968). *On the Computation of Solar Elevation Angles and the Determination of Sunrise and sunset Times*. Washington, DC: National Aeronautics and Space Administration. Available at <https://ntrs.nasa.gov/citations/19680025707> (Accessed April 01, 2022).
- Xiu, D., and Hesthaven, J. S. (2005). High-order Collocation Methods for Differential Equations with Random Inputs. *SIAM J. Sci. Comput.* 27, 1118–1139. doi:10.1137/040615201
- Zhou, S., Kang, S., Gao, T., and Zhang, G. (2010). Response of Zhadang Glacier Runoff in Nam Co basin, Tibet, to Changes in Air Temperature and Precipitation Form. *Chin. Sci. Bull.* 55, 2103–2110. doi:10.1007/s11434-010-3290-5
- Zolles, T., Maussion, F., Galos, S. P., Gurgiser, W., and Nicholson, L. (2019). Robust Uncertainty Assessment of the Spatio-Temporal Transferability of Glacier Mass and Energy Balance Models. *The Cryosphere* 13, 469–489. doi:10.5194/tc-13-469-2019
- Conflict of Interest:** The authors declare that the research was conducted in the absence of any commercial or financial relationships that could be construed as a potential conflict of interest.
- Publisher's Note:** All claims expressed in this article are solely those of the authors and do not necessarily represent those of their affiliated organizations, or those of the publisher, the editors and the reviewers. Any product that may be evaluated in this article, or claim that may be made by its manufacturer, is not guaranteed or endorsed by the publisher.
- Copyright © 2022 Balasubramanian, Hoelzle, Lehning, Bolibar, Wangchuk, Oerlemans and Keller. This is an open-access article distributed under the terms of the Creative Commons Attribution License (CC BY). The use, distribution or reproduction in other forums is permitted, provided the original author(s) and the copyright owner(s) are credited and that the original publication in this journal is cited, in accordance with accepted academic practice. No use, distribution or reproduction is permitted which does not comply with these terms.

7.2 Paper II

Improving water-use efficiency of artificial ice reservoirs (Icestupas) through weather-sensitive fountain scheduling strategies

Balasubramanian, S., Hoelzle, M., and Waser, R.

Frontiers in Earth Science 9 (February 23, 2022): 771342. doi:10.3389/feart.2021.771342.

Fountain scheduling strategies for improving water-use efficiency of artificial ice reservoirs (Ice stupas)

Suryanarayanan Balasubramanian^{1,2}, Martin Hoelzle¹, and Roger Waser³

¹University of Fribourg, Department of Geosciences, Fribourg, Switzerland

²Himalayan Institute of Alternatives, Ladakh, India

³University of Applied Sciences and Arts, Luzern, Switzerland

Correspondence: suryanarayanan.balasubramanian@unifr.ch

Abstract.

Artificial ice reservoirs (AIRs), also called ice stupas, are a climate-change adaptation strategy developed in the Indian Himalayas (Ladakh). With this technology, otherwise unused stream/spring water is stored in large ice towers during the winter. The surplus melt water generated in spring is used to satisfy irrigation water demands. Recent studies have shown that, during AIRs construction, over 75% of the water sprayed is lost. We examine whether fountain scheduling strategies can reduce this water loss by building two AIRs under identical weather conditions but with different fountain scheduling construction strategies. Fountain scheduling was performed through an automation system computing recommended discharge rates using real-time weather input and location metadata. Fountain operation using scheduling strategies produced similar ice volume while consuming one-tenth of the water the unscheduled fountain used. Simulations converting unscheduled fountains into scheduled fountains showed a threefold improvement in water-use efficiency. Overall, these results show that automated fountain water supply management can increase water-use efficiency of AIRs and reduce their maintenance without compromising their meltwater production.

1 Introduction

Cryosphere-fed irrigation networks in arid mountain regions are completely dependent on timely availability of meltwater from snow, glaciers, and permafrost (Immerzeel et al., 2020; Farhan et al., 2015; Tveiten, 2007). With the accelerated decline of glaciers due to climate change, these regions are experiencing seasonal water scarcity (Hoelzle et al., 2019; Xenarios et al., 2019; Barandun et al., 2020), which limits the output and duration of agricultural activities.

In Ladakh, a cold arid desert in northern India, a typical shortage of water occurs at the onset of the agricultural season (April and May) until a sufficient and reliable supply of meltwater from glaciers becomes available (Norphel and Tashi, 2015; Nüsser and Baghel, 2016; Vincent, 2009).

To cope with this recurrent water scarcity, villagers have developed artificial ice reservoirs (AIRs; Fig. 1a). AIRs capture water during autumn and winter, freezing and holding it until spring, when this water melts and flows down to irrigate the fields (IPCC, 2019; Vince, 2009; Clouse et al., 2017; Nüsser et al., 2019); thus retaining a previously unused portion of the annual flow and facilitating its use to compensate the decreased flow during the following spring.

25 A spirit of improvisation guides the construction strategy of AIRs, challenging their classification. Construction strategies using fountain systems form AIRs which tend towards a conical shape, whereas those strategies without fountain systems form flat sheets of ice. Therefore, in the present study, we classify AIRs based on whether or not these use fountain systems. AIRs using fountain systems are called ice stupas (Fig. 1c) and those without are called ice terraces (Fig. 1b), according to the resulting shape of the respective AIRs. In the present work, we investigate the ice stupa form of AIRs.

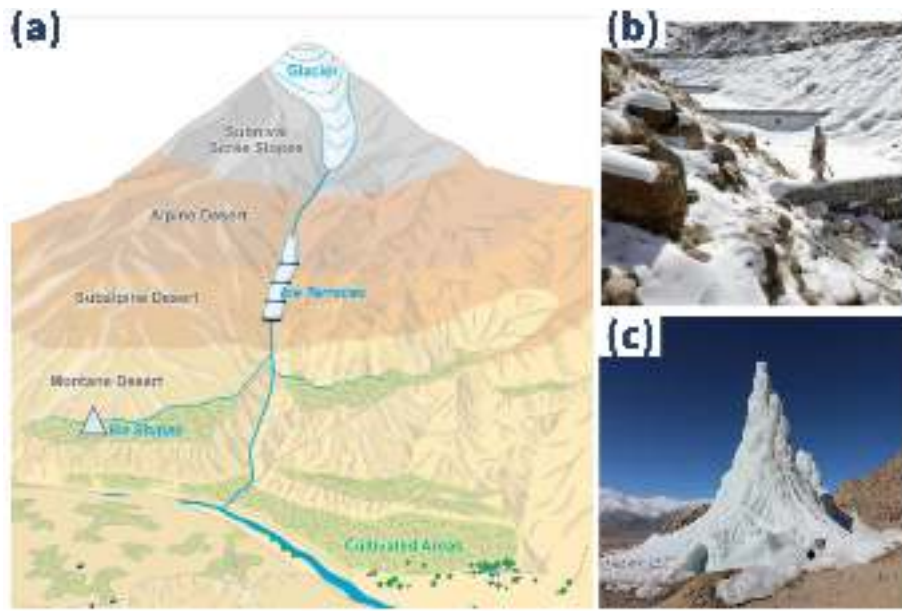


Figure 1. (a) Schematic overview of artificial ice reservoirs (AIRs) located at altitudes between the glaciers and the irrigation networks in the cultivated areas; (b) ice terraces and (c) ice stupas are located at higher and lower altitudes, respectively. Adapted from: Nüsser and Baghel (2016)

30 Over the past decade, several ice stupas have been built to supplement the irrigation water supply of mountain villages in India (Wangchuk, 2020; Palmer, 2022; Aggarwal et al., 2021), Kyrgyzstan (BBC News, 2020), and Chile (Reuters, 2021). These AIRs are traditionally constructed by diverting springs or glacial streams into fountain spray systems via embankments and pipelines.

35 A common issue of AIR construction systems is fountain scheduling, namely answering the questions “when to spray?,” “how much?,” and “for how long?.” Starting a fountain spray too early, spraying too much water, or running a fountain spray for too long might lead to overwatering; at the very least, this practice wastes water. Similarly, starting the fountain spray too late, spraying too little water, or not running the system for long enough might lead to underwatering and can cause reduced ice volume or freeze the water supply pipelines.

40 Previous work (Balasubramanian et al., 2022) has shown that traditional construction systems suffer from overwatering. To avoid this issue, we need to understand surface freezing rates, which can be calculated by means of the full energy balance model developed in Balasubramanian et al. (2022). This model requires an accurate estimation of fountain spray radius to pro-

duce recommended discharge rates. In theory, we can estimate this by modelling the projectile motion of water droplets using fountain characteristics such as aperture diameter and discharge rate. In practice, this estimation depends also on the relative importance of wind-driven redistribution effects. Therefore, estimating fountain spray radius requires a better understanding of
45 the relative contribution of these two processes.

Other practical issues need to be addressed before dealing with fountain scheduling processes: for example, in Indian AIRs, the fountain discharge rate could theoretically be halved since this is always twice as high as the modelled freezing rate (Balasubramanian et al., 2022). However, in practice, a reduction of the discharge rate could increase the maintenance cost due to a higher risk of freezing events in the fountain pipeline.

50 An optimum construction strategy, therefore, should first prevent the occurrence of freezing events in the fountain pipeline. These events can be prevented by setting a minimum threshold for the recommended discharge rate. Additionally, discharge rates recommended need to be sensitive to constraints on water supply or weather conditions at the construction site; for example, locations limited by their water supply such as Ladakh, India would prioritize water-use efficiency, whereas those limited by the duration of their favorable weather windows such as Guttannen, Switzerland would prioritize maximum ice
55 volume. Accordingly, we use two types of model parameter optimization that prevent underwatering and overwatering to attain higher ice volume and higher water-use efficiency, respectively.

Adjusting fountain discharge rates manually is not practical due to two reasons: first, this would involve constant adjustments of discharge rates in response to significant diurnal and seasonal variations of freezing rates; second, frequent pipeline water drainage would be required to avoid water losses. Therefore, the operation of scheduled fountains via automation systems is
60 preferred to reduce long-term maintenance costs.

The present study aims to compare water-use efficiency, maximum ice volume, and maintenance effort between traditional and automated construction strategies. First, two AIRs were built in the same location with and without automated fountain scheduling strategies; both were measured and compared. In a second step, differences in construction strategies between Indian and Swiss AIRs studied in previous winters were quantified using model simulations.

65 2 Study sites and data

In the present work, we use datasets from our previous work (Balasubramanian et al., 2022) along with new datasets. These old datasets record the meteorological conditions and fountain characteristics of AIRs built in Gangotri, India (IN21) and Guttannen, Switzerland (CH21) during the winter of 2020–21. The new AIR datasets were collected in Guttannen, Switzerland during the winter of 2021–22 (CH22).

70 The Guttannen site (46.66°N , 8.29°E) is situated in the Berne region, Switzerland at an altitude of 1047 m a.s.l . During the winter (Oct-Apr), mean daily minimum and maximum air temperatures vary between -13 and 15°C . Clear skies are rare, averaging around 7 days during winter. Daily winter precipitation can sometimes be as high as 100 mm . These values are based on 30 years of hourly historical weather data measurements (Meteoblue, 2021). Two AIRs were constructed by the Guttannen

Bewegt Association, the University of Fribourg, and the Lucerne University of Applied Sciences and Arts during the winter of
75 2021–22 using a traditional and an automated construction strategy.



Figure 2. Unscheduled and scheduled fountains used for construction of traditional and automated AIRs at Guttannen. Picture credits: Daniel Bürki

The automated and traditional AIRs were constructed adjacent to each other with different fountain designs, as shown in Fig. 2. This ensures both AIRs share water source and identical weather conditions. In addition, a webcam guaranteed continuous surveillance of the automated AIR.

In the AIR constructed with the traditional strategy, tree branches were laid covering the fountain pipe to initiate and accelerate the ice cone formation process. In the AIR constructed with an automated strategy, only the fountain pipe was placed before the water spray started. Construction of both AIRs began on December 8, 2021 (start date) on a 13-cm-thick snow bed and ended on April 12, 2022 (expiry date).

In the traditional AIR, the fountain was operated manually, whereas in the automated AIR, the fountain discharge rate was controlled using real-time weather input and several control parameters which could be modified via a user interface.
85 Henceforth, we refer to the fountain used in the traditional AIR as unscheduled fountain and to the fountain used in the automated AIR as scheduled fountain.

2.1 Meteorological data

To calculate the surface energy balance of an AIR, the following variables are required: air temperature, relative humidity, wind speed, pressure, precipitation, incoming longwave radiation, shortwave radiation, and cloudiness index. Our primary

90 weather data source is an automatic weather station (AWS) located within 20 m from the AIRs. Hourly ground temperature measurements were also recorded by the AWS to obtain approximate values of the fountain water temperature. Less than 0.4 % of data was missing, and data gaps were filled by linear interpolation. However, two additional datasets were used to obtain all the necessary input variables, namely cloudiness index and precipitation. These two datasets were obtained from ERA5 reanalysis dataset (Hersbach et al., 2020) and a MeteoSwiss AWS located 184 m from the AIRs (Station ID: 0-0756-0-GTT).

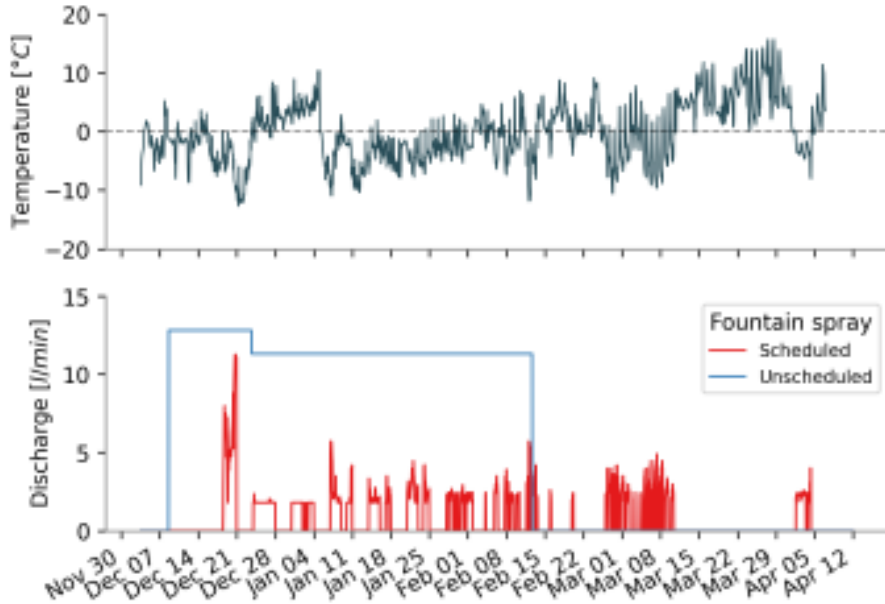


Figure 3. Temperature and discharge measurements of the two fountains at the Guttannen construction site.

95 2.2 Fountain observations

The scheduled and unscheduled fountains present the following attributes: discharge rate (Q), height (h), water temperature (T_F), nozzle pressure loss (P_{nozzle}), and the spray radius (r). Discharge rate represents the discharge rate of water in the fountain pipeline. Height denotes the height of the fountain pipeline installed. Fountain water temperature is the temperature of water droplets produced by the fountain. The nozzle pressure loss denotes the pressure consumed during the formation of 100 water droplets. Spray radius denotes the observed ice radius formed from the fountain water droplets.

Height was increased in steps of 1 m for both fountains. For the scheduled fountain, the initial height was 3 m and was increased to 4 m on December 23. For the unscheduled fountain, the initial height was 3.7 m and was increased twice—December 23 and February 12.

Figure 3 shows the temporal variation in temperature and discharge rate for both the scheduled and unscheduled fountains. 105 The unscheduled fountain showed variations in discharge rate whenever the fountain height was increased. The discharge rate variations of the scheduled fountain were caused by the control valve of the automation system. The control ball valve position

between 0 and 100 % (or 0 to 90 °) was regulated based on real-time meteorological conditions. Throughout the study period, the control valve was opened completely (100 %) only once, corresponding to the moment in time when temperature attained its minimum of -13°C on December 20. The control valve was never opened beyond 34 % thereafter.

110 The unscheduled fountain was manually operated to spray all the available discharge until a fountain freezing event interrupted the discharge on February 17. Unfortunately, no discharge rate measurements were recorded for the unscheduled fountain. However, the unscheduled fountain presented a higher discharge rate compared with the scheduled fountain due to its higher aperture area (Fig. 2). Therefore, we conservatively assume the discharge rate of the unscheduled fountain to be equal to the maximum discharge rate of the scheduled fountain, which was observed to be 13 l/min and 11 l/min at a fountain height
115 of 3 m and 4 m, respectively.

Water temperature of both fountains was estimated from the AWS ground temperature dataset obtained with a thermistor located 0.3 m below the base of the scheduled fountain.

2.3 Drone surveys

Several photogrammetric surveys were conducted on the traditional and the automated AIRs. The digital elevation models
120 (DEMs) generated from the obtained imagery were analysed to document ice radius, surface area, and volume of the ice structures. Ice radius measurements from drone flights showed either an increase in AIR circumference or volume and were averaged to determine the fountain spray radius. The number of drone surveys conducted for the traditional and the automated AIRs was 8 and 6, respectively (Table 1). We attach a high uncertainty of $\pm 10\%$ for all AIR observations to accommodate for the uncertainties in the drone processing methodology described in the supplementary materials of Balasubramanian et al.
125 (2022).

3 Methods

3.1 Fountain scheduling software

Recommended discharge rates can be produced only when information about AIR surface properties and weather conditions is available. In particular, resolving the uncertainty in the expected freezing rate requires quantification of slope, albedo, and
130 cloudiness. However, these properties cannot be predicted, and therefore, we associate the upper and lower bound of each variable to a different model depending on whether these increase the freezing rate or not. Higher albedo and slope values decrease the shortwave radiation impact. Higher cloudiness values increase both the shortwave and the longwave radiation impact. The model overestimating the freezing rate is hereinafter referred as ice volume optimized model (IVOM) and the model underestimating the freezing rate, water-use efficiency optimized model (WEOM). Accordingly, the values assigned for
135 all three variables in each model are presented in Table 2.

The discharge scheduling software implements two types of fountain scheduling strategies depending on which model type is suitable. The WEOM model type is used when the location presents limited water quantity, as this is expected to produce

Table 1. Summary of drone surveys

	No.	Date	Volume	Radius	Surface area
Traditional	1	Dec 23, 2021	17 m ³	2.9 m	47 m ²
	2	Jan 3, 2022	22 m ³	3.4 m	61 m ²
	3	Jan 22, 2022	35 m ³	4 m	79 m ²
	4	Feb 6, 2022	44 m ³	4.2 m	86 m ²
	5	Feb 20, 2022	43 m ³	4.3 m	86 m ²
	6	Mar 19, 2022	33 m ³	4.4 m	84 m ²
	7	Mar 26, 2022	24 m ³	4.3 m	74 m ²
	8	Apr 12, 2022	11 m ³	3.5 m	50 m ²
Automated	1	Dec 23, 2021	35 m ³	4.3 m	73 m ²
	2	Jan 3, 2022	32 m ³	4.4 m	81 m ²
	3	Feb 20, 2022	60 m ³	5.3 m	105 m ²
	4	Mar 19, 2022	28 m ³	3.7 m	57 m ²
	5	Mar 26, 2022	19 m ³	3.7 m	53 m ²
	6	Apr 12, 2022	7 m ³	2.5 m	53 m ²

better water-use efficiency. The IVOM model type is used when the location presents limited duration of favorable weather windows, as this is expected to produce higher ice volume. These two types of scheduled fountains are hereafter referred as
140 water-sensitive fountain and weather-sensitive fountain, respectively.

Table 2. Assumptions for the parametrization introduced to simplify the ice volume optimized model (IVOM) and the water-use efficiency optimized model (WEOM). $\alpha_{snow/ice}$ represents albedo of snow or ice.

Estimation of	Symbol	IVOM	WEOM
Slope	s_{cone}	1	0
Albedo	α	α_{snow}	α_{ice}
Cloudiness	cld	0	1

We apply the assumptions described in Table 2 on the one-dimensional description of energy fluxes as used in Balasubramanian et al. (2022) to obtain the rate of change of AIR ice mass as follows:

$$\frac{\Delta M_{ice}}{\Delta t} = \left(\frac{q_{SW} + q_{LW} + q_S + q_F + q_R + q_G - q_T}{L_F} + \frac{q_L}{L_V} \right) \cdot A_{cone} \quad (1)$$

Upward and downward fluxes relative to the ice surface are positive and negative, respectively. The first term represents the
145 mass change rate due to freezing of the fountain water and melting of the ice. q_{SW} is the net shortwave radiation; q_{LW} is the net longwave radiation; q_L and q_S are the turbulent latent and sensible heat fluxes, respectively; q_F is the fountain discharge heat flux; q_R is the rain water heat flux; q_G is the ground heat flux; q_T is the temperature heat flux, and A_{cone} is the area of the AIR surface. L_F and L_V represent latent heat of fusion and vaporization, respectively. The derivation of these individual terms for the IVOM and WEOM model versions are discussed in Appendix A.

150 Equation 1 is implemented in the automation software. The user interface of the software enables input of the spray radius, altitude, latitude, and longitude of the construction location. The automation hardware consists of an AWS, flowmeter, control valve, drain valves, air valves, fountain, pipeline, and a logger. The logger feeds the AWS data to the automation software and informs of the recommended discharge rate to the flowmeter. The flowmeter adjusts the control valve to match the recommendation. In case a termination criterion gets met, the drain and air valves allow removal of water and entry of air in the pipeline,
155 respectively.

The recommended discharge rate is equal to the mass change rate. However, certain termination criteria listed below override the discharge rate recommendation and drain the pipeline to prevent water loss or fountain freezing events:

- High water loss is assumed when wind speed is greater than user-defined critical wind speed.
- High risk of fountain freezing is assumed when mass change rate is lower than user-defined minimum fountain discharge rate.
- Freezing events in fountain pipeline are assumed when measured discharge rate equals zero for at least 20 seconds.
- Pipeline leakage is assumed when measured discharge rate is greater than user-defined maximum fountain discharge rate.

4 Modelling fountain spray radius

165 Fountain spray radius is defined as the largest horizontal distance covered by fountain water droplets. This can be determined by modelling the trajectory of these droplets using the projectile motion equation. This projectile motion starts at the fountain nozzle and ends at the AIR surface. To obtain the droplets speed (v), we use the measured aperture diameter ($dia = 0.001m$) and discharge rate of the scheduled fountain with the following equation:

$$v = \frac{4 \cdot Q}{60 \cdot 1000 \cdot \pi \cdot dia^2} \quad (2)$$

170 where v is the droplet speed in m/s and Q is the discharge rate of the fountain in l/min .

To obtain the spray radius (r), we use the optimum launch angle $\theta = 45^\circ$ in the projectile motion equation to get:

$$r = \frac{v \cdot (v + \sqrt{v^2 + 4hg})}{2g} \quad (3)$$

The influence of wind-driven redistribution can be included in the spray radius by multiplying wind speed by time of flight of water droplets.

175 5 Determination of pressure losses

The fountain pipeline system delivering water to the ice stupa suffers several pressure losses, which limit the maximum height that the fountain can achieve. These lossses can be (a) altitudinal (P_{alt}), (b) frictional ($P_{friction}$), and (c) nozzle (P_{nozzle}) losses. The altitudinal losses depend on the altitude difference between the source and the fountain. The frictional losses are proportional to the length of the pipeline and inversely proportional to their diameter. The nozzle losses depend on the 180 engineering design of the fountain nozzle.

Pressure losses can be determined using the Bernoulli equation as follows:

$$P_{source} = P_{alt} + P_{friction} + P_{nozzle} + \frac{\rho \cdot v^2}{2} \cdot 10^{-5} \quad (4)$$

where P_{source} is the source pressure, P_{nozzle} is the pressure loss due to the fountain nozzle, and P_{alt} is the pressure loss due to the altitudinal difference between the pipeline input and fountain output. These pressure variables are measured in bars. 185 The speed v can be determined from discharge rate observations using Eq. 2.

The frictional loss of the pipeline used in the experiment can be determined using the Hagen–Poiseuille equation (Poiseuille, 1847):

$$P_{friction} = \frac{3.2 \cdot \mu \cdot v \cdot L}{\rho \cdot g \cdot dia^2} \quad (5)$$

where $P_{friction}$ is in bars, L is the total length of the pipeline measured in meters, and v is the water speed in m/s . Note 190 that the above equation only applies for laminar flow, the one investigated in the present work.

5.1 Model updates

In the present study, we focus on the integration of fountain scheduling processes with the AIR model (Balasubramanian et al., 2022). For details on model internals and calculation of surface processes, we refer to the respective literature references.

In the previous version of the model (Balasubramanian et al., 2022), fountain water temperature (T_F) was estimated as a 195 constant parameter. However, in reality, this is a poor approximation because it does not account for two processes, namely temperature fluctuations during transit from the source to the fountain nozzle or temperature fluctuations during the flight time of water droplets after leaving the fountain nozzle. Therefore, we use hourly measured ground temperature values to approximate the first process and we assume that water temperature cools down to $0^\circ C$ during subzero air temperature conditions to approximate the second process.

200 In the previous version of the model (Balasubramanian et al., 2022), fountain discharge events were reset from surface albedo to ice albedo. However, this assumption limits the accuracy of the model, especially for the automated AIR, where

several fountain discharge events of short duration occur. Therefore, we assume that discharge events reduce the albedo decay rate (τ) by a factor of $\frac{\alpha_{ice}}{\alpha_{snow}}$.

Additionally, both AIRs experienced numerous precipitation events. Therefore, instead of assuming AIR density (ρ_{cone}) to 205 be equal to ice density—which was no longer accurate—we parameterized AIR density ρ_{cone} as follows:

$$\rho_{cone} = \frac{M_F + M_{dep} + M_{ppt}}{(M_F + M_{dep})/\rho_{ice} + M_{ppt}/\rho_{snow}} \quad (6)$$

where M_F is the cumulative mass of the fountain discharge, M_{ppt} is the cumulative precipitation, M_{dep} is the cumulative accumulation through water vapour deposition, ρ_{ice} is the ice density (917 kg m^{-3}), and ρ_{snow} is the density of wet snow (300 kg m^{-3}) taken from Cuffey and Paterson (2010).

210 Rain events were not considered in the previous version of the model, but these occurred in our experiment. The influence of rain events on the albedo and the energy balance was assumed to be similar to the discharge events. However, the water temperature of a rain event was assumed to be equal to the air temperature; accordingly, the rain water heat flux (q_R) generated due to a rain event was equal to:

$$q_R = \frac{\Delta M_{ppt} \cdot c_{water} \cdot T_a}{\Delta t \cdot A_{cone}} \quad (7)$$

215 where M_{ppt} is the hourly precipitation in meters, c_{water} is the specific heat of water, and A_{cone} is the surface area.

5.2 Calibration

The model parameters were calibrated to the mean values of the ranges presented in Appendix Table A1. However, the surface layer thickness parameter was calibrated to a value of 0.09 m for the automated AIR instead of the default value of 0.05 m . This calibration was necessary to prevent hourly surface temperature fluctuations from assuming unphysical values above 220 40°C .

We performed the validation of the model for the traditional and automated AIRs by evaluating the root mean squared error (RMSE) between volume estimates and measurements.

Performance of the IVOM and WEOM versions of the physical model were assessed by comparing the correlation of its discharge rate estimates with the validated freezing rates of the traditional AIR.

225 6 Results

6.1 Model validation

The volume estimation for the automated and traditional AIRs showed an RMSE of 8 m^3 and 6 m^3 , respectively, with the drone volume observations. These are within 13 % and 11 % of the maximum volume of the automated and the traditional AIR, respectively. The estimated and measured AIR volumes are shown in Fig. 4.

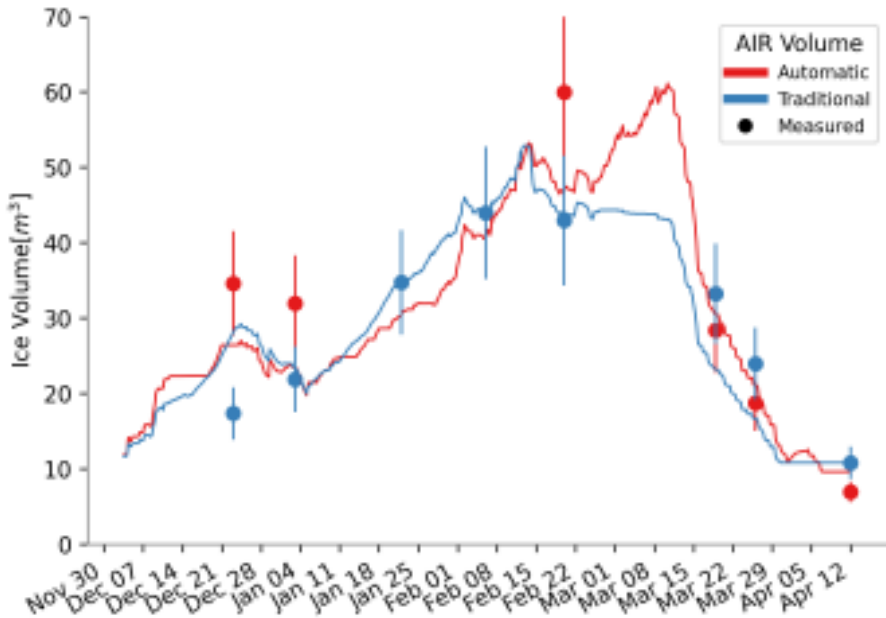


Figure 4. Volume validation of the scheduled and unscheduled fountain construction strategies.

230 6.2 Comparison of AIR construction strategies

Table 3 presents the influence of the two different fountain scheduling strategies in the mass and energy balance of their respective AIRs. The overall impact of the radiation fluxes—longwave and shortwave—and the turbulent fluxes—sensible and latent—on the freezing and melting energies is determined by their energy turnover, which is calculated as the sum of energy fluxes in absolute values (Table 3).

235 Fountain scheduling reduced the fountain discharge input and fountain wastewater output by an order of magnitude. However, this does not result in an appreciable difference in the volume evolution of the automated or traditional AIR, as shown in Fig. 4. This is due to two counteracting surface processes during fountain spray: process A consists in the dampening of albedo to ice albedo and process B consists in the absorption of heat energy from the fountain water droplets. The temporal variation of the magnitude of these processes is shown in Fig. 5.

240 A considerable difference exists in the contribution of the shortwave radiation due to process A. Although the unscheduled fountain was active for a longer duration, frequent snowfall events counteracted the albedo feedback of the fountain discharge. In contrast, the albedo of the automated AIR was reduced by late fountain spray events, in particular in March and April, as shown in Fig. 5. These poorly timed fountain spray events occurred because of the global solar radiation diurnal variation, since these were calibrated based on values for February in the automation system. Therefore, poor calibration of the automation 245 system resulted in an increased impact of shortwave radiation on the automated AIR. Similarly, the fountain discharge heat flux for the traditional AIR was enhanced due to process B. The higher discharge value of the unscheduled fountain and its longer

Table 3. Summary of the mass balance, energy balance, and fountain and AIR characteristics estimated at the end of the respective simulation duration for the automated and the traditional AIRs

	Name	Symbol	Traditional	Automated	Units
Input	Fountain discharge	M_F	1.1×10^6	1.5×10^5	kg
	Snowfall	M_{ppt}	9.2×10^3	1.4×10^4	kg
	Deposition	M_{dep}	4.0×10^2	4.5×10^2	kg
Output	Meltwater	M_{water}	4.5×10^4	5.4×10^4	kg
	Ice	M_{ice}	7.4×10^3	6.1×10^3	kg
	Sublimation	M_{sub}	3.7×10^3	4.5×10^3	kg
	Fountain wastewater	M_{waste}	1.07×10^6	1.0×10^5	kg
Energy flux	Shortwave radiation	q_{SW}	14	21	%
	Longwave radiation	q_{LW}	25	25	%
	Sensible heat	q_S	38	33	%
	Latent heat	q_L	19	19	%
	Fountain discharge heat	q_F	4	0	%
	Rain heat	q_R	0	0	%
	Ground heat	q_G	1	1	%
AIR	Maximum AIR volume		53	61	m^3
	Water-use efficiency		4	35	%

duration are responsible for the higher contribution of fountain discharge heat flux in the overall energy turnover. Therefore, higher melt of the automated AIR due to process A counteracted the higher melt of the traditional AIR due to process B.

6.3 Benefits of scheduling fountains

250 The difference in water-use efficiency and maximum ice volume between unscheduled and scheduled fountains in the Indian and Swiss locations across two winters is shown in Fig. 6a. Four experimental values (highlighted in circles) and five simulated values (highlighted in squares) are shown together. The experimental values were taken from the IN21 and CH21 AIRs studied in Balasubramanian et al. (2022) and the CH22 AIR investigated in the present work.

255 The water-use efficiency of all the unscheduled fountains is below 20 %. In general, water-use efficiency exhibits a threefold increase when the weather- or water-sensitive fountains are used in both locations.

For the Indian location, the three different kinds of fountains yielded significantly different results owing to discharge duration and max discharge rate (Fig. 6b). The unscheduled fountain showed a max discharge rate more than twice that of the scheduled fountains, resulting in higher water loss; freezing events in its pipeline caused frequent interruptions in the unscheduled discharge rate (Fig. 6b). In contrast, the mean freezing rates of the other two fountains during these events were

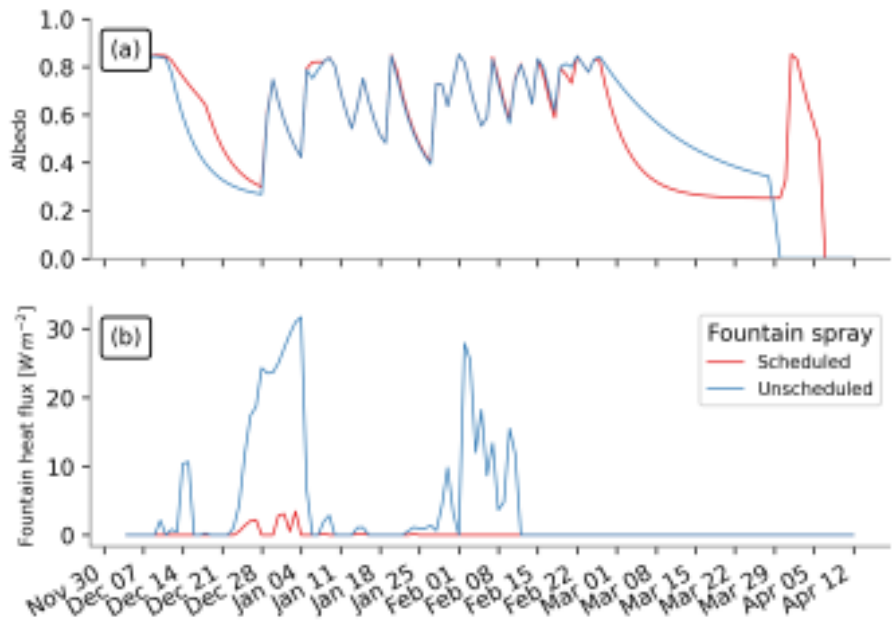


Figure 5. (a) Surface albedo and (b) fountain discharge heat flux showed significant variations between the two AIRs due to differences in their discharge rates.

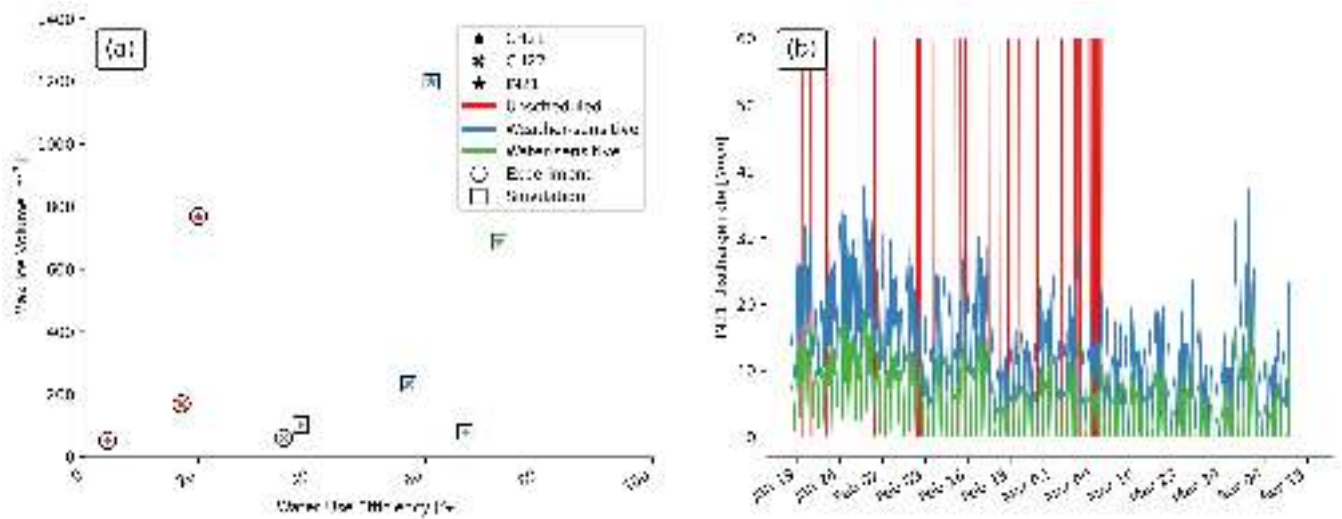


Figure 6. (a) The maximum volume and water-use efficiency estimated for AIRs constructed in different locations (represented by symbols) with different fountain scheduling strategies (represented by colours). Experimental values are highlighted in circles and simulated values are highlighted in squares. (b) Comparison of the unscheduled and scheduled fountain discharge rates at the IN21 location.

260 above their median values. This is because very cold temperatures freeze the water inside rather than outside the fountain system, instigating these freezing events in the fountain pipeline. Therefore, the discharge duration of the unscheduled fountain was much lower, resulting in lower ice volume. The water-sensitive fountain underestimated the freezing rate during the construction period and therefore produced much lower ice volume compared with the weather-sensitive fountain.

265 For the Swiss locations, scheduled fountains yielded better water-use efficiency but did not significantly alter the maximum volume obtained.

6.4 Performance of weather- and water-sensitive fountains

The WEOM and IVOM model versions estimated the freezing rate of the unscheduled fountain with an RMSE less than 0.8 l/min and 1.8 l/min , respectively, and a correlation of 0.4. The discharge rate values of the weather-sensitive fountain overestimated the freezing rate 93 % of the fountain spray duration, whereas those of the water-sensitive fountain overestimated 270 the freezing rate 70 % of the unscheduled fountain spray duration, as illustrated by Fig. 7. Therefore, the IVOM model version was successful in prioritizing the maximum ice volume by overestimating the discharge rates, but the WEOM model version could not sufficiently underestimate its discharge rate values to optimize water-use efficiency.

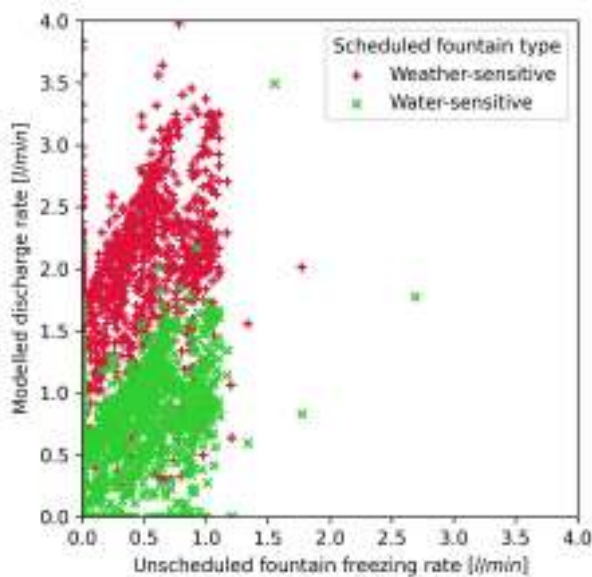


Figure 7. Comparison of the freezing rate estimated for the unscheduled fountain and the discharge rate of the scheduled fountains.

However, for the Indian location, significant magnitude differences can be observed among the three kinds of fountains. The modelled weather- and water-sensitive discharge rate values were a factor of two and three smaller, respectively, than the 275 measured unscheduled discharge rate (Fig. 6b).

6.5 Pressure losses

Table 4. Pipeline configuration of the automated ice stupa.

Name	Symbol	Value
Pipeline diameter	dia	16 mm
Pipeline length	L	66 m
Source water pressure	P_{source}	6 bar
Altitudinal pressure head	P_{alt}	1.1 bar
Water viscosity	μ	0.00152 Pas

Pressure consumption across the fountain pipeline provides insights into how the fountain pipeline configuration can be better optimized. The pipeline configuration of the automated ice stupa fountain is presented in Table 4. Maximum frictional loss occurs during maximum discharge, which was measured to be 11 l/min . By substituting the corresponding values in Eq. 280 5, we get $P_{friction}$ to be 0.3 bar. The speed v can be determined from our discharge rate observation from Eq. 3. Therefore, from Eq. 4, we get P_{nozzle} to be 4.6 bar, which represents more than 75 % of the source water pressure. Most of the input pressure was used by the fountain nozzle to generate water droplets.

6.6 Influence of wind-driven redistribution on fountain spray radius

The estimated volume changes over the month of January of the Swiss AIRs built in the winter of 2021–22 is less than half 285 that of the AIRs from the previous winter (CH21). This difference cannot respond to warmer temperatures during the CH22 winter, as the median January temperature of CH22 winter was colder than that of the CH21 winter (Fig. 8a). Moreover, the volume growth of CH20 AIR is 6 times that of the CH22 AIR, despite CH20 winter being 3 °C warmer.

We suspect the primary driver of volume difference across different winters to be the spray radius (Fig. 8b). However, this 290 observation contradicts our expectation that AIRs using the same water source and fountain designs would present similar spray radius. Moreover, manual measurements of the fountain spray radius were lower than the drone observations of the ice radius. These two observations imply that wind drift of water droplets could play a major role in temporal fluctuations of ice radius.

To validate this hypothesis, we modelled the projectile motion of scheduled fountain water droplets with wind speed values taken from CH22 and CH21 experiments. Figure 9 shows the modelled spray radius produced using these two wind datasets 295 and compares them with the measured spray radius values. As illustrated, wind speed drives the temporal variation in the spray radius. Moreover, the spray radius of the scheduled fountain is much higher with CH22 wind values than with those of CH21. Therefore, the determination of the fountain spray radius cannot be performed using the characteristics of the fountain nozzle alone, as this is significantly influenced by the temporal variation of the wind speed.

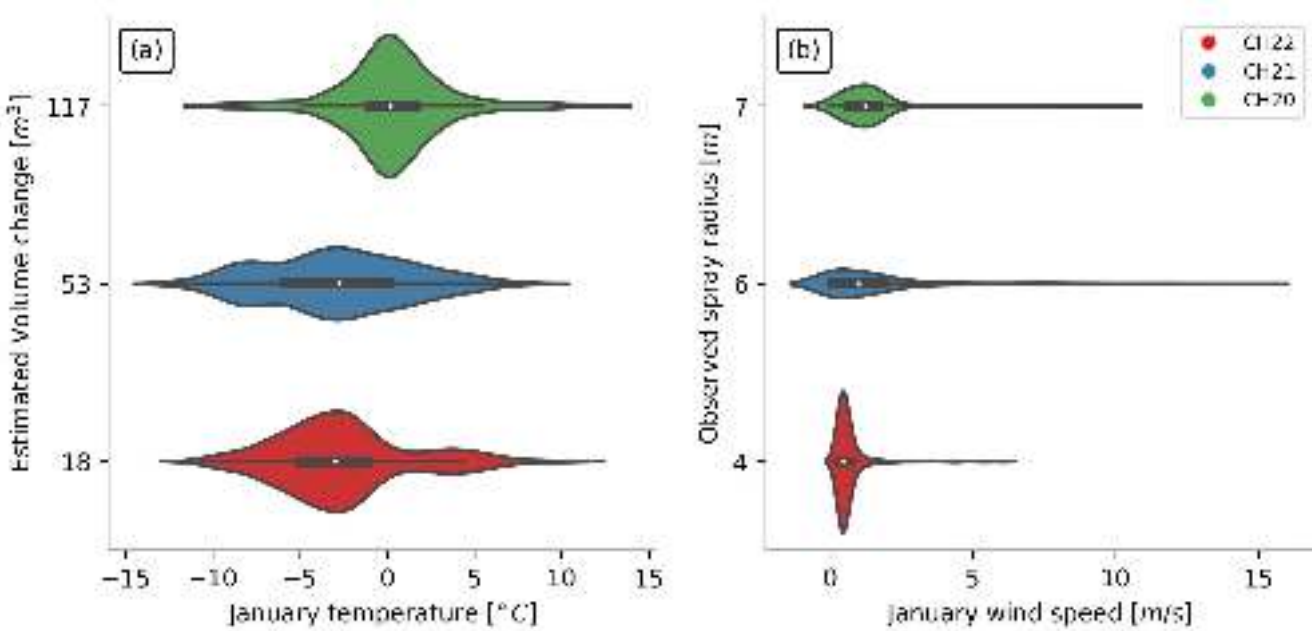


Figure 8. (a) Estimated volume change and temperature. (b) Observed spray radius and wind speed during January for AIRs built across three winters.

7 Discussion

300 7.1 Implementation of automated construction strategy

Our strategy is not yet suitable for direct application in current AIR construction sites due to the cost of the automation system. However, we believe sufficient cost reduction is possible through simpler automation systems which control only the duration of fountain spray and not their quantity.

Despite the cost, implementation can be reasonable if multiple stupas are constructed simultaneously. In the Guttannen site, 305 for example, eight identical ice stupas could have been constructed using the water supply of just one traditional ice stupa, thereby increasing eight times the melt water supply.

7.2 The state of AIR technology

The present study shows one strategy that can improve the water-use efficiency of AIRs. We chose this strategy because it 310 enables the use the AIR model in a simple and effective manner. Ice stupa construction can significantly be improved with sufficient engineering expertise. The fountain nozzle design is crucial for increasing the ice volume obtained. However, no methodology currently exists to rank the several fountain nozzles used for construction. An ideal pipeline configuration could make this technology cheaper and maintenance free. However, optimization of the pipeline material and diameters is yet

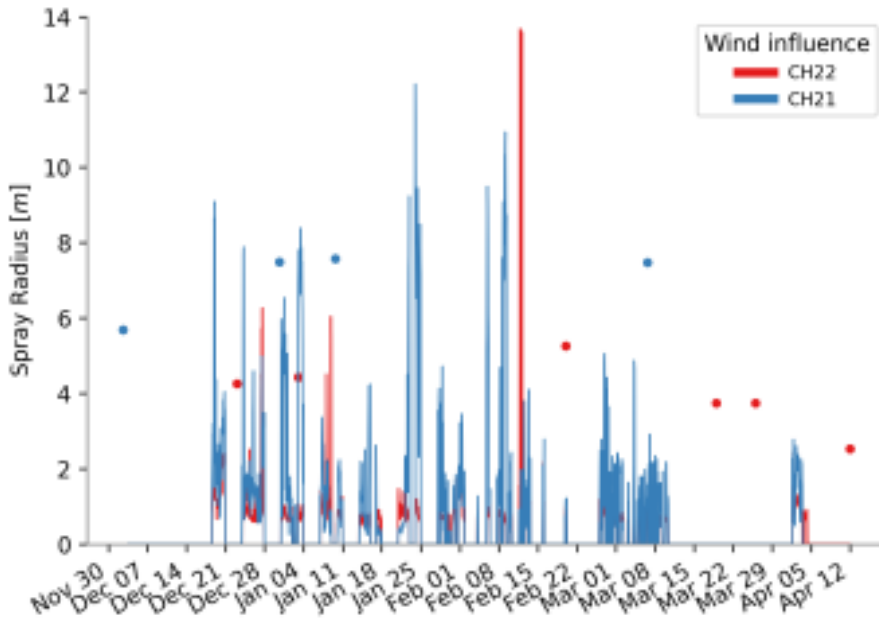


Figure 9. Modelled spray radius using wind values from CH22 and CH21 experiments. Measured spray radius values are indicated as dots.

to be performed—despite the time lost on pipeline freezing events and the potential cost reduction with cheaper pipeline materials and sizes. Therefore, we strongly encourage the engineering community to get involved and push the limits of the

315 cost-effectiveness, size, and survival duration of artificial ice reservoirs.

7.3 Additional water losses

A portion of the water volume exiting the fountains does not reach the ground due to both thermodynamic—evaporation and sublimation—and mechanical—wind-driven redistribution—effects. Although these water losses can be significant (Hanzer et al., 2020), their simulation with physical formulation is challenging because this is sensitive to the diameter of the water

320 droplets produced by the fountain.

8 Conclusions

We compare an automated AIR construction strategy with a traditional one using data collected in Guttannen, Switzerland and Gangles, India.

The main purpose of the present study is to quantify the influence of different fountain scheduling strategies on the water-
325 use efficiency and ice volume of AIRs exposed to identical weather conditions. We found that overwatering by unscheduled fountains not only increased the fountain wastewater production but also enhanced the melting rate of AIRs, mainly due to

surface albedo and fountain heat flux feedbacks. Scheduled fountains, in contrast, consumed only 13 % of the unscheduled fountain water supply. However, volume evolution of both AIRs showed no significant variations.

Two different model forcing strategies were used to recommend two types of scheduled discharge rates: limited weather windows to favor higher ice volume and water supply to favor water-use efficiency. These model versions were able to capture more than 44 % of the freezing rate variations of the traditional AIR. Simulations converting several unscheduled fountains to scheduled ones showed that at least a threefold increase in water-use efficiency is possible without compromising meltwater production.

The influence of wind-driven redistribution on the spray radius resulted in AIRs 6 times bigger despite 3 °C warmer temperatures. This implies that higher wind speed caused the volume differences in the AIRs constructed at the Swiss location through three consecutive winters. However, higher wind speed can also cause water losses if water droplets are distributed beyond the spray radius. Therefore, a critical wind speed needs to be determined to force wind-driven redistribution to increase spray radius instead of water losses. Future selection of construction locations and design of automation algorithms need to capitalize on wind-driven redistribution effects to further increase water-use efficiency.

Fountain nozzles play an important role in the construction process. First, these consume most of the input water pressure to form water droplets. Second, their engineering design determines the droplet size distribution and spray radius. Future research, therefore, must be devoted to engineer fountain nozzles able to create water droplets with a size distribution that consumes less energy and a trajectory that increases the spray radius.

Appendix A: Model forcing based on water-use efficiency and maximum ice volume objectives

We reduced model complexity and data requirement (Balasubramanian et al., 2022) through assumptions that optimize ice volume (IVOM) or water-use efficiency (WEOM). We define the freezing rate and melting rate as the positive and negative mass change rate, respectively. We choose assumptions based on whether these overestimate or underestimate the freezing rate. IVOM assumptions overestimate freezing rate, whereas WEOM assumptions underestimate freezing rate. We describe these two kinds of assumptions applied on each energy balance component:

350 A1 Surface area A_{cone} assumptions

Determination of surface area during the accumulation period is achieved by assuming a constant ice cone radius equal to the fountain spray radius. The surface area scales the freezing rate of the AIR. Hence, for the IVOM version, we assume the maximum possible slope to be 1 for the ice cone. Therefore, area is estimated as:

$$A_{cone} = \sqrt{2} \cdot \pi \cdot r_F^2 \quad (A1)$$

355 Similarly, for the water-use efficiency objective, the area of the conical AIR is approximated to the area of its circular base. Therefore, area is estimated as:

$$A_{cone} = \pi \cdot r_F^2 \quad (\text{A2})$$

A2 Net shortwave radiation q_{SW} assumptions

The net shortwave radiation q_{SW} is computed as follows:

$$360 \quad q_{SW} = (1 - \alpha) \cdot (SW_{direct} \cdot f_{cone} + SW_{diffuse}) \quad (\text{A3})$$

where α is the albedo value, SW_{direct} is the direct shortwave radiation, $SW_{diffuse}$ is the diffuse shortwave radiation, and f_{cone} is the solar area fraction.

365 The data requirement was reduced by estimating the global shortwave radiation and pressure using directly the location's coordinates and altitude through the solar radiation model described in Holmgren et al. (2018). The algorithm used to estimate the clear-sky global radiation is described in Ineichen (2008).

The diffuse and direct shortwave radiation are determined using the estimated global solar radiation as follows:

$$\begin{aligned} SW_{diffuse} &= cld \cdot SW_{global} \\ SW_{direct} &= (1 - cld) \cdot SW_{global} \end{aligned} \quad (\text{A4})$$

where cld is the cloudiness factor. cld is assumed to be 1 and 0 for the water-use efficiency and ice volume objective, respectively.

370 We ignore the variations in the albedo and assume it to be equal to snow albedo and ice albedo for the ice volume and water-use efficiency objective, respectively.

The solar area fraction f_{cone} of the ice structure exposed to the direct shortwave radiation depends on the shape considered and is computed as:

$$f_{cone} = \frac{(0.5 \cdot r_{cone} \cdot h_{cone}) \cdot \cos\theta_{sun} + (\pi \cdot (r_{cone})^2 / 2) \cdot \sin\theta_{sun}}{\pi \cdot r_{cone} \cdot ((r_{cone})^2 + (h_{cone})^2)^{1/2}} \quad (\text{A5})$$

375 For the ice volume objective, we assume the slope of the cone to be 1; f_{cone} is determined as follows:

$$f_{cone} = \frac{\cos\theta_{sun} + \pi \cdot \sin\theta_{sun}}{2\sqrt{2} \cdot \pi} \quad (\text{A6})$$

Similarly, for the water-use efficiency objective, we assume the slope of the cone to be negligible obtain:

$$f_{cone} = \frac{\sin\theta_{sun}}{2} \quad (\text{A7})$$

A3 Net longwave radiation q_{LW} assumptions

380 We assume $T_{ice} = 0^\circ C$ to determine outgoing longwave radiation. To constrain the minimum ice temperature is challenging; therefore, we maintain this assumption for both our objectives. However, to estimate atmospheric emissivity, we again assume cld to be 1 and 0 for the water-use efficiency and ice volume objective, respectively.

A4 Turbulent fluxes assumptions

385 Turbulent fluxes estimation depends on the slope of the cone through the μ_{cone} parameter. As suggested by Oerlemans et al. (2021), we estimated this parameter as follows:

$$\mu_{cone} = 1 + s_{cone}/2 \quad (\text{A8})$$

Hence, the μ_{cone} parameter takes values of 1.5 and 1 for the ice volume and water-use efficiency objective, respectively. Since turbulent fluxes impact both the freezing and the melting rates, this assumption may not favor the corresponding objectives for certain sites.

Table A1. Free parameters in the model categorized as constant, model hyperparameters, and weather parameters with their respective values/ranges.

Constant parameters	Symbol	Value	Unit	References
Van Karman constant	κ	0.4	dimensionless	Cuffey and Paterson (2010)
Stefan Boltzmann constant	σ	5.67×10^{-8}	$W m^{-2} K^{-4}$	Cuffey and Paterson (2010)
Air pressure at sea level	$p_{0,a}$	1013	hPa	Mölg and Hardy (2004)
Density of water	ρ_w	1000	$kg m^{-3}$	Cuffey and Paterson (2010)
Density of ice	ρ_{ice}	917	$kg m^{-3}$	Cuffey and Paterson (2010)
Density of air	ρ_a	1.29	$kg m^{-3}$	Mölg and Hardy (2004)
Specific heat of water	c_w	4186	$J kg^{-1} {}^\circ C^{-1}$	Cuffey and Paterson (2010)
Specific heat of ice	c_{ice}	2097	$J kg^{-1} {}^\circ C^{-1}$	Cuffey and Paterson (2010)
Specific heat of air	c_a	1010	$J kg^{-1} {}^\circ C^{-1}$	Mölg and Hardy (2004)
Thermal conductivity of ice	k_{ice}	2.123	$W m^{-1} K^{-1}$	Bonales et al. (2017)
Latent heat of sublimation	L_s	2.848×10^6	$J kg^{-1}$	Cuffey and Paterson (2010)
Latent heat of fusion	L_f	3.34×10^5	$J kg^{-1}$	Cuffey and Paterson (2010)
Gravitational acceleration	g	9.81	$m s^{-2}$	Cuffey and Paterson (2010)
Weather station height	h_{AWS}	2	m	assumed
Model timestep	Δt	3600	s	assumed

Model Hyperparameters	Symbol	Range	Unit	References
Surface layer thickness	Δx	$[1 \times 10^{-2}, 1 \times 10^{-1}]$	m	assumed

Weather parameters	Symbol	Range	Unit	References
Ice emissivity	ϵ_{ice}	[0.95, 0.99]	dimensionless	Hori et al. (2006)
Surface roughness	z_0	$[1 \times 10^{-3}, 5 \times 10^{-3}]$	m	Brock et al. (2006)
Ice albedo	α_{ice}	[0.15, 0.35]	dimensionless	Steiner et al. (2015); Zolles et al. (2019)
Snow albedo	α_{snow}	[0.8, 0.9]	dimensionless	Zolles et al. (2019)
Precipitation temperature threshold	T_{ppt}	[0, 2]	${}^\circ C$	ShiChang et al. (2010)
Albedo decay rate	τ	[10, 22]	$days$	Schmidt et al. (2017); Oerlemans and Knap (1998)

390 *Author contributions.* **Suryanarayanan Balasubramanian:** Conceptualization, Methodology, Investigation, Data curation, Visualization, Software, Writing – original draft preparation. **Martin Hoelzle:** Conceptualization, Supervision, Investigation, Writing – review and editing. **Roger Waser:** Resources – automation system, Writing – review and editing.

Competing interests. The authors declare that they have no known competing financial interests or personal relationships that could have appeared to influence the work reported in this paper.

395 *Financial support.* This work was supported and funded by the University of Fribourg and by the Swiss Government Excellence Scholarship (SB). The associated fieldwork in Guttannen was funded by the Glaciers Alive Association.

400 *Acknowledgements.* This work would not have been possible without the unconditional support of Daniel Bürki from Guttannen Bewegt Association to manage our field experiments for the past three winters. David Sciboz, Maria Gruber and Dominik Amschwand helped us install the weather station and the automation system. The smooth operation of the automation system was possible due to the user interface designed by Martin Von Burg. We would particularly like to thank our english editors Ana Rodríguez Crespo and Akshatha N Tirumale. We also thank Dr. Eric Pohl for valuable suggestions that improved the manuscript.

References

- Aggarwal, A., Frey, H., McDowell, G., Drenkhan, F., Nüsser, M., Racoviteanu, A., and Hoelzle, M.: Adaptation to Climate Change Induced Water Stress in Major Glacierized Mountain Regions, *Climate and Development*, 0, 1–13, 405 <https://doi.org/10.1080/17565529.2021.1971059>, 2021.
- Balasubramanian, S., Hoelzle, M., Lehning, M., Bolibar, J., Wangchuk, S., Oerlemans, J., and Keller, F.: Influence of Meteorological Conditions on Artificial Ice Reservoir (Icestupa) Evolution, *Frontiers in Earth Science*, 9, 771 342, <https://doi.org/10.3389/feart.2021.771342>, 2022.
- Barandun, M., Fiddes, J., Scherler, M., Mathys, T., Saks, T., Petrakov, D., and Hoelzle, M.: The State and Future of the Cryosphere in Central 410 Asia, *Water Security*, 11, 100 072, <https://doi.org/10.1016/j.wasec.2020.100072>, 2020.
- BBC News: Bright Artificial Glacier in Naryn - BBC Kyrgyz, <https://www.youtube.com/watch?v=TpeSQf75bFQ>, 2020.
- Bonales, L. J., Rodriguez, A. C., and Sanz, P. D.: Thermal Conductivity of Ice Prepared under Different Conditions, *International Journal of Food Properties*, 20, 610–619, <https://doi.org/10.1080/10942912.2017.1306551>, 2017.
- Brock, B. W., Willis, I. C., and Sharp, M. J.: Measurement and Parameterization of Aerodynamic Roughness Length Variations at Haut 415 Glacier d’Arolla, Switzerland, *Journal of Glaciology*, 52, 281–297, <https://doi.org/10.3189/172756506781828746>, 2006.
- Clouse, C., Anderson, N., and Shippling, T.: Ladakh’s Artificial Glaciers: Climate-Adaptive Design for Water Scarcity, *Climate and Development*, 9, 428–438, <https://doi.org/10.1080/17565529.2016.1167664>, 2017.
- Cuffey, K. M. and Paterson, W. S. B.: *The Physics Of Glaciers*, Elsevier, 2010.
- Farhan, S. B., Zhang, Y., Ma, Y., Guo, Y., and Ma, N.: Hydrological Regimes under the Conjunction of Westerly and Monsoon Climates: A 420 Case Investigation in the Astore Basin, Northwestern Himalaya, *Climate Dynamics*, 44, 3015–3032, <https://doi.org/10.1007/s00382-014-2409-9>, 2015.
- Hanzer, F., Carmagnola, C. M., Ebner, P. P., Koch, F., Monti, F., Bavay, M., Bernhardt, M., Lafaysse, M., Lehning, M., Strasser, U., François, H., and Morin, S.: Simulation of Snow Management in Alpine Ski Resorts Using Three Different Snow Models, *Cold Regions Science and Technology*, 172, 102 995, <https://doi.org/10.1016/j.coldregions.2020.102995>, 2020.
- Hersbach, H., Bell, B., Berrisford, P., Hirahara, S., Horányi, A., Muñoz-Sabater, J., Nicolas, J., Peubey, C., Radu, R., Schepers, D., Simmons, 425 A., Soci, C., Abdalla, S., Abellan, X., Balsamo, G., Bechtold, P., Biavati, G., Bidlot, J., Bonavita, M., Chiara, G. D., Dahlgren, P., Dee, D., Diamantakis, M., Dragani, R., Flemming, J., Forbes, R., Fuentes, M., Geer, A., Haimberger, L., Healy, S., Hogan, R. J., Hólm, E., Janisková, M., Keeley, S., Laloyaux, P., Lopez, P., Lupu, C., Radnoti, G., de Rosnay, P., Rozum, I., Vamborg, F., Villaume, S., and Thépaut, J.-N.: The ERA5 Global Reanalysis, *Quarterly Journal of the Royal Meteorological Society*, 146, 1999–2049, 2020.
- Hoelzle, M., Barandun, M., Bolch, T., Fiddes, J., Gafurov, A., Muccione, V., Saks, T., and Shahgedanova, M.: The Status and Role of the 430 Alpine Cryosphere in Central Asia, <https://doi.org/10.4324/9780429436475-8>, 2019.
- Holmgren, W. F., Hansen, C. W., and Mikofski, M. A.: Pvlib Python: A Python Package for Modeling Solar Energy Systems, *Journal of Open Source Software*, 3, 884, <https://doi.org/10.21105/joss.00884>, 2018.
- Hori, M., Aoki, T., Tanikawa, T., Motoyoshi, H., Hachikubo, A., Sugiura, K., Yasunari, T. J., Eide, H., Storvold, R., Nakajima, Y., and 435 Takahashi, F.: In-Situ Measured Spectral Directional Emissivity of Snow and Ice in the 8–14 Mm Atmospheric Window, *Remote Sensing of Environment*, 100, 486–502, <https://doi.org/10.1016/j.rse.2005.11.001>, 2006.
- Immerzeel, W. W., Lutz, A. F., Andrade, M., Bahl, A., Biemans, H., Bolch, T., Hyde, S., Brumby, S., Davies, B. J., Elmore, A. C., Emmer, A., Feng, M., Fernández, A., Haritashya, U., Kargel, J. S., Koppes, M., Kraaijenbrink, P. D. A., Kulkarni, A. V., Mayewski, P. A., Nepal, S.,

Pacheco, P., Painter, T. H., Pellicciotti, F., Rajaram, H., Rupper, S., Sinisalo, A., Shrestha, A. B., Viviroli, D., Wada, Y., Xiao, C., Yao, T., and Baillie, J. E. M.: Importance and Vulnerability of the World's Water Towers, *Nature*, 577, 364–369, <https://doi.org/10.1038/s41586-019-1822-y>, 2020.

440 Ineichen, P.: A Broadband Simplified Version of the Solis Clear Sky Model, *Solar Energy*, 82, 758–762, <https://doi.org/10.1016/j.solener.2008.02.009>, 2008.

IPCC: Chapter 2: High Mountain Areas — Special Report on the Ocean and Cryosphere in a Changing Climate, *IPCC Special Report on the
445 Ocean and Cryosphere in a Changing Climate*, 2019.

Meteoblue: Climate Guttannen, https://www.meteoblue.com/en/weather/historyclimate/climatemodelled/guttannen_switzerland_2660433, 2021.

Mölg, T. and Hardy, D. R.: Ablation and Associated Energy Balance of a Horizontal Glacier Surface on Kilimanjaro, *J. Geophys. Res.-Atmos.*, 109, 1–13, <https://doi.org/10.1029/2003JD004338>, 2004.

450 Norphel, C. and Tashi, P.: Snow Water Harvesting in the Cold Desert in Ladakh: An Introduction to Artificial Glacier, in: *Mountain Hazards and Disaster Risk Reduction*, edited by Nibanupudi, H. K. and Shaw, R., *Disaster Risk Reduction*, pp. 199–210, Springer Japan, Tokyo, https://doi.org/10.1007/978-4-431-55242-0_11, 2015.

Nüsser, M. and Baghel, R.: Local Knowledge and Global Concerns: Artificial Glaciers as a Focus of Environmental Knowledge and Development Interventions, in: *Ethnic and Cultural Dimensions of Knowledge*, edited by Meusburger, P., Freytag, T., and Suarsana, L.,
455 *Knowledge and Space*, pp. 191–209, Springer International Publishing, Cham, https://doi.org/10.1007/978-3-319-21900-4_9, 2016.

Nüsser, M., Dame, J., Kraus, B., Baghel, R., and Schmidt, S.: Socio-Hydrology of Artificial Glaciers in Ladakh, India: Assessing Adaptive Strategies in a Changing Cryosphere, *Regional Environmental Change*, <https://doi.org/10.1007/s10113-018-1372-0>, 2019.

Oerlemans, J. and Knap, W. H.: A 1 Year Record of Global Radiation and Albedo in the Ablation Zone of Morteratschgletscher, Switzerland, *Journal of Glaciology*, 44, 231–238, <https://doi.org/10.3189/S0022143000002574>, 1998.

460 Oerlemans, J., Balasubramanian, S., Clavuot, C., and Keller, F.: Brief Communication: Growth and Decay of an Ice Stupa in Alpine Conditions – a Simple Model Driven by Energy-Flux Observations over a Glacier Surface, *The Cryosphere*, 15, 3007–3012, <https://doi.org/10.5194/tc-15-3007-2021>, 2021.

Palmer, L.: Storing Frozen Water to Adapt to Climate Change, *Nature Climate Change*, 12, 115–117, <https://doi.org/10.1038/s41558-021-01260-x>, 2022.

465 Poiseuille: Experimental Investigations on the Flow of Liquids in Tubes of Very Small Diameter, 21, 76, 1847.

Reuters: Conservationists in Chile Aim to Freeze Water in Man-Made Glaciers, *Reuters*, 2021.

Schmidt, L. S., Aðalgeirs Þóttir, G., Guðmundsson, S., Langen, P. L., Pálsson, F., Mottram, R., Gascoin, S., and Björnsson, H.: The Importance of Accurate Glacier Albedo for Estimates of Surface Mass Balance on Vatnajökull: Evaluating the Surface Energy Budget in a Regional Climate Model with Automatic Weather Station Observations, *The Cryosphere*, 11, 1665–1684, <https://doi.org/10.5194/tc-11-1665-2017>,
470 2017.

ShiChang, TanGuang, G., ShiQiao, Z. G. Z., and Kang: Response of Zhadang Glacier Runoff in Nam Co Basin, Tibet, to Changes in Air Temperature and Precipitation Form, *Chinese Science Bulletin*, 55, 2103–2110, <https://doi.org/10.1007/s11434-010-3290-5>, 2010.

Steiner, J. F., Pellicciotti, F., Buri, P., Miles, E. S., W. T. D. I. W., and Reid: Modelling Ice-Cliff Backwasting on a Debris-Covered Glacier in the Nepalese Himalaya, *Journal of Glaciology*, 61, 889–907, <https://doi.org/10.3189/2015JoG14J194>, 2015.

475 Tveiten, I.: Glacier Growing - A Local Response to Water Scarcity in Baltistan and Gilgit, Pakistan, Ph.D. thesis, 2007.

Vince, G.: Glacier Man, *Science*, 326, 659–661, https://doi.org/10.1126/science.326_659, 2009.

Vincent, S.: Energy and Climate Change in Cold Regions of Asia, 2009.

Wangchuk, S.: Ice Stupa Competition, <https://tribal.nic.in/IceStupa.aspx>, 2020.

Xenarios, S., Schmidt-Vogt, D., Qadir, M., Janusz-Pawletta, B., and Abdullaev, I.: The Aral Sea Basin: Water for Sustainable Development

480 in Central Asia, Routledge, 100-121, 2019.

Zolles, T., Maussion, F., Galos, S. P., Gurgiser, W., and Nicholson, L.: Robust Uncertainty Assessment of the Spatio-Temporal Transferability
of Glacier Mass and Energy Balance Models, *The Cryosphere*, 13, 469–489, <https://doi.org/10.5194/tc-13-469-2019>, 2019.

7.3 Paper III

Brief communication: Growth and decay of an ice stupa in alpine conditions – a simple model driven by energy-flux obser- vations over a glacier surface

Oerlemans, J., S. Balasubramanian, C. Clavuot, and F. Keller. *The Cryosphere* 15, no. 6 (2021): 3007–12. doi:10.5194/tc-15-3007-2021.



Brief communication: Growth and decay of an ice stupa in alpine conditions – a simple model driven by energy-flux observations over a glacier surface

Johannes Oerlemans¹, Suryanarayanan Balasubramanian², Conradin Clavuot³, and Felix Keller^{4,5}

¹Institute for Marine and Atmospheric Research, Utrecht University, Princetonplein 5, Utrecht, 3585CC, the Netherlands

²Department of Geosciences, University of Fribourg, Fribourg, Switzerland

³Architecture Clavuot, Gängelistrasse 49, Chur 7000, Switzerland

⁴Academia Engiadina, Samedan, Switzerland

⁵Department of Environmental Systems Science, ETH, Zurich, Switzerland

Correspondence: Johannes Oerlemans (j.oerlemans@uu.nl)

Received: 13 February 2021 – Discussion started: 1 April 2021

Revised: 30 May 2021 – Accepted: 4 June 2021 – Published: 29 June 2021

Abstract. We present a simple model to calculate the evolution of an ice stupa (artificial ice reservoir). The model is formulated for a cone geometry and driven by energy balance measurements over a glacier surface for a 5-year period. An “exposure factor” is introduced to deal with the fact that an ice stupa has a very rough surface and is more exposed to wind than a flat glacier surface. The exposure factor enhances the turbulent fluxes.

For characteristic alpine conditions at 2100 m, an ice stupa may reach a volume of 200 to 400 m³ in early April. We show sensitivities of ice stupa size to temperature changes and exposure factor. The model may also serve as an educational tool, with which the effects of snow cover, switching off water during daytime, different starting dates, switching off water during high wind speeds, etc. can easily be evaluated.

1 Introduction

Ice stupas (Fig. 1), also referred to as artificial ice reservoirs (AIRs), are used more and more as a means to store water in the form of ice (Nüsser et al., 2018). In Ladakh, India, engineer Sonam Wangchuk initiated and developed the use of ice stupas to provide water for irrigation purposes in spring and early summer. The ice stupas grow in winter by sprinkling water on the growing ice structure, and they melt in spring and summer to deliver water; a typical turnover volume is up

to 1×10^6 L. Ice stupas also form interesting touristic attractions with a distinct and special artistic flavour. They come in the same class as ice sculptures, which are popular in all regions of the world that have a cold winter.

The possibility to grow ice stupas of appreciable size depends on the meteorological conditions and the availability of water. When a surface has a negative energy balance and water is sprayed on it, ice will form (a well-known technique to make skating rinks). The more effective the latent heat of fusion can be removed by contact with cold air and effective emittance of longwave radiation, the faster the ice layer may grow. In spring and summer incoming solar radiation will dominate and the ice stupa will lose mass.

In this note we present a model of ice stupa growth and decay, based on a simple consideration of the total energy budget, and driven by energy flux observations over a glacier surface (half hourly observations over a 5-year period). We believe that the energy balance of a glacier surface and of an ice stupa have much in common and therefore consider this data set as ideal for a first study. The focus is on alpine conditions at a typical height of 2100 m a.s.l. The purpose of this study is to obtain first-order estimates of how fast an ice stupa may grow and melt and what processes are most important. We emphasize that in this note the focus is on the energetics of the ice stupa system, not on the technical aspects that have to be dealt with in constructing an ice stupa.



Figure 1. (a) Ice stupa in Ladakh, India (courtesy of Sonam Wangchuk). (b) Early growing stage of ice stupa with inner structure in Val Roseg, Switzerland (courtesy of Conradin Clavuot). (c) Simple geometrical representation. The ice stupa can have an inner structure (brown). The dashed lines illustrate the growth of an ice stupa from a base with a constant radius.

2 Geometry

Ice stupas have different and often complex shapes. The *cone* is probably the most appropriate simple geometric shape to represent an ice stupa (Fig. 1), but alternatively a *dome* (half sphere) could also be considered.

The geometric characteristics of a cone with radius r and height h are

$$\text{Area of base: } \pi r^2, \quad (1a)$$

$$\text{Lateral area: } \pi r \sqrt{r^2 + h^2}, \quad (1b)$$

$$\text{Volume: } \pi r^2 h / 3. \quad (1c)$$

It is useful to introduce a shape parameter $s = h/r$. The volume can then also be written as

$$V = \pi r^3 / 3s^2. \quad (2)$$

So for a given volume the height of the ice stupa can be calculated from

$$h = \left\{ \frac{3}{\pi} V s^2 \right\}^{1/3}. \quad (3)$$

In this note we will consider two cases: (i) the shape factor is constant during growth and decay, and (ii) the ice stupa grows upward from a base with a fixed radius, implying that the shape factor gradually increases. The first case may be more appropriate when an inner structure is used or when water supply is by varying sprinkler properties or even manually. Case (ii) describes better the situation when a fixed spray radius is maintained during the growth phase.

3 Energy exchange

Ice stupas exchange energy with the surroundings by absorbing and reflecting solar radiation, absorbing and emitting longwave (terrestrial) radiation, and by turbulent fluxes

of sensible and latent heat. Because of the complex shape of an ice stupa, as compared to a horizontal ice/snow surface, it is hard to describe these processes in detail. However, some simplifying assumptions may help to arrive at reasonable approximations.

We use 5 years of energy balance measurements with an automatic weather station (AWS) on the Vadret da Morteratsch (Morteratsch Glacier) (e.g. Oerlemans et al., 2009), which was located at an elevation of about 2280 m a.s.l. The surface energy flux is written as

$$\text{energy flux} = S_{\text{in}} - S_{\text{out}} + L_{\text{in}} - L_{\text{out}} + H + G. \quad (4)$$

S_{in} stands for solar radiation, S_{out} for reflected solar radiation, L_{in} for incoming longwave radiation, L_{out} for emitted longwave radiation, H for the total turbulent heat flux, and G for the ground heat flux (conduction from or into the surface layer – generally small compared to the other components). These quantities are normally expressed in W m^{-2} . So the energy flux is positive when directed towards the surface. A positive energy flux will be used for melting of ice or snow; when the energy flux is negative freezing of water can take place (when available).

We now discuss how these measurements over (almost) flat terrain can be applied to an ice stupa. We first deal with solar radiation and consider the direct part (fraction q) and diffuse part (fraction $1-q$) separately. Although the ratio of direct to diffuse solar radiation depends strongly on cloud conditions, outside subtropical climate zones where low cloudiness prevails the components are typically of the same order of magnitude (e.g. Li et al., 2015; Berrizbeitia et al., 2020).

With respect to direct solar radiation, the solar beam can be considered to have a vertical component, impinging on the horizontal surface (base of the ice stupa), and a horizontal component impinging on the vertical cross section (a triangle). Measurements over a flat surface, like those from

the glacier AWS, thus underestimate the solar radiation intercepted by an ice stupa. A correction factor f is therefore needed with which the direct radiation as measured by the AWS has to be multiplied. This factor may be large for a low sun, but in alpine conditions where there is always significant shading by the surroundings this situation is rarely found. A simple analysis shows that, for a shape factor of $s = 2$, f varies from 2.5 for a solar elevation of 20° to about 1.2 for a solar elevation of 60° . To account for the fact that the correction factor should be 1 for a flat surface and increase with the shape factor, we use (note that f and s are dimensionless)

$$f = 1 + s/4. \quad (5)$$

For the *diffuse* part of the solar radiation, illumination is on all sides and the relevant area therefore is the lateral area as given in Eq. (1b). Therefore the total amount of absorbed solar radiation per unit of time can be estimated as (in J s^{-1})

$$F_{\text{sol}} = f q (S_{\text{in}} - S_{\text{out}}) \pi r^2 + (1 - q) (S_{\text{in}} - S_{\text{out}}) \pi r \sqrt{r^2 + h^2}. \quad (6)$$

Alternatively, one may wish to prescribe the albedo α separately, i.e.

$$F_{\text{sol}} = f q S_{\text{in}} (1 - \alpha) \pi r^2 + (1 - q) S_{\text{in}} (1 - \alpha) \pi r \sqrt{r^2 + h^2}. \quad (7)$$

For the longwave radiation and turbulent exchange, the exposed surface is also the lateral area. The longwave radiation balance then becomes

$$F_{\text{lw}} = (L_{\text{in}} - L_{\text{out}}) \pi r \sqrt{r^2 + h^2}. \quad (8)$$

The turbulent heat fluxes depend on the roughness and exposure of the surface. Since we do not calculate the surface (skin) temperature, we simply assume that it is close to the melting point. The sensible and latent heat input are calculated using the well-known bulk transfer equations (e.g. Garratt, 1992):

$$F_H = \mu \rho c_p C U (T - T_s) \pi r \sqrt{r^2 + h^2} \quad (9)$$

$$F_L = 0.623 \mu \rho L_v C U p^{-1} (e_s - e) \pi r \sqrt{r^2 + h^2}. \quad (10)$$

Here C is the bulk turbulent exchange coefficient over a flat surface, T is the air temperature, T_s is the surface temperature (set to the melting point), ρ is air density, L_v is the latent heat of sublimation ($2830\,000 \text{ J kg}^{-1}$), c_p is the specific heat capacity of air ($1004 \text{ J kg}^{-1} \text{ K}^{-1}$), e is the vapour pressure, e_s is the saturation vapour pressure, p is atmospheric pressure, and U is the wind speed. The total turbulent heat flux H is just the sum of the fluxes of sensible and latent heat.

The dimensionless parameter μ is an “exposure/roughness parameter” that deals with the fact that an ice stupa has a rough appearance and forms an obstacle to the wind regime. So μ is expected to be larger than 1 and could perhaps have a

value of 2 or more. For a larger shape parameter the exposure will be larger; we therefore use

$$\mu = 1 + s/2. \quad (11)$$

Equation (9) is no more than an educated guess. It is hard to base estimates of this parameter on information in the literature. Many studies have been carried out on the effect of obstacles on atmospheric boundary layer flow (e.g. trees, but also buildings), but always in an ensemble setting, looking at the bulk effect of an ensemble of obstacles. We deal with a case of a single obstacle in open terrain, and we are confident that the roughness of the surface and the exposure will lead to larger turbulent fluxes. Given the uncertainty in the exposure parameter, later on we will present results for different values.

When water availability is unlimited, the mass gain or loss is given by

$$\frac{dM}{dt} = (F_{\text{sol}} + F_{\text{lw}} + F_L + F_H)/L_m + F_L/L_v. \quad (12)$$

M is the mass of the ice stupa and L_m is the latent heat of melting/fusion ($334\,000 \text{ J kg}^{-1}$). For typical alpine conditions the last term in Eq. (10) is normally quite small. Since the volume of the ice stupa is simply related to the mass ($V = M/\rho_{\text{ice}}$), the height of the stupa can directly be calculated for a given shape factor (case i) or given radius (case ii).

4 Application to the Oberengadin region, Switzerland

Over the past few years, several ice stupas have been constructed in the Oberengadin, southeast Switzerland. In the winter of 2017/2018 an ice stupa was constructed in the Val Roseg at 2000 m a.s.l. (Fig. 1, maximum height about 12 m). In the winter of 2018/2019 several smaller ice stupas (height about 5 m) were built at a site in the Val Morteratsch at about 1900 m a.s.l. Since February 2021 a test site for ice stupa construction has been in operation at the Diavolezza Talstation at an altitude of 2080 m a.s.l.

To obtain first-order estimates of growth and decay rates for typical climatic conditions in the Oberengadin, we used the energy balance measurements from the automatic weather station on the Vadret da Morteratsch as a proxy for this high alpine region. During the period 1 July 2007–30 September 2012, the AWS on the Vadret da Morteratsch was located at an altitude of about 2280 m a.s.l. and has produced a unique data set without any gaps. The annual melt at the AWS location was between 5 and 7 m of ice. With a focus on the Diavolezza site, which is at an altitude of 2080 m a.s.l., a temperature correction of $+1.3 \text{ K}$ was applied to the input data (based on a standard atmospheric temperature lapse rate of 0.0065 K m^{-1}). We note that all the locations mentioned above are within a distance of 10 km from each other (interactive map to find locations: <https://map.wanderland.ch>, last access: 25 June 2021).

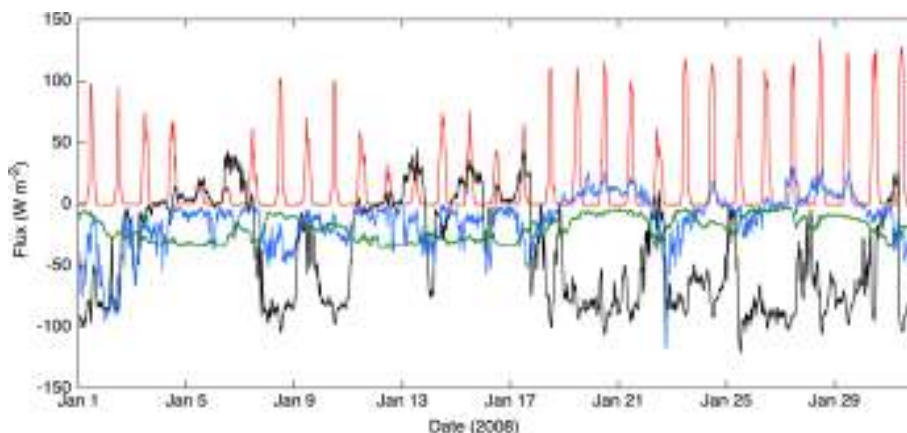


Figure 2. Energy balance components as measured by the AWS on the Vadret da Morteratsch for January 2008. Net solar radiation in red, net longwave radiation flux in black, turbulent sensible heat flux in blue, turbulent latent heat flux in green.

Figure 2 shows an example of data from the AWS. The data have been stored as 30 min averages. The turbulent heat fluxes have been calculated from the wind speed, air temperature, and humidity, where the turbulent exchange coefficient C was used as a tuning parameter (to obtain the correct amount of observed ice melt over a 5-year period). The example shown is just for one relatively sunny winter month (January 2008). Note the large degree of compensation between net solar radiation and net longwave radiation – the well-known effect in clear sky conditions on the radiation balance. As a consequence, the turbulent heat fluxes are more important than it appears at first sight.

Figure 3 summarizes model results in terms of ice stupa height and volume for 5 years. In all calculations we used $q = 0.5$ and $\alpha = 0.6$. It has been assumed that water availability is unlimited. In the first example (Fig. 3a) we show the evolution of an ice stupa on a 5 m high inner structure. In the model this is simply achieved by setting $h = 5$ m at the start of the integration and correct the total volume afterwards for the volume of the inner structure. The use of an inner structure has the advantage that the freezing area is larger from the beginning and that the typical ice stupa shape is achieved relatively fast. The shape factor has been taken constant and equal to 2. We see some differences among the years: the maximum ice stupa height varies between 10 and 12 m and is normally reached in early April. For the last 2 years the simulated ice stupa volume is smaller mainly because of slightly higher temperatures and larger insolation. The decay of the ice stupa is hardly faster than the growth. A faster decay would occur if the albedo were not constant but would be prescribed to decrease during the melt phase (which is more realistic in most cases).

Figure 3b shows a comparison between the fixed-shape simulation just described and a fixed-radius simulation with $r = 7$ m. This value of the radius was chosen to obtain more or less the same ice stupa volume. It can be seen that in the first stage of growth the volume for the fixed-radius case in-

creases somewhat faster than for the fixed-shape case. Nevertheless, the differences in the curves are not large and point to the fact that in the end the energy constraints determine how much ice can form (in the case of unlimited water availability).

Because the value of the exposure parameter μ is highly uncertain, we show the sensitivity of the fixed-radius ice stupa volume to different formulations (Fig. 3c). For $\mu = 1$, implying that the situation is equivalent to that of a flat surface, the stupa volume is significantly smaller than in the reference case ($\mu = 1+s/2$). A stronger dependence of μ on the shape factor ($\mu = 1+s$) increases the stupa volume by about 25 %. For a larger shape factor, the mostly negative turbulent fluxes in winter increase, and this is not compensated by a larger interception of solar radiation.

In the simulations discussed so far the ice stupas disappear in summer. One may ask the question under what conditions an ice stupa may survive the summer and grow to a larger size in the next winter. A possible way to study this question is to decrease the air temperature uniformly (temperature change ΔT). This will imply a stronger negative sensible heat flux in winter and a weaker positive heat flux in summer, thus accelerating stupa growth and slowing down its decay. We found a break-even point for $\Delta T \approx -2$ K (Fig. 3d). For larger negative values of ΔT the ice stupa does not disappear in summer and keeps growing from year to year. For $\Delta T \approx -3$ K, the maximum volume in the fifth year (~ 2400 m 3) is about 4 times that in the first year (~ 600 m 3). We note that in this calculation the effect of lower temperatures on the net longwave radiation balance has not been taken into account, because the radiation fluxes were prescribed according to the AWS observations. It is likely that we therefore underestimate the effect of lower air temperature.

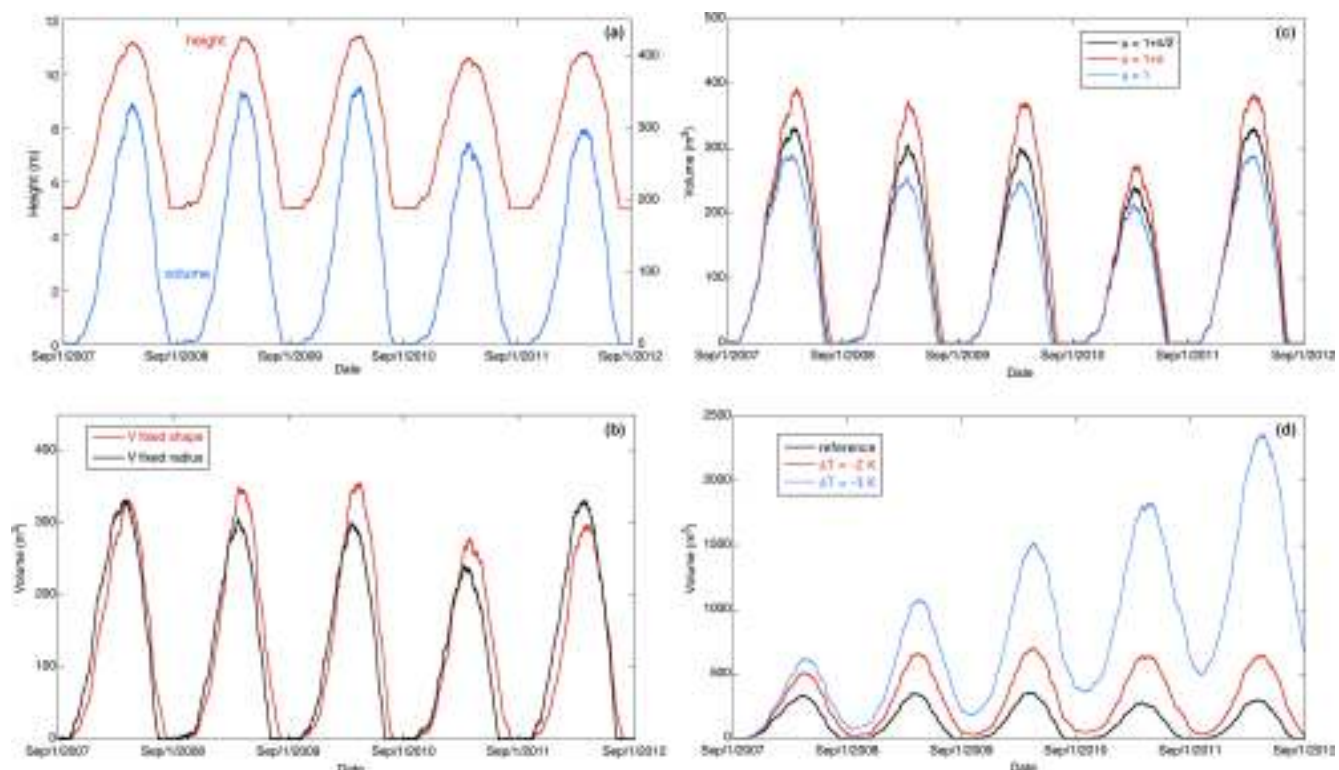


Figure 3. Calculated evolution of ice stupa for the case of unlimited water supply for five winters. **(a)** Height and volume for the case with an inner structure (height 5 m) and fixed shape. **(b)** Volume for the case with an inner structure and the case with a fixed radius (7 m). **(c)** The effect of the exposure parameter μ on the volume (fixed radius). **(d)** The effect of a negative temperature perturbation. For $\Delta T = -3 K$ the stupa does not disappear anymore but is growing from year to year (fixed shape).

5 Discussion

The data set used to simulate ice stupa growth and decay for typical conditions in the Oberengadin is probably quite appropriate. The setting of the location of the AWS (on the lower tongue of the Vadret da Morteratsch when it still existed) and the Diavolezza Talstation are rather similar: the altitude is about the same, and the valley is relatively wide. However, differences in the wind statistics are likely to exist, but they are difficult to assess. The Morteratsch AWS reveals a steady katabatic (glacier) wind most of the time, whereas the Diavolezza Talstation is more exposed to the larger-scale wind regime. It seems likely that the average wind speed at the Diavolezza Talstation is somewhat higher than at the AWS site, where the 5-year average wind speed is 2.8 m s^{-1} . In contrast, the sites in the Val Roseg and Val Morteratsch are more sheltered and wind speeds are probably lower.

The examples presented here are best-case scenarios with respect to ice stupa growth. In practice it is not always possible to have unlimited water availability, and it may be difficult to sprinkle the water more or less evenly over the stupa, especially at higher wind speeds. The choice of the shape of the ice stupa depends on the sprinkling strategy. It may be more realistic to describe an ice stupa with different shapes

for the growth phase (e.g. fixed radius) and decay phase (e.g. constant shape factor). Such an approach can easily be accommodated in the model.

We note that the ice stupa volume calculated here for alpine conditions at $\sim 2100 \text{ m a.s.l.}$ (typically 250 m^3) is significantly smaller than the volumes obtained in the big ice stupas in Ladakh. Winter conditions in Ladakh are considerably colder and therefore growth rates can be much larger.

In this exploratory study a solid comparison between observed and simulated stupa sizes was not attempted. However, we note that the maximum height of the stupa in the Val Roseg was 12 m, which is in good agreement with the stupa height shown in Fig. 3a.

The model presented here is simple, basically because we consider the ice stupa to be a single unit with a surface temperature close to the melting point. As soon as this constraint is relaxed and the surface temperature of the stupa is considered to be a dependent variable, the whole procedure becomes more complicated, and some processes can be studied more explicitly. Nevertheless, we believe that the simple approach presented in this note, which requires no more than one page of coding, is a useful tool to obtain first-order estimates of growth and decay rates under various conditions. Effects of snow cover, switching off water during daytime,

switching of water supply for high wind speeds, different starting dates, differences between warm and cold winters, etc. can be evaluated. We finally note that the model can easily be reformulated for another geometry, e.g. a dome.

Data availability. The 5-year data set from the weather station on the Vadret da Morteratsch is available on request.

Author contributions. JO designed, coded, and ran the model. Through their experience in constructing ice stupas, SB, CC, and FK have made important contributions concerning the concept and application of the model. JO wrote the text of this communication.

Competing interests. The authors declare that they have no conflict of interest.

Disclaimer. Publisher's note: Copernicus Publications remains neutral with regard to jurisdictional claims in published maps and institutional affiliations.

Acknowledgements. We thank the reviewers and editor for their constructive comments. The operation of the weather station on the Vadret da Morteratsch was made possible by the NWO-SPINOZA grant (Dutch Research Council) to Johannes Oerlemans.

Review statement. This paper was edited by Chris Derksen and reviewed by Jonathan D. Mackay and two anonymous referees.

References

- Berrizbeitia, S. E., Cago, E. J., and Muneer, T.: Empirical models of the estimation of solar sky-diffusive radiation. A review and experimental analysis, *Energies*, 13, 701, <https://doi.org/10.3390/en13030701>, 2020.
- Garratt, J.: *The Atmospheric Boundary Layer*, Cambridge University Press, 316 pp., ISBN 0521380529, 1992.
- Li, D. H. W., Lou, S. W., and Lam, J. C.: An analysis of global, direct and diffuse solar radiation, *Energy Procedia*, 75, 388–393, 2015.
- Nüsser, M., Dame, J., Kraus, B., Baghel, R., and Schmidt, S.: Socio-hydrology of artificial glaciers in Ladakh, India: assessing adaptive strategies in a changing cryosphere, *Reg. Environ. Change*, 19, 1327–1337, <https://doi.org/10.1007/s10113-018-1372-0>, 2018.
- Oerlemans, J., Giesen, R. H., and Van den Broeke, M. R.: Retreating alpine glaciers: increased melt rates due to accumulation of dust (Vadret da Morteratsch, Switzerland), *J. Glaciol.*, 55, 729–736, 2009.

Bibliography

- Aggarwal, Anubha, Holger Frey, Graham McDowell, et al. (Sept. 2021). "Adaptation to Climate Change Induced Water Stress in Major Glaciated Mountain Regions". In: *Climate and Development* 0.0, pp. 1–13 (cit. on pp. 2, 41).
- Arndt, Anselm, Dieter Scherer, and Christoph Schneider (Apr. 2021). "Atmosphere Driven Mass-Balance Sensitivity of Halji Glacier, Himalayas". In: *Atmosphere* 12.4, p. 426 (cit. on p. 36).
- Awaz Production (Mar. 2022). *Ice Stupa | Artificial Glacier Grafting in Skardu* (cit. on p. 2).
- Bagla, Pallava (Oct. 1998). "Artificial Glaciers to Help Farmers". In: *Science* 282.5389, pp. 619–619 (cit. on pp. 2, 56).
- BBC News (Feb. 2020). *Bright Artificial Glacier in Naryn - BBC Kyrgyz*. <https://www.youtube.com/watch?v=TpeSQ> (cit. on pp. 2, 41).
- Benn, Douglas I and Evans, David JA (2014). *Glaciers and Glaciation*. Routledge (cit. on p. 4).
- Bonales, L. J., A. C. Rodriguez, and P. D. Sanz (2017). "Thermal Conductivity of Ice Prepared under Different Conditions". In: *International Journal of Food Properties* 20.sup1, pp. 610–619 (cit. on p. 28).
- Brock, Ben W., Ian C. Willis, and Martin J. Sharp (2006). "Measurement and Parameterization of Aerodynamic Roughness Length Variations at Haut Glacier d'Arolla, Switzerland". In: *Journal of Glaciology* 52.177, pp. 281–297 (cit. on p. 28).
- Brutsaert, W. (1982). *Evaporation into the Atmosphere. Theory, History and Application*. Kluwer Academic Publishers (cit. on p. 20).
- (1975). "On a Derivable Formula for Long-Wave Radiation from Clear Skies". In: *Water Resources Research* 11.1-4, pp. 742–744 (cit. on p. 20).
- Buytaert, Wouter, Simon Moulds, Luis Acosta, et al. (Nov. 2017). "Glacial Melt Content of Water Use in the Tropical Andes". In: *Environmental Research Letters* 12.11, p. 114014 (cit. on p. 60).
- Chevuturi, A., A. P. Dimri, and R. J. Thayyen (Jan. 2018). "Climate Change over Leh (Ladakh), India". In: *Theoretical and Applied Climatology* 131.1, pp. 531–545 (cit. on p. 1).
- Clouse, Carey, Naomi Anderson, and Taylor Shippling (2017). "Ladakh's Artificial Glaciers: Climate-Adaptive Design for Water Scarcity". In: *Climate and Development* 9.5, pp. 428–438 (cit. on pp. 1, 3).
- Cogley, J. G., A. A. Arendt, A. Bauder, et al. (2010). "Glossary of Glacier Mass Balance and Related Terms". In: (cit. on p. 4).

- Cuffey, Kurt M. and W. S. B. Paterson (2010). *The Physics Of Glaciers*. Elsevier (cit. on pp. 17, 28).
- Farhan, Suhaib Bin, Yinsheng Zhang, Yingzhao Ma, Yanhong Guo, and Ning Ma (June 2015). “Hydrological Regimes under the Conjunction of Westerly and Monsoon Climates: A Case Investigation in the Astore Basin, Northwestern Himalaya”. In: *Climate Dynamics* 44.11, pp. 3015–3032 (cit. on p. 1).
- Furukawa, Yasutaka and Jean Ponce (2010). “Accurate, Dense, and Robust Multiview Stereopsis”. In: *IEEE Transactions on Pattern Analysis and Machine Intelligence* 32.8, pp. 1362–1376 (cit. on p. 131).
- Garratt, J. R. (1992). *The Atmospheric Boundary Layer*. Cambridge University Press (cit. on pp. 21, 31).
- Grossman, D. (2015). *As Himalayan Glaciers Melt, Two Towns Face the Fallout*. https://e360.yale.edu/features/as_himalay (cit. on p. 55).
- Holmgren, William F., Clifford W. Hansen, and Mark A. Mikofski (2018). “Pvlib Python: A Python Package for Modeling Solar Energy Systems”. In: *Journal of Open Source Software* 3.29, p. 884 (cit. on p. 137).
- Hori, Masahiro, Teruo Aoki, Tomonori Tanikawa, et al. (Feb. 2006). “In-Situ Measured Spectral Directional Emissivity of Snow and Ice in the 8–14 Mm Atmospheric Window”. In: *Remote Sensing of Environment* 100.4, pp. 486–502 (cit. on p. 28).
- Huang, Jianhua (June 2018). “A Simple Accurate Formula for Calculating Saturation Vapor Pressure of Water and Ice”. In: *AMETSOC* 57 (cit. on p. 21).
- Immerzeel, W. W., A. F. Lutz, M. Andrade, et al. (Jan. 2020). “Importance and Vulnerability of the World’s Water Towers”. In: *Nature* 577.7790, pp. 364–369 (cit. on p. 1).
- Ineichen, Pierre (Aug. 2008). “A Broadband Simplified Version of the Solis Clear Sky Model”. In: *Solar Energy* 82.8, pp. 758–762 (cit. on p. 137).
- IPCC (2019). “Chapter 2: High Mountain Areas — Special Report on the Ocean and Cryosphere in a Changing Climate”. In: *IPCC Special Report on the Ocean and Cryosphere in a Changing Climate* (cit. on p. 1).
- Kaser, Georg, Martin Großhauser, and Ben Marzeion (Nov. 2010). “Contribution Potential of Glaciers to Water Availability in Different Climate Regimes”. In: *Proceedings of the National Academy of Sciences* 107.47, pp. 20223–20227 (cit. on p. 60).
- Khan, Klaudia (2020). *A Marriage of Glaciers - Przekrój Magazine*. <https://przekroj.pl/en/science/a-marriage-of-glaciers-klaudia-khan-2> (cit. on p. 8).
- Kreutzmann, Hermann (Aug. 2011). “Scarcity within Opulence: Water Management in the Karakoram Mountains Revisited”. In: *Journal of Mountain Science* 8.4, pp. 525–534 (cit. on pp. 2, 37).
- Küng, O., C. Strecha, A. Beyeler, et al. (2011). “THE ACCURACY OF AUTOMATIC PHOTGRAMMETRIC TECHNIQUES ON ULTRA-LIGHT UAV IMAGERY”. In: *The International Archives of the Photogrammetry, Remote Sensing and Spatial Information Sciences* XXXVIII-1/C22, pp. 125–130 (cit. on p. 131).

- Labbal, V. (2000). "Traditional Oases of Ladakh: A Case Study of Equity in Water Management." In: *Sharing water: irrigation and water management in the Hindukush - Karakoram - Himalaya*, pp. 163–183 (cit. on pp. 2, 37).
- Lowe, David G. (2004). "Distinctive Image Features from Scale-Invariant Keypoints". In: *International Journal of Computer Vision* 60.2, pp. 91–110 (cit. on p. 131).
- Maria Gruber (2022). "Ice Stupas Ladakh, India (Unpublished)". Bachelor Thesis. University of Fribourg (cit. on pp. 50–52, 125).
- Messerli, Bruno, Daniel Vivioli, and Rolf Weingartner (Nov. 2004). "Mountains of the World: Vulnerable Water Towers for the 21st Century". In: *AMBIO: A Journal of the Human Environment* 33.sp13, pp. 29–34 (cit. on p. 60).
- Meteoblue (Feb. 2021). *Climate Guttannen*. <https://www.meteoblue.com/en/weather/historyclimate/climatemode> (cit. on p. 13).
- Mölg, Nico and Tobias Bolch (2017). "Structure-from-Motion Using Historical Aerial Images to Analyse Changes in Glacier Surface Elevation". In: *Remote Sensing* 9.10 (cit. on p. 131).
- Mölg, T. and D. R. Hardy (2004). "Ablation and Associated Energy Balance of a Horizontal Glacier Surface on Kilimanjaro". In: *J. Geophys. Res.-Atmos.* 109, pp. 1–13 (cit. on p. 28).
- Motschmann, Alina, Christian Huggel, Randy Muñoz, and Angela Thür (Sept. 2020). "Towards Integrated Assessments of Water Risks in Deglaciating Mountain Areas: Water Scarcity and GLOF Risk in the Peruvian Andes". In: *Geoenvironmental Disasters* 7.1, p. 26 (cit. on p. 58).
- Motschmann, Alina, Claudia Teutsch, Christian Huggel, et al. (June 2022). "Current and Future Water Balance for Coupled Human-Natural Systems – Insights from a Glaciated Catchment in Peru". In: *Journal of Hydrology: Regional Studies* 41, p. 101063 (cit. on p. 58).
- Mukhopadhyay, Biswajit and Asif Khan (Aug. 2015). "A Reevaluation of the Snowmelt and Glacial Melt in River Flows within Upper Indus Basin and Its Significance in a Changing Climate". In: *Journal of Hydrology* 527, pp. 119–132 (cit. on p. 1).
- Norphel, Chewang (2009). "Artificial Glacier: A High Altitude Cold Desert Water Conservation Technique". In: Energy and Climate Change in cold regions of Asia: Proceedings of the Seminar, Ladakh, India, pp. 62–64 (cit. on p. 37).
- Norphel, Chewang and Padma Tashi (2015). "Snow Water Harvesting in the Cold Desert in Ladakh: An Introduction to Artificial Glacier". In: *Mountain Hazards and Disaster Risk Reduction*. Ed. by Hari Krishna Nibanupudi and Rajib Shaw. Disaster Risk Reduction. Tokyo: Springer Japan, pp. 199–210 (cit. on pp. 1, 2, 11, 38, 40, 56).
- Nüsser, M., Juliane Dame, Benjamin Kraus, Ravi Baghel, and Susanne Schmidt (2019). "Socio-Hydrology of Artificial Glaciers in Ladakh, India: Assessing Adaptive Strategies in a Changing Cryosphere". In: *Regional Environmental Change* (cit. on pp. 1, 3, 11, 37–41, 56, 59, 124).

- Nüsser, Marcus and Ravi Baghel (2016). "Local Knowledge and Global Concerns: Artificial Glaciers as a Focus of Environmental Knowledge and Development Interventions". In: *Ethnic and Cultural Dimensions of Knowledge*. Ed. by Peter Meusburger, Tim Freytag, and Laura Suarsana. Knowledge and Space. Cham: Springer International Publishing, pp. 191–209 (cit. on pp. 1–3).
- Nüsser, Marcus, Susanne Schmidt, and Juliane Dame (2012). "Irrigation and Development in the Upper Indus Basin: Characteristics and Recent Changes of a Socio-hydrological System in Central Ladakh, India". In: *Mountain Research and Development* 32.1, pp. 51–61 (cit. on pp. 2, 13, 37).
- Oerlemans, J., S. Balasubramanian, C. Clavuot, and F. Keller (2021). "Brief Communication: Growth and Decay of an Ice Stupa in Alpine Conditions – a Simple Model Driven by Energy-Flux Observations over a Glacier Surface". In: *The Cryosphere* 15.6, pp. 3007–3012 (cit. on pp. 21, 138).
- Oerlemans, J. and W. H. Knap (1998). "A 1 Year Record of Global Radiation and Albedo in the Ablation Zone of Morteratschgletscher, Switzerland". In: *Journal of Glaciology* 44.147, pp. 231–238 (cit. on pp. 19, 28).
- Palmer, Lisa (Feb. 2022). "Storing Frozen Water to Adapt to Climate Change". In: *Nature Climate Change* 12.2, pp. 115–117 (cit. on pp. 2, 41).
- Pix4D SA (2020). *Pix4Dmapper 4.1 User Manual* (cit. on p. 131).
- Rabatel, A., B. Francou, A. Soruco, et al. (Jan. 2013). "Current State of Glaciers in the Tropical Andes: A Multi-Century Perspective on Glacier Evolution and Climate Change". In: *The Cryosphere* 7.1, pp. 81–102 (cit. on p. 60).
- Reuters (Oct. 2021). "Conservationists in Chile Aim to Freeze Water in Man-Made Glaciers". In: *Reuters* (cit. on pp. 2, 41).
- Sauter, Tobias, Anselm Arndt, and Christoph Schneider (Nov. 2020). "COSIPY v1.3 – an Open-Source Coupled Snowpack and Ice Surface Energy and Mass Balance Model". In: *Geoscientific Model Development* 13.11, pp. 5645–5662 (cit. on p. 33).
- Schmidt, L. S., G. Aðalgeirsdóttir, S. Guðmundsson, et al. (2017). "The Importance of Accurate Glacier Albedo for Estimates of Surface Mass Balance on Vatnajökull: Evaluating the Surface Energy Budget in a Regional Climate Model with Automatic Weather Station Observations". In: *The Cryosphere* 11.4, pp. 1665–1684 (cit. on p. 28).
- Shabina Faraz (June 2020). *The Glacier 'Marriages' in Pakistan's High Himalayas* (cit. on p. 8).
- ShiChang, Gao TanGuang, Zhang GuoShuai Zhou ShiQiao, and Kang (July 2010). "Response of Zhadang Glacier Runoff in Nam Co Basin, Tibet, to Changes in Air Temperature and Precipitation Form". In: *Chinese Science Bulletin* 55.20, pp. 2103–2110 (cit. on p. 28).
- Simant Verma (2018). *Ice Stupa Meltwater Measurements (Unpublished)* (cit. on p. 42).

- Soheb, Mohd, Alagappan Ramanathan, Anshuman Bhardwaj, and Lydia Sam (Mar. 2022). “Spatiotemporal Quantification of Key Environmental Changes in Stok and Kang Yatze Regions of Ladakh Himalaya, India”. In: *Geocarto International* 0.0, pp. 1–25 (cit. on p. 58).
- Steiner, Jakob F., Francesca Pellicciotti, Pascal Buri, et al. (2015). “Modelling Ice-Cliff Backwasting on a Debris-Covered Glacier in the Nepalese Himalaya”. In: *Journal of Glaciology* 61.229, pp. 889–907 (cit. on p. 28).
- Tennøe, Simen, Geir Halnes, and Gáute T. Einevoll (2018). “Uncertainpy: A Python Toolbox for Uncertainty Quantification and Sensitivity Analysis in Computational Neuroscience”. In: *Frontiers in Neuroinformatics* 12, p. 49 (cit. on p. 133).
- Turner, Darren, Arko Lucieer, and Christopher Watson (2012). “An Automated Technique for Generating Georectified Mosaics from Ultra-High Resolution Unmanned Aerial Vehicle (UAV) Imagery, Based on Structure from Motion (SfM) Point Clouds”. In: *Remote Sensing* 4.5, pp. 1392–1410 (cit. on p. 131).
- Tveiten, Ingvar (2007). “Glacier Growing - A Local Response to Water Scarcity in Baltistan and Gilgit, Pakistan”. PhD thesis (cit. on pp. 1, 9, 55).
- Vince, Gaia (Oct. 2009). “Glacier Man”. In: *Science* 326.5953, pp. 659–661 (cit. on pp. 1, 38).
- Wangchuk, S. (2014). “Ice Stupa Artificial Glaciers of Ladakh”. In: (cit. on p. 41).
- Wangchuk, Sonam (Dec. 2020). *Ice Stupa Competition*. <https://tribal.nic.in/IceStupa.aspx> (cit. on pp. 2, 41).
- Woolf, Harold M. (1968). *On the Computation of Solar Elevation Angles and the Determination of Sunrise and Sunset Times*. National Aeronautics and Space Administration (cit. on p. 19).
- Xiu, Dongbin and Jan S. Hesthaven (2005). “High-Order Collocation Methods for Differential Equations with Random Inputs”. In: *SIAM Journal on Scientific Computing* 27.3, pp. 1118–1139 (cit. on p. 135).
- Zolles, T., F. Maussion, S. P. Galos, W. Gurgiser, and L. Nicholson (2019). “Robust Uncertainty Assessment of the Spatio-Temporal Transferability of Glacier Mass and Energy Balance Models”. In: *The Cryosphere* 13.2, pp. 469–489 (cit. on p. 28).

References

- Aggarwal, Anubha, Holger Frey, Graham McDowell, et al. (Sept. 2021). “Adaptation to Climate Change Induced Water Stress in Major Glaciated Mountain Regions”. In: *Climate and Development* 0.0, pp. 1–13 (cit. on pp. 2, 41).
- Arndt, Anselm, Dieter Scherer, and Christoph Schneider (Apr. 2021). “Atmosphere Driven Mass-Balance Sensitivity of Halji Glacier, Himalayas”. In: *Atmosphere* 12.4, p. 426 (cit. on p. 36).

- Awaz Production (Mar. 2022). *Ice Stupa | Artificial Glacier Grafting in Skardu* (cit. on p. 2).
- Bagla, Pallava (Oct. 1998). "Artificial Glaciers to Help Farmers". In: *Science* 282.5389, pp. 619–619 (cit. on pp. 2, 56).
- BBC News (Feb. 2020). *Bright Artificial Glacier in Naryn - BBC Kyrgyz*. <https://www.youtube.com/watch?v=TpeSQf75bFc> (cit. on pp. 2, 41).
- Benn, Douglas I and Evans, David JA (2014). *Glaciers and Glaciation*. Routledge (cit. on p. 4).
- Bonales, L. J., A. C. Rodriguez, and P. D. Sanz (2017). "Thermal Conductivity of Ice Prepared under Different Conditions". In: *International Journal of Food Properties* 20.sup1, pp. 610–619 (cit. on p. 28).
- Brock, Ben W., Ian C. Willis, and Martin J. Sharp (2006). "Measurement and Parameterization of Aerodynamic Roughness Length Variations at Haut Glacier d'Arolla, Switzerland". In: *Journal of Glaciology* 52.177, pp. 281–297 (cit. on p. 28).
- Brutsaert, W. (1982). *Evaporation into the Atmosphere. Theory, History and Application*. Kluwer Academic Publishers (cit. on p. 20).
- (1975). "On a Derivable Formula for Long-Wave Radiation from Clear Skies". In: *Water Resources Research* 11.1-4, pp. 742–744 (cit. on p. 20).
- Buytaert, Wouter, Simon Moulds, Luis Acosta, et al. (Nov. 2017). "Glacial Melt Content of Water Use in the Tropical Andes". In: *Environmental Research Letters* 12.11, p. 114014 (cit. on p. 60).
- Chevuturi, A., A. P. Dimri, and R. J. Thayyen (Jan. 2018). "Climate Change over Leh (Ladakh), India". In: *Theoretical and Applied Climatology* 131.1, pp. 531–545 (cit. on p. 1).
- Clouse, Carey, Naomi Anderson, and Taylor Shippling (2017). "Ladakh's Artificial Glaciers: Climate-Adaptive Design for Water Scarcity". In: *Climate and Development* 9.5, pp. 428–438 (cit. on pp. 1, 3).
- Cogley, J. G., A. A. Arendt, A. Bauder, et al. (2010). "Glossary of Glacier Mass Balance and Related Terms". In: (cit. on p. 4).
- Cuffey, Kurt M. and W. S. B. Paterson (2010). *The Physics Of Glaciers*. Elsevier (cit. on pp. 17, 28).
- Farhan, Suhaib Bin, Yinsheng Zhang, Yingzhao Ma, Yanhong Guo, and Ning Ma (June 2015). "Hydrological Regimes under the Conjunction of Westerly and Monsoon Climates: A Case Investigation in the Astore Basin, Northwestern Himalaya". In: *Climate Dynamics* 44.11, pp. 3015–3032 (cit. on p. 1).
- Furukawa, Yasutaka and Jean Ponce (2010). "Accurate, Dense, and Robust Multiview Stereopsis". In: *IEEE Transactions on Pattern Analysis and Machine Intelligence* 32.8, pp. 1362–1376 (cit. on p. 131).
- Garratt, J. R. (1992). *The Atmospheric Boundary Layer*. Cambridge University Press (cit. on pp. 21, 31).

- Grossman, D. (2015). *As Himalayan Glaciers Melt, Two Towns Face the Fallout*. https://e360.yale.edu/features/as_himalayan_glaciers_melt_two_towns_face_the_fallout (cit. on p. 55).
- Holmgren, William F., Clifford W. Hansen, and Mark A. Mikofski (2018). “Pvlib Python: A Python Package for Modeling Solar Energy Systems”. In: *Journal of Open Source Software* 3.29, p. 884 (cit. on p. 137).
- Hori, Masahiro, Teruo Aoki, Tomonori Tanikawa, et al. (Feb. 2006). “In-Situ Measured Spectral Directional Emissivity of Snow and Ice in the 8–14 Mm Atmospheric Window”. In: *Remote Sensing of Environment* 100.4, pp. 486–502 (cit. on p. 28).
- Huang, Jianhua (June 2018). “A Simple Accurate Formula for Calculating Saturation Vapor Pressure of Water and Ice”. In: *AMETSO* 57 (cit. on p. 21).
- Immerzeel, W. W., A. F. Lutz, M. Andrade, et al. (Jan. 2020). “Importance and Vulnerability of the World’s Water Towers”. In: *Nature* 577.7790, pp. 364–369 (cit. on p. 1).
- Ineichen, Pierre (Aug. 2008). “A Broadband Simplified Version of the Solis Clear Sky Model”. In: *Solar Energy* 82.8, pp. 758–762 (cit. on p. 137).
- IPCC (2019). “Chapter 2: High Mountain Areas — Special Report on the Ocean and Cryosphere in a Changing Climate”. In: *IPCC Special Report on the Ocean and Cryosphere in a Changing Climate* (cit. on p. 1).
- Kaser, Georg, Martin Großhauser, and Ben Marzeion (Nov. 2010). “Contribution Potential of Glaciers to Water Availability in Different Climate Regimes”. In: *Proceedings of the National Academy of Sciences* 107.47, pp. 20223–20227 (cit. on p. 60).
- Khan, Klaudia (2020). *A Marriage of Glaciers - Przekrój Magazine*. <https://przekroj.pl/en/science/a-marriage-of-glaciers-klaudia-khan-2> (cit. on p. 8).
- Kreutzmann, Hermann (Aug. 2011). “Scarcity within Opulence: Water Management in the Karakoram Mountains Revisited”. In: *Journal of Mountain Science* 8.4, pp. 525–534 (cit. on pp. 2, 37).
- Küng, O., C. Strecha, A. Beyeler, et al. (2011). “THE ACCURACY OF AUTOMATIC PHOTGRAMMETRIC TECHNIQUES ON ULTRA-LIGHT UAV IMAGERY”. In: *The International Archives of the Photogrammetry, Remote Sensing and Spatial Information Sciences* XXXVIII-1/C22, pp. 125–130 (cit. on p. 131).
- Labbal, V. (2000). “Traditional Oases of Ladakh: A Case Study of Equity in Water Management.” In: *Sharing water: irrigation and water management in the Hindu Kush - Karakoram - Himalaya*, pp. 163–183 (cit. on pp. 2, 37).
- Lowe, David G. (2004). “Distinctive Image Features from Scale-Invariant Keypoints”. In: *International Journal of Computer Vision* 60.2, pp. 91–110 (cit. on p. 131).
- Maria Gruber (2022). “Ice Stupas Ladakh, India (Unpublished)”. Bachelor Thesis. University of Fribourg (cit. on pp. 50–52, 125).
- Messerli, Bruno, Daniel Vivioli, and Rolf Weingartner (Nov. 2004). “Mountains of the World: Vulnerable Water Towers for the 21st Century”. In: *AMBIO: A Journal of the Human Environment* 33.sp13, pp. 29–34 (cit. on p. 60).

- Meteoblue (Feb. 2021). *Climate Guttannen*. <https://www.meteoblue.com/en/weather/historyclimate/climatemodelled/> (cit. on p. 13).
- Mölg, Nico and Tobias Bolch (2017). "Structure-from-Motion Using Historical Aerial Images to Analyse Changes in Glacier Surface Elevation". In: *Remote Sensing* 9.10 (cit. on p. 131).
- Mölg, T. and D. R. Hardy (2004). "Ablation and Associated Energy Balance of a Horizontal Glacier Surface on Kilimanjaro". In: *J. Geophys. Res.-Atmos.* 109, pp. 1–13 (cit. on p. 28).
- Motschmann, Alina, Christian Huggel, Randy Muñoz, and Angela Thür (Sept. 2020). "Towards Integrated Assessments of Water Risks in Deglaciating Mountain Areas: Water Scarcity and GLOF Risk in the Peruvian Andes". In: *Geoenvironmental Disasters* 7.1, p. 26 (cit. on p. 58).
- Motschmann, Alina, Claudia Teutsch, Christian Huggel, et al. (June 2022). "Current and Future Water Balance for Coupled Human-Natural Systems – Insights from a Glaciated Catchment in Peru". In: *Journal of Hydrology: Regional Studies* 41, p. 101063 (cit. on p. 58).
- Mukhopadhyay, Biswajit and Asif Khan (Aug. 2015). "A Reevaluation of the Snowmelt and Glacial Melt in River Flows within Upper Indus Basin and Its Significance in a Changing Climate". In: *Journal of Hydrology* 527, pp. 119–132 (cit. on p. 1).
- Norphel, Chewang (2009). "Artificial Glacier: A High Altitude Cold Desert Water Conservation Technique". In: Energy and Climate Change in cold regions of Asia: Proceedings of the Seminar, Ladakh, India, pp. 62–64 (cit. on p. 37).
- Norphel, Chewang and Padma Tashi (2015). "Snow Water Harvesting in the Cold Desert in Ladakh: An Introduction to Artificial Glacier". In: *Mountain Hazards and Disaster Risk Reduction*. Ed. by Hari Krishna Nibanupudi and Rajib Shaw. Disaster Risk Reduction. Tokyo: Springer Japan, pp. 199–210 (cit. on pp. 1, 2, 11, 38, 40, 56).
- Nüsser, M., Juliane Dame, Benjamin Kraus, Ravi Baghel, and Susanne Schmidt (2019). "Socio-Hydrology of Artificial Glaciers in Ladakh, India: Assessing Adaptive Strategies in a Changing Cryosphere". In: *Regional Environmental Change* (cit. on pp. 1, 3, 11, 37–41, 56, 59, 124).
- Nüsser, Marcus and Ravi Baghel (2016). "Local Knowledge and Global Concerns: Artificial Glaciers as a Focus of Environmental Knowledge and Development Interventions". In: *Ethnic and Cultural Dimensions of Knowledge*. Ed. by Peter Meusburger, Tim Freytag, and Laura Suarsana. Knowledge and Space. Cham: Springer International Publishing, pp. 191–209 (cit. on pp. 1–3).
- Nüsser, Marcus, Susanne Schmidt, and Juliane Dame (2012). "Irrigation and Development in the Upper Indus Basin: Characteristics and Recent Changes of a Socio-hydrological System in Central Ladakh, India". In: *Mountain Research and Development* 32.1, pp. 51–61 (cit. on pp. 2, 13, 37).
- Oerlemans, J., S. Balasubramanian, C. Clavuot, and F. Keller (2021). "Brief Communication: Growth and Decay of an Ice Stupa in Alpine Conditions – a Simple Model Driven by Energy-Flux Observations over a Glacier Surface". In: *The Cryosphere* 15.6, pp. 3007–3012 (cit. on pp. 21, 138).

- Oerlemans, J. and W. H. Knap (1998). "A 1 Year Record of Global Radiation and Albedo in the Ablation Zone of Morteratschgletscher, Switzerland". In: *Journal of Glaciology* 44.147, pp. 231–238 (cit. on pp. 19, 28).
- Palmer, Lisa (Feb. 2022). "Storing Frozen Water to Adapt to Climate Change". In: *Nature Climate Change* 12.2, pp. 115–117 (cit. on pp. 2, 41).
- Pix4D SA (2020). *Pix4Dmapper 4.1 User Manual* (cit. on p. 131).
- Rabatel, A., B. Francou, A. Soruco, et al. (Jan. 2013). "Current State of Glaciers in the Tropical Andes: A Multi-Century Perspective on Glacier Evolution and Climate Change". In: *The Cryosphere* 7.1, pp. 81–102 (cit. on p. 60).
- Reuters (Oct. 2021). "Conservationists in Chile Aim to Freeze Water in Man-Made Glaciers". In: *Reuters* (cit. on pp. 2, 41).
- Sauter, Tobias, Anselm Arndt, and Christoph Schneider (Nov. 2020). "COSIPY v1.3 – an Open-Source Coupled Snowpack and Ice Surface Energy and Mass Balance Model". In: *Geoscientific Model Development* 13.11, pp. 5645–5662 (cit. on p. 33).
- Schmidt, L. S., G. Æðalgeirs ðóttir, S. Guðmundsson, et al. (2017). "The Importance of Accurate Glacier Albedo for Estimates of Surface Mass Balance on Vatnajökull: Evaluating the Surface Energy Budget in a Regional Climate Model with Automatic Weather Station Observations". In: *The Cryosphere* 11.4, pp. 1665–1684 (cit. on p. 28).
- Shabina Faraz (June 2020). *The Glacier 'Marriages' in Pakistan's High Himalayas* (cit. on p. 8).
- ShiChang, Gao TanGuang, Zhang GuoShuai Zhou ShiQiao, and Kang (July 2010). "Response of Zhadang Glacier Runoff in Nam Co Basin, Tibet, to Changes in Air Temperature and Precipitation Form". In: *Chinese Science Bulletin* 55.20, pp. 2103–2110 (cit. on p. 28).
- Simant Verma (2018). *Ice Stupa Meltwater Measurements (Unpublished)* (cit. on p. 42).
- Soheb, Mohd, Alagappan Ramanathan, Anshuman Bhardwaj, and Lydia Sam (Mar. 2022). "Spatiotemporal Quantification of Key Environmental Changes in Stok and Kang Yatze Regions of Ladakh Himalaya, India". In: *Geocarto International* 0.0, pp. 1–25 (cit. on p. 58).
- Steiner, Jakob F., Francesca Pellicciotti, Pascal Buri, et al. (2015). "Modelling Ice-Cliff Backwasting on a Debris-Covered Glacier in the Nepalese Himalaya". In: *Journal of Glaciology* 61.229, pp. 889–907 (cit. on p. 28).
- Tennøe, Simen, Geir Halnes, and Gaute T. Einevoll (2018). "Uncertainpy: A Python Toolbox for Uncertainty Quantification and Sensitivity Analysis in Computational Neuroscience". In: *Frontiers in Neuroinformatics* 12, p. 49 (cit. on p. 133).
- Turner, Darren, Arko Lucieer, and Christopher Watson (2012). "An Automated Technique for Generating Georectified Mosaics from Ultra-High Resolution Unmanned Aerial Vehicle (UAV) Imagery, Based on Structure from Motion (SfM) Point Clouds". In: *Remote Sensing* 4.5, pp. 1392–1410 (cit. on p. 131).
- Tveiten, Ingvar (2007). "Glacier Growing - A Local Response to Water Scarcity in Baltistan and Gilgit, Pakistan". PhD thesis (cit. on pp. 1, 9, 55).

- Vince, Gaia (Oct. 2009). “Glacier Man”. In: *Science* 326.5953, pp. 659–661 (cit. on pp. 1, 38).
- Wangchuk, S. (2014). “Ice Stupa Artificial Glaciers of Ladakh”. In: (cit. on p. 41).
- Wangchuk, Sonam (Dec. 2020). *Ice Stupa Competition*. <https://tribal.nic.in/IceStupa.aspx> (cit. on pp. 2, 41).
- Woolf, Harold M. (1968). *On the Computation of Solar Elevation Angles and the Determination of Sunrise and Sunset Times*. National Aeronautics and Space Administration (cit. on p. 19).
- Xiu, Dongbin and Jan S. Hesthaven (2005). “High-Order Collocation Methods for Differential Equations with Random Inputs”. In: *SIAM Journal on Scientific Computing* 27.3, pp. 1118–1139 (cit. on p. 135).
- Zolles, T., F. Maussion, S. P. Galos, W. Gurgiser, and L. Nicholson (2019). “Robust Uncertainty Assessment of the Spatio-Temporal Transferability of Glacier Mass and Energy Balance Models”. In: *The Cryosphere* 13.2, pp. 469–489 (cit. on p. 28).

List of Figures

1.1	Seasonal variation in the availability of irrigation water. The graph highlights the crucial role of AIRs in bridging the gap in water availability. Adapted from Marcus Nüsser and Baghel, 2016	2
1.2	(a) Schematic overview of the position of artificial ice reservoirs. These constructions are located at altitudes between the glaciers and the irrigation networks in the cultivated areas. (b) Ice terraces at 3900 m, located above the village of Nang, Ladakh. The cascade is composed of a series of loose masonry walls ranging in height from 2 to 3 m, which help freeze water for storage. (c) Ice stupas at 3600 m, located above the village of Phyang, Ladakh. They are made using fountain systems. Adapted from Marcus Nüsser and Baghel, 2016	3
3.1	The Swiss and Indian AIRs were 5 m and 13 m tall on January 9 and March 3, 2021 respectively. Picture credits: Daniel Bürki (left) and Thinles Norboo (right)	12
3.2	Spray radius of the CH20 AIR	14
3.3	Model schematic showing the workflow used in the model at every time step.	16
3.4	Shape variables of the AIR. r_{cone} is the radius, h_{cone} is the height, j_{cone} is the thickness change and s_{cone} is the slope of the ice cone. r_F is the spray radius of the fountain.	18
3.5	(a) Total-order sensitivities of all the uncertain parameters of the model with net water loss as the objective. (b) The calibration of the sensitive parameter, Δx with the RMSE between the drone and model estimates of the ice volume. The dots denote the optimum values. The estimates from the Swiss and Indian AIRs are denoted with blue and red colors respectively.	29

3.6	Simulated ice volume during the lifetime of the AIRs (blue curve). The shaded regions (light blue and orange) represent the 90% prediction interval of the AIR ice volume caused by the variations in weather and fountain forcing parameters, respectively. Violet points indicate the drone ice volume observations. The grey dashed line represents the observed expiry date for each AIR.	30
3.7	Comparison of volume estimates generated from the AIR and COSISTUPA models.	35
4.1	Different types of ice reservoirs. Adapted from M. Nüsser et al., 2019	38
4.2	Ice terrace of Phuktse, viewpoint 4430 m. (a) February 2014 (b) October 2014 Adapted from: M. Nüsser et al., 2019	39
4.3	The process of ice accumulation for ice terraces. Adapted from M. Nüsser et al. (2019)	40
4.4	Ice stupa of Phyang village on March 2015.	40
4.5	The construction process of ice stupas. Diagrams by: Francesco Muzzi	41
4.6	Irrigation channel of the ice stupa at Phyang village. (P.C. Lobzang Dadul)	42
4.7	Daily meltwater measurements for the IN17 and IN18 AIRs along with the corresponding model estimations for the IN21 AIR.	43
4.8	Unscheduled and scheduled fountains used for construction of traditional and automated AIRs at Guttannen. Picture credits: Daniel Bürki	44
4.9	Volume validation of the scheduled and unscheduled fountain construction strategies.	46
4.10	(a) Surface albedo and (b) fountain discharge heat flux showed significant variations between the two AIRS due to the differences in their discharge rates.	47
4.11	(a) The maximum volume and water-use efficiency estimated for AIRs constructed in different locations (represented by symbols) with different fountain scheduling strategies (represented by colours). Experimental values are highlighted in circles and simulated values are highlighted in squares. (b) Comparison of the unscheduled and scheduled fountain discharge rates at the IN21 location.	48
5.1	Regions where AIRs have been built.	50

5.2	Some villages of Ladakh where AIRs have been built. Adapted from Maria Gruber (2022)	51
5.3	Relationship of measured ice volume with altitude of AIRs built during winter of 2019-20 across different villages in Ladakh. Adapted from Maria Gruber (2022)	52
5.4	Icestupa at Shara, Ladakh, built by local farmers in the winter of 2019-20, survived a full summer melt season and released around 8 million litres of water.	53
5.5	The effect of a negative temperature perturbation. For $\Delta T = -3^{\circ}C$ the icestupa does not disappear anymore but is growing from year to year.	53
5.6	(a) Estimated volume change and temperature and (b) Observed spray radius and wind speed during January for AIRs built across three winters.	54
6.1	Compilation of AIRs built in different villages of Ladakh.	56
6.2	One of the deserted villages in Ladakh where AIR meltwater supported a harvest of 1300 kgs of potatoes in October 2021. (P.C. Icestupa Project)	57
A.1	Digital elevation map of Indian AIR constructed from the drone survey on March 3, 2021. The green area represents the area bounded by the marked perimeter and the red area represents gaps in the point cloud that were filled to compute the associated volume.	132

List of Tables

3.1	Summary of the weather observations for AIRs built during the respective study period. The weather measurements are shown using their mean (μ) and standard deviation (σ) during the study period as $\mu \pm \sigma$	14
3.2	List of all the studied AIRs. The study period starts when the fountain was first switched on (denoted as Start Date) and ends when the respective AIR either melted or broke into several ice blocks (denoted as Expiry Date).	15
3.3	Free parameters in the model categorised as constant, derived, model hyperparameters, weather and fountain forcing parameters with their respective values/ranges.	28
4.1	Assumptions for the parametrisation introduced to simplify the ice volume optimised model (IVOM) and water-use efficiency optimised model (WEOM). $\alpha_{snow/ice}$ represents albedo of snow or ice respectively.	45
A.1	List of all the studied AIRs in Ladakh.	133

List of abbreviations

AIRs Artificial Ice Reservoirs

AWS Automatic Weather Station

DEMs Digital Elevation Maps

RMSE Root Mean Squared Error

IVOM Ice Volume Optimised Model

WEOM Water-use Efficiency Optimised Model

Appendix

A.1 Drone surveys processing methodology

The drone flew along a predefined flight course and took photographs at a set time interval. The position and altitude of the drone at the exposure stations, which were obtained by the built-in integrated Position and Orientation System (POS, composed of a global positioning system and inertial measurement units), were recorded in JPEG pictures. In this study, we adopted a three-step workflow as implemented in the commercial software package Pix4Dmapper version 4.6.4 (Pix4D SA, 2020). A short summary of this workflow is described below:

- (1) Initial processing: This process generates a sparse point cloud with the structure-from motion algorithm (Turner et al., 2012). First, it searches for and matches key points in the photos that have certain overlapping areas using a feature matching algorithm (e.g., the scale-invariant feature transform (SIFT) algorithm, which can detect key points in photos with different views and illumination conditions; Lowe, 2004). Second, the approximate locations and orientations of the camera at each exposure station are reconstructed with the internal parameters (focal length, coordinates of the principal point of the photograph), and external parameters (i.e. POS data). A sparse point cloud is created.
- (2) Point cloud densification: In this step, the multi-view stereo technique is applied to achieve a higher point cloud density than in the previous step (Furukawa and Ponce, 2010; N. Mölg and Bolch, 2017). Thus, the spatial resolution of the products can be increased, and an irregular network for the next step can be created (Küng et al., 2011).
- (3) AIR delineation: Ice radius, area and volume are the three final products. Perimeter was manually marked on the point cloud by identifying the AIR boundary (see Fig. A.1). For the Indian location, we identified identical rock features near the ice boundary to mark as vertices of this perimeter. For

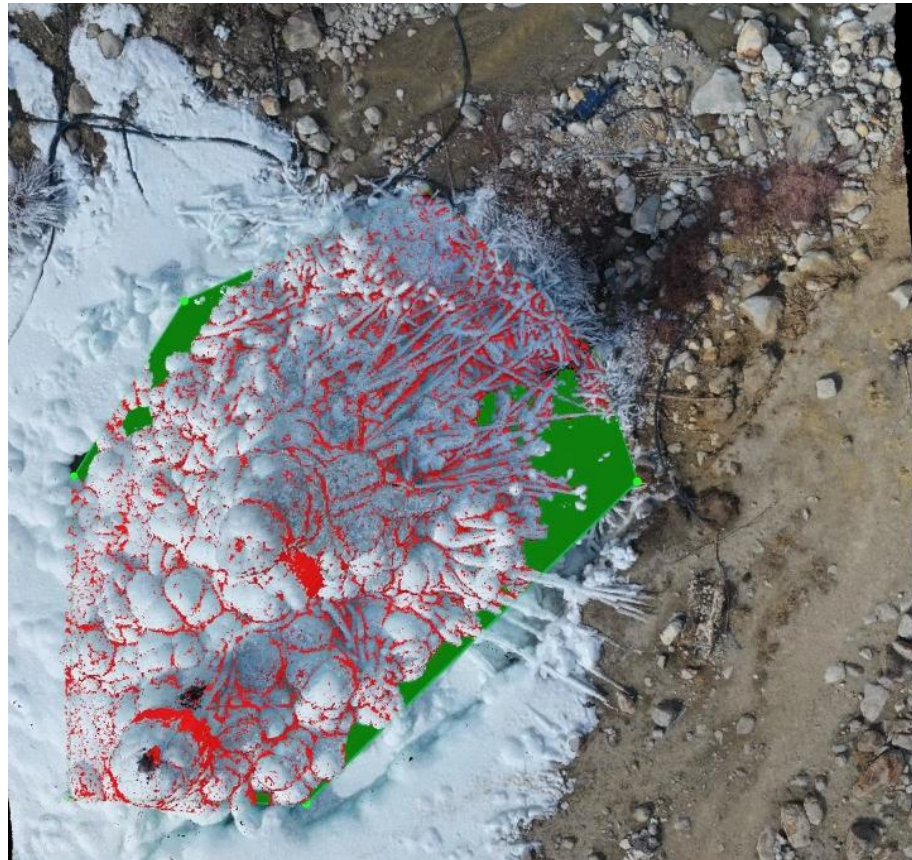


Fig. A.1.: Digital elevation map of Indian AIR constructed from the drone survey on March 3, 2021. The green area represents the area bounded by the marked perimeter and the red area represents gaps in the point cloud that were filled to compute the associated volume.

Tab. A.1.: List of all the studied AIRs in Ladakh.

Location	Winter season	Altitude [m a.s.l.]	Radius [m]	Volume [m^3]
Igoo	2019–20	4209	23	4918
Karith	2019–20	3710	12	1451
Karith 2	2020–21	3692	5	1133
Lamso	2019–20	3859	7	615
Lamso 2	2020–21	3863	6	420
Nang	2019–20	3897	13	1601
Phyang	2019–20	3916	19	5182
Sandoo	2019–20	3773	10	1483
Shara	2019–20	4288	18	7936
Gangles	2020–21	4072	9	602
Apati	2020–21	3840	6	351
Mulbeck	2019–20	3451	11	1887
Nang	2019–20	3897	13	1601
Skurbuchan	2019–20	3023	9	956
Takmachik	2019–20	3032	13	1265
Takmachik 2	2020–21	3052	10	1604
Tarchit	2020–21	3962	17	2363
Patherak	2020–21	3899	10	770
Kullum	2020–21	3907	7	328

the Swiss AIR, no such feature was available due to snowfall, so instead the perimeter was marked by identifying the ice and snow boundary.

There is temporal and spatial uncertainty associated with this process. Weather conditions influence the quality of each drone survey to various degrees. Moreover, since ice/snow surfaces do not have many identifiable features, few feature points can be detected and matched in the vicinity of the AIR. Thus, we attach a high uncertainty of $\pm 10\%$ for all the AIR observations to accommodate for this.

A.2 Sensitivity and uncertainty analysis

In this section, we summarise the theory behind the methods for uncertainty quantification and sensitivity analysis used. For a detailed explanation of this methodology, see Tennøe et al., 2018.

A.2.1 Problem definition

Consider our model U that depends on timestep i , has d uncertain parameters $Q = [Q_1, Q_2, \dots, Q_d]$, and gives output V_{ice} :

$$V_{ice} = U(i, Q) \quad (\text{A.1})$$

The output V_{ice} can have any value within the output space and has an unknown probability density function $\rho_{V_{ice}}$. The goal of our uncertainty quantification is to describe the unknown $\rho_{V_{ice}}$ through statistical metrics.

We assume that all these parameters are statistically independent from each other and have a uniform probability density function ρ_{Q_j} . The joint multivariate probability density function for the uncertain parameters is then:

$$\rho_Q = \prod_{j=1}^d \rho_{Q_j} \quad (\text{A.2})$$

As mentioned, the goal of an uncertainty quantification is to describe the unknown distribution of the model output through statistical metrics. A useful metric is the $(100 \cdot x)$ -th percentile P_x of V_{ice} , which defines a value below which $100 \cdot x$ percent of the model outputs are located. We can combine two percentiles to create a prediction interval, which is a range of values within which a $100 \cdot x$ percentage of the outputs V_{ice} occur. In our methodology, we use the 90 % prediction interval I^k , as the metric to compare the uncertainties of a given set of parameters Q^k . This is defined as:

$$I^k = [P_{(0.9/2)}, P_{(1-0.9/2)}] \quad (\text{A.3})$$

A.2.2 Sensitivity analysis

We use a variance-based sensitivity analysis and compute the commonly considered Sobol sensitivity indices (Sobol, 1990). The Sobol sensitivity indices quantify how much of the variance in the model output each uncertain parameter is responsible for. There are several types of Sobol indices. The first

order Sobol sensitivity index S_j measures the direct effect each parameter has on the variance of the model. Higher order Sobol indices give the sensitivity due to interactions between a parameter Q_j and various other parameters. The total Sobol sensitivity S_{Tj} includes the sensitivity of both first order effects, as well as the sensitivity due to interactions between a given parameter Q_j and all combinations of the other parameters. The sum of the total Sobol sensitivity indices is equal to or greater than one, and is only equal to one if there are no interactions between the parameters. Our goal is to use sensitivity analysis to fix parameters with high sensitivity, so the total-order Sobol indices are an appropriate metric.

A.2.3 Polynomial Chaos Expansions

A recent mathematical framework for efficient uncertainty quantification and sensitivity analysis is that of polynomial chaos expansions (Xiu and Hesthaven, 2005). This method calculates the same statistical metrics as the Monte Carlo method but typically much faster.

The general idea behind polynomial chaos expansions is to approximate the model U with a polynomial expansion \hat{U} :

$$U \approx \hat{U}(i, Q) = \sum_{n=0}^{N_p-1} c_n(i) \phi_n(Q) \quad (\text{A.4})$$

where ϕ_n are polynomials, and c_n are expansion coefficients. The number of expansion factors N_p is given by

$$N_p = \binom{d+p}{p} \quad (\text{A.5})$$

where p is the polynomial order.

The first and total-order indices can also be calculated directly from the polynomial chaos expansion. On the other hand, the 90 % prediction interval (I) must be estimated by using \hat{U} as a surrogate model.

A.3 Model forcing based on water-use efficiency and maximum ice volume objectives

The model complexity and data requirement (paper I) were reduced through assumptions that optimise for the ice volume or the water-use efficiency objectives. The corresponding model assumptions are called IVOM and WEOM respectively. We define the freezing rate and melting rate as the positive and negative mass change rate, respectively. Assumptions are chosen, based on whether they overestimate/underestimate the freezing rate. IVOM assumptions overestimates freezing rate whereas WEOM assumptions underestimates freezing rate. We describe these two kinds of assumptions applied on each of the energy balance components below:

A.3.1 Surface Area A_{cone} assumptions

The surface area during the accumulation period is determined by assuming a constant ice cone radius equal to the fountain spray radius. The surface area scales the freezing rate of the AIR. Hence, for the IVOM version, we assume the maximum possible slope of 1 for the ice cone or in other words $h_{cone} = r_F$. Therefore, area is estimated as:

$$A_{cone} = \sqrt{2} \cdot \pi \cdot r_F^2 \quad (\text{A.6})$$

Similarly, for the water-use efficiency objective, the area of the conical AIR is approximated to the area of its circular base. Therefore, area is estimated as:

$$A_{cone} = \pi \cdot r_F^2 \quad (\text{A.7})$$

A.3.2 Net shortwave radiation q_{SW} assumptions

The net shortwave radiation q_{SW} is computed as follows:

$$q_{SW} = (1 - \alpha) \cdot (SW_{direct} \cdot f_{cone} + SW_{diffuse}) \quad (\text{A.8})$$

where α is the albedo value ; SW_{direct} is the direct shortwave radiation; $SW_{diffuse}$ is the diffuse shortwave radiation and f_{cone} is the solar area fraction.

The data requirement was reduced by estimating the global shortwave radiation and pressure directly using the location's coordinates and altitude through the solar radiation model described in Holmgren et al. (2018). The algorithm used to estimate the clear-sky global radiation is described in Ineichen (2008).

The diffuse and direct shortwave radiation is determined using the estimated global solar radiation as follows:

$$\begin{aligned} SW_{diffuse} &= cld \cdot SW_{global} \\ SW_{direct} &= (1 - cld) \cdot SW_{global} \end{aligned} \quad (\text{A.9})$$

where cld is the cloudiness factor. cld is assumed to be 1 and 0 for the water-use efficiency and ice volume objective respectively.

We ignore the variations in the albedo and assume it to be equal to snow albedo and ice albedo for the ice volume and water-use efficiency objective, respectively.

The solar area fraction f_{cone} of the ice structure exposed to the direct shortwave radiation depends on the shape considered. It is computed as

$$f_{cone} = \frac{(0.5 \cdot r_{cone} \cdot h_{cone}) \cdot \cos\theta_{sun} + (\pi \cdot (r_{cone})^2 / 2) \cdot \sin\theta_{sun}}{\pi \cdot r_{cone} \cdot ((r_{cone})^2 + (h_{cone})^2)^{1/2}} \quad (\text{A.10})$$

For the ice volume objective, since we assume the slope of the cone to be 1, f_{cone} is determined as follows:

$$f_{cone} = \frac{\cos\theta_{sun} + \pi \cdot \sin\theta_{sun}}{2\sqrt{2} \cdot \pi} \quad (\text{A.11})$$

Similarly, for the water-use efficiency objective, since we assume the slope of the cone to be negligible, we get:

$$f_{cone} = \frac{\sin\theta_{sun}}{2} \quad (\text{A.12})$$

A.3.3 Net Longwave radiation q_{LW} assumptions

We assume $T_{ice} = 0^{\circ}\text{C}$ in order to determine outgoing longwave radiation. Since it is challenging to constrain the minimum ice temperature, we maintain this assumption for both our objectives. However, in order to estimate atmospheric emissivity, we again assume cld to be 1 and 0 for the water-use efficiency and ice volume objective respectively.

A.3.4 Turbulent fluxes assumptions

Turbulent fluxes estimation depend on the slope of the cone through the μ_{cone} parameter. As suggested by Oerlemans, Balasubramanian, et al. (2021), we estimated this parameter as follows:

$$\mu_{cone} = 1 + s_{cone}/2 \quad (\text{A.13})$$

Hence, the μ_{cone} parameter takes values of 1.5 and 1 for the ice volume and water-use efficiency objective respectively. Since turbulent fluxes impact both the freezing and the melting rates, this assumption may not favor the corresponding objectives for certain sites.

Acknowledgement

A PhD, in which you have to do a research project, is a daunting task. How could I possibly frame the questions that would lead to significant discoveries; design and interpret an experiment so that the conclusions were absolutely convincing; foresee difficulties and see ways around them, or, failing that, solve them when they occurred?

These were the reasons why I didn't even apply for PhD projects after my masters in Mathematics and rather decided to wander around the Himalayas. The seeds of this PhD were sown then, during my 3-year long immersion with the mountain communities of Ladakh. Living among mountains of sand, I recognised the futility of human life but was also alarmed by how small human-scale actions could transform these mountains beyond recognition. How is this even possible and what can be done about it? Looking back, those were the questions that pushed me to pursue this journey.

But why did I end up here in Switzerland, my first foreign country and how did I get an opportunity to pursue a PhD in the domain of glaciology, a subject which I had no knowledge about? Short answer: The trust and support of three people: Sonam Wangchuk, Felix Keller, and Martin Hoelzle. With Sonam, there were always great ideas around. All I had to do was pick my favourite and pursue it. It was together with him, I began to interrogate all things ice. With Felix, Switzerland became a country where my second home is. Without his support, I cannot imagine how I would have transitioned into the Swiss way of life. In Martin, I found a colleague twice my age whose engagement around scientific questions was unmatched. I owe a lot to each of them who mentored me around in Phyang, Samedan and Fribourg for the past seven years.

A PhD thesis does not write itself, nor does its author operate from a deserted island. As such, I would like to acknowledge the many individuals that contributed to the realization of this work in, what will most likely be, one of the most read sections of this thesis. This work would not have been possible without the support, collaboration and friendship of my family, friends and

colleagues. To that end, I attempted to thank all of them in the following paragraphs.

First and foremost, words cannot express my gratitude and appreciation for professor Martin Hoelzle, my mentor. You initiated and guided me through the wondrous world of science, at every step giving me that extra push to believe in myself. I am grateful for the entire journey; from writing proposals and manuscripts to suffering through the destructive feedbacks together, from discussing research problems to helping others write their bachelors and masters thesis around them, from designing experiments on the blackboard to establishing Swiss and Indian icestupa laboratories, from mere equations to real insights, to today, almost holding my PhD.

My Ph.D. project was somewhat interdisciplinary and, for a while, whenever I ran into a problem, I pestered a lot of people for help: from the university concierge Tony for his experience with pipelines to the faculty who were experts in the various disciplines that I needed. I remember the day when Johannes Oerlemans (who won the International Glaciological Society's Richardson medal two years later) told me he didn't know how to solve the problem I was having in his area. I was a first-year graduate student and I figured that Oerlemans knew much more than I did. If he didn't have the answer, nobody did.

That's when it hit me: nobody did. That's why it was a research problem. And being my research problem, it was up to me to solve. Once I faced that fact, the going got easy. The crucial lesson was that the scope of things I didn't know wasn't merely vast; it was, for all practical purposes, infinite. That realization, instead of being discouraging, was liberating. If our ignorance is infinite, the only possible course of action is to muddle through as best we can.

Dozens of people have contributed with days and days of work for collecting the associated datasets. My special thanks goes to the Himalayan Institute of Alternatives, Ladakh (HIAL) team who provided administrative and material support to conduct measurement campaigns in India. Norboo Thinles, Nishant Tiku, Sourabh Maheshwari and Dr. Tom Matthews were instrumental for making these campaigns a success. Without the unconditional support of Daniel Bürki from Guttannen Bewegt, the frequent drone flights and expensive installations during the past 3 winters would not have been possible. I would also like to thank Adolf Kaeser and Mr. Flavio Catillaz from Eispalast

Schwarzsee. Even though no datasets from this site appear in the thesis or our publications, the field experience we gained there was a necessary precondition for success in our future sites.

In hindsight, my PhD alone would not have done justice to reveal all the insights hidden in these datasets. Therefore, I am grateful that Michelle Stirnimann and Maria Gruber opted to explore these datasets in their masters and bachelors thesis work. Moreover, all the fieldwork remained lively thanks to their presence and enthusiasm over this work.

One of the main reasons I arrived (almost) everyday to work are the fabulous colleagues of the Cryosphere department, many of whom became good friends. My office mates over the years, Shafaq, Mario, Ottavia, Romain, Rebecca, and Esther made our room quite lively, which I missed a lot during periods of remote work. These colleagues coming from literally all parts of the world, gave me an incredible international experience. It was also a great experience to teach Bachelors courses with Horst and Eric. Luke deserves a special mention for the one with the most wisdom in the department. His timely recommendation to use the Schwarzsee Eispalast as my first experiment site kickstarted my PhD in earnest. I also like to thank the administrative staff for welcoming me into the department. David and Sylvie, apart from taking care of my logistic and financial hurdles, also nudged me in every encounter to become a better french speaker. Nicole, for taking that extra care towards sorting all my visa anxieties. Alex showed me how cool technicians can be with his stories and youthfulness. I feel very blessed to have spent time with all of you, ranging from many afterwork drinks, numerous coffee breaks, lunches, dinners, conferences, train rides, and treks. All of you contributed to the exceptional warm and cosy atmosphere at our department and I cherished every minute.

Without the generous support from the Swiss Government Excellence Scholarship (SGES) and the University of Fribourg (UniFR), this research would not have been possible. Beyond financial support, the SGES were also very accomodating for my field work requirements during a global pandemic and made exceptions for me that have never been made before. I am also grateful to have received grants from the Swiss Polar Institute and GlaciersAlive Association that enabled the extensive fieldwork over the past few winters.

Not everything is science! Eluckkiya made sure it was that way. Without her, I feel I would have languished much longer with the innumerable research questions emerging around this nascent topic.

Last but not the least, I would like to express the most sincere gratitude to my parents. Some of my hard life choices like volunteering in the mountains or shifting abroad were worth considering only because I always had their emotional and financial support to lean back on.

Colophon

This thesis was typeset with $\text{\LaTeX} 2_{\varepsilon}$. It uses the *Clean Thesis* style developed by Ricardo Langner.

Download the *Clean Thesis* style at <http://cleantheesis.der-ric.de/>.

Declaration

You can put your declaration here, to declare that you have completed your work solely and only with the help of the references you mentioned.

Fribourg, August 29, 2022

Suryanarayanan
Balasubramanian

